

Reactionless Motion Control of Free-Floating/Flying Space Manipulators and its Applications

Master Thesis Presented to
the Graduate School of Engineering,
Tokyo City University
in Partial Fulfillment of the Requirements
for the Degree of Master of Engineering Course

1481214 Hiroki Sone
Advisor: Prof. Dragomir N. Nenchev
Assoc. Prof. Daisuke Sato

January 29th, 2016

Contents

1	Introduction	11
1.1	Space robots	11
1.1.1	Control issues with FFSR	13
1.1.2	Reactionless motion control	14
1.1.3	Energy consumption	16
1.2	Motion/Force control	17
1.3	Aim of this study	19
1.4	Outline of this thesis	20
1.5	The roles of variable's index	21
2	Basic Notation	23
2.1	Modeling of free-floating base robots	23
2.1.1	Kinematics	24
2.1.2	Kinetic energy	25
2.1.3	Inertia submatrices	26
2.1.4	Equation of motion	27
2.2	Momentum conservation law	28
2.2.1	Linear momentum conservation law	28
2.2.2	Angular momentum conservation law	29
2.3	Reaction Null-Space	31
2.3.1	Momentum based derivation	32

2.3.2	Dynamics based derivation	32
2.4	Summary	33
I	Reactionless Motion Control	35
3	Review of Reactionless Motion and Analysis	37
3.1	Reactionless motion control	37
3.2	Qualitative study of reactionless motion	39
3.2.1	Vector field of reactionless motion	39
3.2.2	Fixed point and bifurcation	40
3.2.3	Rank deficiency of the coupling inertia matrix	42
3.3	Summary	43
4	Proposal of Reactionless Tasks	45
4.1	Manipulator model	45
4.1.1	Model description	45
4.1.2	Reactionless motion representation	46
4.2	Inspection task using a hand-held camera	49
4.2.1	Control command	50
4.2.2	Numerical simulation	51
4.3	Singularities within the inspection task	54
4.3.1	Problem statement	54
4.3.2	Singularity treatment with the Damped Least-Squares inverse	56
4.4	Point-to-point positioning task	60
4.4.1	The 3-Phase method	61
4.4.2	Verification via numerical simulations	62
4.5	Deployment task	65
4.5.1	Full reactionless task	66

<i>CONTENTS</i>	3
4.6 Summary	68
5 Energy Consumption Analysis	71
5.1 Kinetic energy	71
5.2 Motion equivalence	73
5.2.1 Comparative study for the inspection task	78
5.2.2 Simulation results	79
5.3 Summary	80
 II Motion/Force Control	 83
6 Formulation and Modeling	85
6.1 Formulations	85
6.1.1 OS formulation based control	85
6.1.2 Reaction Null-Space based control	89
6.2 Examples	92
6.2.1 Planar three-DoF manipulator	92
6.2.2 Seven DoF redundant manipulator	97
6.3 Summary	99
 7 Analysis of Joint Motion Behavior	 103
7.1 Influence of the inertia parameter	103
7.1.1 Analysis through simulation	104
7.1.2 Discussion	105
7.1.3 Verification via numerical simulations	107
7.2 Stabilization of joint motion	109
7.2.1 The velocity-level based acceleration solution	110
7.2.2 Verification via numerical simulations	111
7.3 Summary	112

8	Conclusions and Future Research Directions	113
8.1	Conclusions	113
8.2	Future tasks	115
	References	117
	Research Progresses	127

List of Figures

1.1	Space robotic systems: (a) Canadarm ©NASA, (b) Canadarm 2 ©NASA, (c) JEMRMS ©JAXA and (d) ETS-VII.	12
2.1	General model of free-floating base robot.	24
2.2	Relationship between a variation of translation and a rotational variation.	30
3.1	A planar two-DoF space manipulator model with $m_i = 100$ kg, $l_i = 1.0$ m ($i = 1, 2$); the base mass is $m_b = 1000$ kg. The vector field is obtain with $r = 0$ m.	39
3.2	The vector field and nullclines for each joint direction when r variates as: (a) $r = 0.5$ m, (b) $r = 0.945$ m and (c) $r = 1.5$ m.	41
3.3	This figure shows the determinant of $(\mathbf{M}_{\omega m} \tilde{\mathbf{M}}_{\omega m}^T)$ and the distance between the manipulator CoM and the base one as color map: (a) $\det(\tilde{\mathbf{M}}_{\omega m} \tilde{\mathbf{M}}_{\omega m}^T)$ and (b) the distance between the manipulator CoM and the base one.	42
4.1	Our manipulator model with seven-DoF mechanism at the initial configuration ($\theta_i = 0$ rad, $\forall \theta_i$).	46
4.2	Reactionless motion of the manipulator model: (a) the pre-dominant wrist motion and (b) the elbow folding motion.	48

4.3	Inspection task using the hand-held camera: (a) target satellite to be refueled or captured and (b) own-satellite attached devices.	49
4.4	Simulation result under the satellite observation mission (Fig. 4.3 (a)).	52
4.5	Simulation result under the inspection of own-satellite mounted devices (Fig. 4.3 (b)).	53
4.6	An example of the algorithmic singularity within the proposed method.	56
4.7	Simulation results under the damped least-squares inverse with numerical filtering.	58
4.8	Simulation results under the singularity consistent method. . .	60
4.9	A motion obtained via the 3-Phase method.	61
4.10	The simulation results under the 3-phase method: (a) the joint velocity and (b) the coupling angular momentum.	63
4.11	The snapshot of the motion obtained via the 3-phase method.	64
4.12	The base attitude deviations under the all methods: (a) 3-phase method, (b) JS-C, (c) IJ-C and (d) TJ-C.	65
4.13	Motion snapshots from the deployment task under reactionless motion control.	67
4.14	The snapshot of the motion under partial reactionless deployment.	68
4.15	The snapshot of the motion under the conventional joint space interpolation.	69
5.1	The distribution of the cost function with the two-DoF model.	74
5.2	This figure shows how the average of C_{ratio} is affected by parameter variation.	75

5.3	The disutribution of cost function with the four-DoF spatial manipulator model: (a) regularly appearing distribution $(\theta_1, \theta_2) = (-3.05, 0.403)$ rad and (b) near the singularity $(\theta_1, \theta_2) = (-\pi, 0)$ rad.	76
5.4	An example of energy consumption comparison.	79
5.5	Comparison of energy consumption under five conditions . . .	80
6.1	Model of n -link manipulator model and its $n + 1$ link control model for the RNS-based controller.	86
6.2	Three-link planar redundant manipulator: (a) real model and (b) control model.	93
6.3	Simulation results of end-effector position and force. The position error is along x -direction, while the force error is represented along z direction, in the end-effector frame.	95
6.4	Simulation results of the joint variables.	96
6.5	Simulation model based on the arm of Rollin' Justin.	98
6.6	Motion control direction is along x axis, while force control direction is along z axis, in the end-effector frame $\{E\}$	99
6.7	Simulation results of end-effector position and force measured in the inertial frame.	100
6.8	Simulation results of joint-space behavior.	101
7.1	The time profiles of the joint velocity and the null-space velocity: the upper part represents the joint velocity; the lower part is the null-space velocity, respectively.	104
7.2	A geometrical interpretation of the RNS constraint: (a) with a small mass of the constrained link and (b) with a large value of the mass.	107
7.3	The root means square of the motion error.	108

- 7.4 Time profile of the Euclidean norm of the null-space velocity:
the line in red represents the velocity based acceleration solution; the line in green stands for the velocity with the damper. 111

List of Tables

4.1	Dynamic model parameters	46
4.2	The maximum value of the base deviation.	64

Chapter 1

Introduction

1.1 Space robots

The first use of a robotic system in space is the Shuttle Remote Manipulator System (SRMS), whose nickname is *Canadarm* (Fig. 1.1 (a)), on Space Shuttle Colombia in 1981 [1]. After that, robotic systems have been employed in various space missions. A well-known space robot is the Space Station Remote Manipulator System (SSRMS) developed by the Canadian Space Agency (CSA). The manipulator was named *Canadarm 2* and has performed several missions, successfully; the most recent mission executed by Canadarm 2 is a catching mission of the H-II Transfer Vehicle (Fig. 1.1 (b)). Canadarm 2 consists of 17-meter long, 7 degree-of-freedom (DoF) symmetric mechanism. As a similar robotic system, the Japan Aerospace Exploration Agency (JAXA) developed the Japanese Experiment Module Remote Manipulator System (JEMRMS) and a small fine arm (SFA) attached on the end of JEMRMS; hence, the combined system has been referred to as JEMRMS/SFA (Fig. 1.1 (c)).

In addition to this kind of space robotic system, free-floating space robots (FFSR), which consists of a satellite base and at least one manipulator arm, are expected to perform future space missions. These missions would be

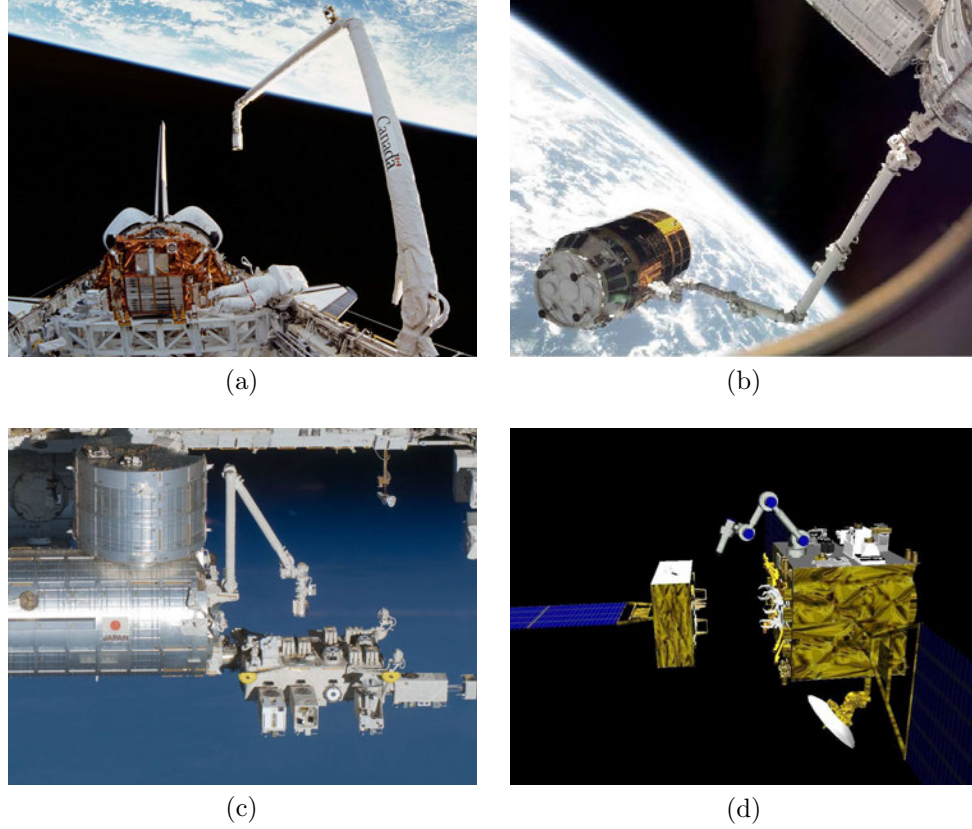


Fig. 1.1: Space robotic systems: (a) Canadarm ©NASA, (b) Canadarm 2 ©NASA, (c) JEMRMS ©JAXA and (d) ETS-VII.

debris removal, construction of large space buildings, servicing for launched satellites and so on. So far, this type of space robots have not been used in practical missions. On the other hand, an experimental robotic system was developed by JAXA around 1997. The robotic system has been referred to as the *Experimental Test Satellite VII* (ETS-VII) [2]. ETS-VII consists of a 2-meter long, 6-DoF manipulator and a 2000 kg class of unmanned satellite (Fig. 1.1 (d)). The system demonstrated some important robotic technologies: autonomous rendezvous and docking (AR&D) and robotic servicing. The robotic servicing includes exchange of orbital replacement unit (ORU),

deployment of a space structure and capturing of a target satellite. As an important results, it was confirmed that the manipulator motions actually induced base motions as indicated from the mechanics theory [3–5]. Hence, specific controller designs for space robots have to be developed in order to execute future space missions, successfully.

1.1.1 Control issues with FFSR

The most significant problem when controlling manipulators in space is the dynamic coupling between the manipulators and the satellite base. The coupling induces a base translation and also rotation. Because of the base motions, control methods that have been employed in terrestrial robots cannot be applied straightforwardly. To overcome this problem, the information of the base motions has to be taken into account within the control schemes.

An important study considering the above issue was done in [4, 6]. The authors proposed the Generalized Jacobian, which includes a base motion estimated from the linear/angular momentum conservation laws. By using the Jacobian, the correct mapping from task space into the joint space can be obtained. This method can be applied simply by replacing the conventional Jacobian matrix with the generalized one on the terrestrial robot controllers. The resolved motion rate control and the resolved acceleration control with the Generalized Jacobian were verified through numerical simulation. In addition, on the experiment with ETS-VII, the utility of the generalized Jacobian was confirmed under resolved motion rate control [5].

On the other hand, a base rotation itself is a problem because it induces a communication failure between the space robot and the ground control center. To overcome this problem, using gas-jet thrusters were considered by some researchers [7]. On the experiment of ETS-VII, under a camera inspection type of mission, the thrusters were used to stabilize the base attitude. However, the fuel for thrusters is finite and its amount determines

the life duration of the space systems. Therefore, attitude devices using electric power such as reaction wheels have been considered so far [8, 9]. Reaction wheels have been successfully used on zero momentum type of various satellites to stabilize their attitude especially against the gravity gradient torque, earth magnetism torque and solar radiation pressure. However, if it is considered that reaction wheels are used to compensate the base reaction induced by a manipulator motion, the output torque of the reaction wheels is quite insufficient with respect to the base reaction. To avoid saturation of the reaction wheel signals, the manipulator has to be driven at very low speed. When some repeatable tasks, e.g. observation/inspection or assembly for construction missions are performed, this low speed manipulation is not desirable from the perspective of work efficiency [6]. Hence, developing a control method that generates a manipulator motion inducing a small reaction is an important issue for space robots.

A pioneering work on manipulator reaction control with free-floating manipulator systems introduced the Disturbance map concept [7, 10]. The base disturbance magnitude is visualized as a colored map in joint space. With this tool, low reaction paths can be obtained in an intuitive manner. However, it is difficult to employ this method with manipulators of more than two degrees of freedom (DoFs). In addition, it is difficult to obtain a low reaction motion through the color map, automatically.

1.1.2 Reactionless motion control

A motion generation method was proposed for zero reaction manipulation. This method has been referred to as the *Reaction Null-Space* (RNS) formulation [11–13], and provides a straightforward approach to reactionless motion generation. Therein, the condition of reactionless motion was derived from the angular momentum conservation law. The method was confirmed at the on-orbit experiment with ETS-VII [14].

In the previous studies, reactionless motion controls based on RNS have been considered by several researchers [15–17]. For instance, the angular momentum distribution control for capturing non-cooperative satellites under the reactionless condition was proposed [18]. The capability of the method was investigated with a planar model. With a dual arm planar model, point-to-point (PTP) reactionless motion control was considered for capturing space debris [19]. For vibration suppression of flexible appendages on a satellite, reactionless motion control of the end-effector was considered in addition to the vibration suppression control [15]. In these studies, position control of the end-effector under reactionless motion was focused on. However, the position control between arbitrary locations would be impossible on general type of spatial manipulators, e.g. six-DoF and seven-DoF redundant manipulators, due to the limitation of these kinematic structures. In fact, the above methods were verified with planar models only.

The possibility of using the RNS method with spatial models is still uncertain, despite the reports on some interesting results. For example, within the extended ETS-VII mission, simple reactionless tasks were examined [14, 20]. Also, results from simulations with a modified ETS-VII manipulator model were presented [14]. In the latter study it was concluded that kinematic redundancy is important for the extension of the workspace under reactionless control. For point-to-point position control, the reaction-null/Jacobian transpose controller was proposed in [21]. This method was verified with a dual arm manipulator system, each manipulator comprising six DoFs. In this work, it was shown that the reachable region of the end-effector from an initial configuration is quite narrow due to the limitation of the kinematic structure. On the other hand, a singularity treatment method (the Singularity Consistent approach) was applied to deal with algorithmic singularities introduced by the reactionless motion constraint [22]. It was also confirmed that the workspace of the end-effector becomes quite narrow when consider-

ing constraints imposed on both end links, the end-effector and the base. In summary, we can conclude that position control of the end-effector under reactionless control is not appropriate in practical tasks even if singularity treatment techniques are used.

1.1.3 Energy consumption

As a different issue in space systems, energy consumption has been considered. In the case of controlling satellite attitude, a power minimization control with redundant reaction wheels were proposed in [23]. From the perspective of tool design, a low-power image payload was discussed [24, 25]. In that study, Control Moment Gyros (CMG) were employed because their mechanical power/energy is smaller than those produced by a reaction wheel assembly.

On the other hand, in the field of robotics, a control method that reduces the energy consumption of free-flying space robots was proposed [26]. The study assumed that the base attitude is controlled through four reaction wheels. Then, the redundant reaction wheel was used to reduce the energy consumption throughout a manipulator motion. In [27], the mechanical power was used as a cost function that is to be minimized.

On reactionless motion control, the energy optimum reactionless path planning was proposed [28]. The method utilized redundancy to optimize the kinetic energy of dual manipulators. However, a rapid change of the joint velocities was observed due to the optimization.

As mentioned in [24], reaction wheels require high amount of mechanical power when a large output torque is generated. Generally, when reaction wheels are used to compensate the base reaction induced by a manipulator motion, the reaction wheels must generate a high output torque. Consequently, the energy consumption becomes large. On the other hand, reactionless motion control does not necessarily need to use reaction wheels com-

pletely. Hence, it is possible to reduce the energy consumption without an additional optimization that usually induces unstable behaviors. The reduction of the energy consumption when using reactionless motion control has not been discussed before. In this work, we focus on the energy consumption reduction and show an interesting result.

1.2 Motion/Force control

With terrestrial robots, force control of the end-effector is as important as motion control. Especially under interaction tasks, whose typical examples are polishing, deburring, machining or assembly in industrial settings, force control providing a compliance behavior is crucial due to a safe contact between the end-effector of a manipulator and the unstructured environments. To understand the importance of the compliance behavior, we consider a situation that an interaction task is executed by a motion control scheme. In this case, the contact between a manipulator and the environment may cause a deviation of the end-effector motion from the desired trajectory. Then, an appropriate position feedback controller should intend to reduce the deviation. As a result, a built-up of the contact force may occur until causing breakage of a part of the manipulator. Hence, the compliance behavior of the manipulator end-effector must be needed.

This compliance behavior can be obtained through passive/active interaction control approaches. The passive approach makes use of a specifically designed mechanical device such as the Remote Center of Compliance (RCC) device. This device is designed and has been used for peg-into-hole like tasks. From the perspective of response time, the use of a passive device is more suitable than the use of active control approaches. However, in order to use the passive approach in industrial applications, specific mechanical devices have to be designed for every robot task. In addition, the passive devices can

only deal with small position and orientation deviations. Hence, to provide flexibility in robotic tasks, active interaction control has to be developed.

The active interaction control schemes can be classified into two categories: indirect force control and direct force control. Impedance control is a well-known scheme belonging to the first category. Under impedance control, the behavior of the end-effector is modeled as an equivalent mass-spring-damper system with adjustable parameters. With the model, the contact force of the end-effector can be related to the deviation of the end-effector motion from the desired one.

On the other hand, hybrid motion/force control belonging to the second category has been developed. The most well-known approach is the so-called *Operational Space* (OS) formulation, which provides the dynamics of a manipulator in task-space coordinates. If the system is non-redundant, the task-space coordinates are actually the generalized coordinates of the system. However, with redundant manipulators, the task-space coordinates cannot be generalized coordinates because there is infinite possibility providing a relation between the task-space and the joint-space coordinates. Hence, a suitable transformation between the task-space and joint-space has to be chosen. To obtain a relation between the two spaces, the inertia-weighted generalized inverse has been used in various studies [29–32]. The inversion provides a decoupled feature between the task-space and the null-space. This character is suitable to design task/joint spaces control systems independently of each other. While task space behavior under the OS formulation (the inertia weighted generalized inverse) seems to be feasible, unstable behaviors have been observed in joint space [33,34]. In addition, the dynamics of joint-space is to be hidden under the OS formulation. As a result, the gravity compensation might cause a cyclic joint motion without affecting the task-space behavior.

Because of these drawbacks of the OS formulation, we proposed a new

motion/force control scheme based on the Reaction Null Space (RNS) formulation, which has been used for space robots, especially for redundant manipulators [35]. The formulation can represent the dynamics in task-space coordinates without making use of a transformation between the two spaces. In addition, the joint motion is explicitly presented in the task-space dynamics. Comparing with the OS formulation, we confirmed that the RNS-based control would have an advantages in terms of joint motion [35]. In this work, we provide a depth discussion of the joint motion under the RNS-based control that has been unclear so far.

1.3 Aim of this study

This thesis treats the following two topics for the RNS-based controls: (i) reactionless motion control for free-floating space robots and (ii) motion/force control for fixed-base redundant manipulators.

On reactionless motion control of free-floating space robots, we discuss the following issues:

- i-1** Analysis of reactionless motion from the perspective of nonlinear dynamics.
- i-2** Proposal of some practical tasks suitable for execution under reactionless motion control.
- i-3** Analysis of the energy consumption under reactionless motion control.

On the RNS-based motion/force control, we treat the following topics:

- ii-1** Obtain a specific model for the RNS-based motion/force control.
- ii-3** Clarify the joint motion under the RNS-based motion/force control.

1.4 Outline of this thesis

This thesis consists of the eight chapters as follows: Chapter 2 describes the modeling of free-floating base robot systems. The equation of motion of the system is derived from the Euler-Lagrange's equation. Then, linear and angular momentum conservation laws are derived via considering the invariance of the system Lagrangian with translation and rotation of the entire system. Finally, we present the Reaction Null-Space formulation in terms of both momentum and dynamics.

In Chapters 3 to 5, we deal with reactionless motion control of free-floating space robots. In Chapter 3, we provide an analysis of reactionless motion with a planar two-DoF model from the perspective of nonlinear dynamics: vector field, fixed point and bifurcation. Besides, with a seven-DoF redundant manipulator, we obtain a representation of its reactionless motion that is useful to consider for practical reactionless tasks.

Chapter 4 discusses motion tasks suitable for execution under reactionless motion control. We propose the following three tasks: (i) inspection task using a hand camera, (ii) point-to-point positioning task, (iii) deployment task from a stowed configuration. The performance of these tasks is verified via numerical simulations.

In Chapter 5, we deal with the energy consumption of free-flying space robots, comparing that produced by reactionless motion control with that produced by reaction wheels used controllers. Under zero base attitude deviation, we show that reactionless motion coincides with the instantaneous energy minimum motion to a high degree. Then, the energy consumption of reactionless motion control is compared with a conventional controller using reaction wheels under the inspection tasks.

In the next two chapters, we deal with the motion/force control based on the Reaction Null-Space for fixed base redundant manipulators. In Chap-

ter 6, we formulate the RNS-based motion/force control. Then, a specific model for the RNS-based controller is presented. Finally, the performance of the proposed method is verified through numerical simulation.

Chapter 7 discusses the joint motion under the RNS-based motion/force control. We show an interesting fact that the joint motion under the RNS-based controller is equivalent to that under the resolved acceleration control. The theoretical derivation and numerical verification are obtained.

Finally, Chapter 8 summarizes this thesis.

1.5 The roles of variable's index

Basically, we describe vectors and matrices according to the following roles of the indexes. *Left superscript*: reference frames in which quantities are described. *Right superscript*: conditions of variables, e.g. T (Transposed), -1 (Inversion), *des* (Desired), *ref* (Reference) and so on. *Right subscript*: physical quantities, component, manipulator mechanisms and so on.

We provide two examples according to the above roles, in what follows. First, we consider the Jacobian \mathbf{J} associated with end-effector linear velocity \mathbf{v}_e with respect to the inertial coordinate frame $\{F\}$. This matrix is written as ${}^I\mathbf{J}_{v_e}$.

Next, we consider the same Jacobian but it just consists of the positioning subchain P , which is a specific part of a manipulator mechanism. This matrix is written as ${}^I\mathbf{J}_{Pv_e}$. Note that if we consider the whole mechanism of a manipulator, we omit this notation. And also note that the notation of the inertial coordinate frame is omitted below.

Chapter 2

Basic Notation

In this section, we describe the equation of motion of a free-floating base robot. We derive the equation through the Euler-Lagrange's equation. Then, we show that the linear/angular conservation laws, which play an important role in robotics, can be derived from the equation of motion with assuming invariance of the system Lagrangian under translation and rotation of the entire system. From linear/angular momentum conservation laws, we obtain the Reaction Null-Space formulation that is useful for reactionless motion control of space robots and also motion/force control of redundant manipulators.

2.1 Modeling of free-floating base robots

We consider a free-floating base robot that consists of a floating base and links, e.g. manipulators and reaction wheels, as shown in Fig. 2.1. Let us define the inertial coordinate frame $\{F\}$. We use two kind of position vector. One of them is vector from the inertial frame; the other is one from the base coordinate frame $\{B\}$. Note that, except special cases these vectors are described with respect to the inertial frame.

Here, we introduce generalized coordinate to describe the system dynamics.

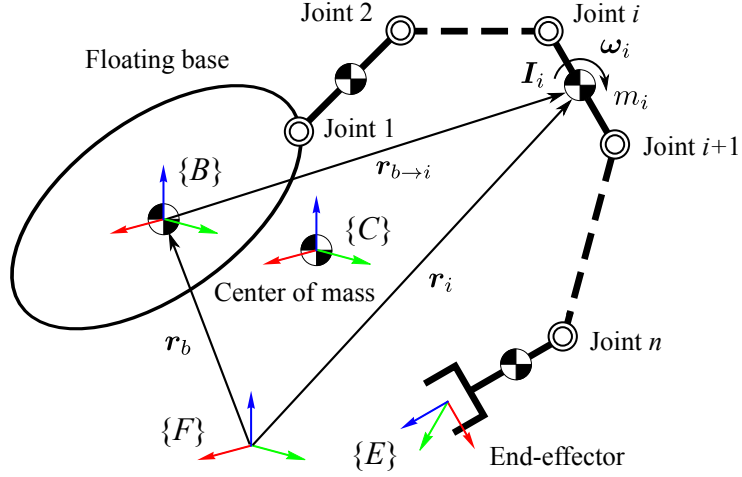


Fig. 2.1: General model of free-floating base robot.

The coordinate is defined as $\mathbf{q} = [\mathcal{X}_b^T \boldsymbol{\theta}^T]^T \in \mathbb{R}^{n+6}$, where $\mathcal{X}_b = [\mathbf{r}_b^T \boldsymbol{\xi}_b^T]^T \in \mathbb{R}^6$ stands for the base variables: $\mathbf{r}_b \in \mathbb{R}^3$ and $\boldsymbol{\xi}_b$ are base position vector and Euler angle describing the base attitude; especially we make use of Roll-Pitch-Yaw angle. $\boldsymbol{\theta} \in \mathbb{R}^n$ is the joint variable vector. Note that because of the non-integrability of angular velocity, the base spatial velocity $\mathcal{V}_b = [\mathbf{v}_b^T \boldsymbol{\omega}_b^T]^T$ cannot be obtained as the time-differential of \mathcal{X}_b . Hence, an appropriate transformation between the time-differential of the Euler angle and the angular velocity is needed:

$$\dot{\boldsymbol{\xi}}_b = \mathbf{A}^{-1} \boldsymbol{\omega}_b \quad (2.1)$$

where $\mathbf{A} \in \mathbb{R}^{3 \times 3}$ is the transformation matrix.

2.1.1 Kinematics

Seen from Fig. 2.1, the position vector of each link can be written as follows:

$$\mathbf{r}_i = \mathbf{r}_b + \mathbf{r}_{b \rightarrow i} \quad (2.2)$$

where \mathbf{r}_i , $\mathbf{r}_{b \rightarrow i}$ are the position vectors pointing to the center of mass of each link from the inertial frame and the base frame, respectively. Differentiating (2.2) with respect to time t , we can obtain the differential kinematic equation:

$$\mathbf{v}_i = \mathbf{v}_b + \mathbf{J}_{v_i}(\mathbf{q})\dot{\boldsymbol{\theta}} + [\boldsymbol{\omega}_b^\times] \mathbf{r}_{b \rightarrow i} \quad (2.3)$$

where \mathbf{v}_i stands for linear velocity of link i , \mathbf{v}_b , $\boldsymbol{\omega}_b \in \mathbb{R}^3$ are linear and angular velocities of the base. $\mathbf{J}_{v_i}(\mathbf{q}) \in \mathbb{R}^{3 \times n}$ is the Jacobian for linear velocity of the link i CoM. $(\dot{})$ and $(\circ)^\times$ define time differential and skew-symmetric matrix.

In contrast to the linear velocity equation, the kinematic equation of angular velocity cannot be obtained directly as the time differential of the position-level equation because of its non-integrability. The angular velocity of link i is expressed in the following form:

$$\boldsymbol{\omega}_i = \boldsymbol{\omega}_b + \mathbf{J}_{\omega_i}(\mathbf{q})\dot{\boldsymbol{\theta}} \quad (2.4)$$

where $\boldsymbol{\omega}_i$ stands for angular velocity of link i , $\mathbf{J}_{\omega_i}(\mathbf{q}) \in \mathbb{R}^{3 \times n}$ is the Jacobian associated with the angular velocity of link i .

2.1.2 Kinetic energy

The kinetic energy of the free-floating base robots is represented as follows:

$$T = \frac{1}{2} \sum_{i=0}^n (m_i \mathbf{v}_i^T \mathbf{v}_i + \boldsymbol{\omega}_i^T \mathbf{I}_i \boldsymbol{\omega}_i) \quad (2.5)$$

where T is kinetic energy, m_i and $\mathbf{I}_i \in \mathbb{R}^3$ are the mass and the inertia tensor of each link. Substituting (2.3) and (2.4) into the above equation, we can rewrite the kinetic energy in terms of the base and the joint variables:

$$T = \frac{1}{2} \dot{\mathbf{q}}^T \mathbf{M}(\mathbf{q}) \dot{\mathbf{q}} \quad (2.6)$$

$$= \frac{1}{2} \begin{bmatrix} \mathcal{V}_b^T & \dot{\boldsymbol{\theta}}^T \end{bmatrix} \begin{bmatrix} \mathbf{M}_b(\mathbf{q}) & \mathbf{M}_{bl}(\mathbf{q}) \\ \mathbf{M}_{bl}(\mathbf{q})^T & \mathbf{M}_l(\mathbf{q}) \end{bmatrix} \begin{bmatrix} \mathcal{V}_b \\ \dot{\boldsymbol{\theta}} \end{bmatrix} \quad (2.7)$$

where $\mathbf{M}(\mathbf{q}) \in \mathbb{R}^{(n+6) \times (n+6)}$ is the inertia matrix of the entire mechanism. $\mathbf{M}_b(\mathbf{q}) \in \mathbb{R}^{6 \times 6}$, $\mathbf{M}_{bl}(\mathbf{q}) \in \mathbb{R}^{6 \times n}$ and $\mathbf{M}_l(\mathbf{q}) \in \mathbb{R}^{n \times n}$ are the submatrices of the inertia matrix; \mathbf{M}_b is the inertia matrix of the system regarded as a Composite-Rigid-Body (CRB), \mathbf{M}_{bl} is a block submatrix of the system inertia matrix. This matrix represents a dynamic coupling between base motion and link motion. Hence, it has been referred to as the *coupling inertia* matrix, and plays an important role under controlling space robots. Finally, \mathbf{M}_l denotes the manipulator inertia matrix.

2.1.3 Inertia submatrices

Here, we provide the definitions of the inertia submatrices. The matrix \mathbf{M}_b is defined in the following form:

$$\mathbf{M}_b = \begin{bmatrix} \mathbf{M}_v & \mathbf{M}_{v\omega} \\ \mathbf{M}_{v\omega}^T & \mathbf{M}_\omega \end{bmatrix} \quad (2.8)$$

$$\mathbf{M}_v = m_c \mathbf{E} \quad (2.9)$$

$$\mathbf{M}_{v\omega} = - \sum_{i=1}^n m_i [\mathbf{r}_{b \rightarrow i}^\times] \quad (2.10)$$

$$\mathbf{M}_\omega = \sum_{i=1}^n (\mathbf{I}_i + m_i [\mathbf{r}_{b \rightarrow i}^\times]^T [\mathbf{r}_{b \rightarrow i}^\times]) + \mathbf{I}_b \quad (2.11)$$

where $m_c = \sum_{i=0}^n m_i$ is the total mass of the system, m_i and $\mathbf{I}_i \in \mathbb{R}^3$ is the mass and the inertia tensor of link i . $\mathbf{E} \in \mathbb{R}^{3 \times 3}$ is the identity matrix.

The coupling inertia matrix \mathbf{M}_{bl} is defined as follows:

$$\mathbf{M}_{bl} = \begin{bmatrix} \mathbf{M}_{vl} \\ \mathbf{M}_{\omega l} \end{bmatrix} \quad (2.12)$$

$$\mathbf{M}_{vl} = \sum_{i=1}^n m_i \mathbf{J}_{v_i} = m_c \mathbf{J}_c \quad (2.13)$$

$$\mathbf{M}_{\omega l} = \sum_{i=1}^n (\mathbf{I}_i \mathbf{J}_{\omega_i} + m_i [\mathbf{r}_{b \rightarrow i}^\times] \mathbf{J}_{v_i}) \quad (2.14)$$

where $\mathbf{J}_c \in \mathbb{R}^{3 \times n}$ is the Jacobian matrix for the CoM velocity of the system; hence it is referred to as the CoM Jacobian.

Finally, \mathbf{M}_l is described as follows:

$$\mathbf{M}_l = \sum_{i=1}^n (m_i \mathbf{J}_{v_i}^T \mathbf{J}_{v_i} + \mathbf{J}_{\omega_i}^T \mathbf{I}_i \mathbf{J}_{\omega_i}) \quad (2.15)$$

Note that this matrix is the same as the manipulator inertia matrix of fixed base robots.

2.1.4 Equation of motion

Since we consider free-floating systems, the gravity potential is approximately zero. Hence, the system Lagrangian coincides with the kinetic energy:

$$L(\mathbf{q}, \dot{\mathbf{q}}) = T(\mathbf{q}, \dot{\mathbf{q}}) \quad (2.16)$$

where $L(\mathbf{q}, \dot{\mathbf{q}})$ is the system Lagrangian.

From the theory of analytical mechanics, equation of motions of dynamic system can be obtained from the partial derivation of the system Lagrangian. Then, equation of motions satisfy the following equation:

$$\frac{d}{dt} \left(\frac{\partial L}{\partial \dot{\mathbf{q}}} \right) - \frac{\partial L}{\partial \mathbf{q}} = \mathbf{Q} \quad (2.17)$$

where \mathbf{Q} is generalized force vector acting on each generalized coordinate.

Substituting (2.7) and (2.16) into (2.17), we can obtain the equation of motion of a free-floating base robot in the following form:

$$\mathbf{M}_b \dot{\mathbf{V}}_b + \mathbf{M}_{bl} \ddot{\boldsymbol{\theta}} + \mathbf{C}_b = \mathbf{0} \quad (2.18)$$

$$\mathbf{M}_{bl}^T \dot{\mathbf{V}}_b + \mathbf{M}_l \ddot{\boldsymbol{\theta}} + \mathbf{c}_l = \boldsymbol{\tau} \quad (2.19)$$

where $\boldsymbol{\tau} \in \mathbb{R}^n$ is joint torque acting on each joint, $\mathbf{C}_b \in \mathbb{R}^6$ and $\mathbf{c}_l \in \mathbb{R}^n$ are nonlinear dependent forces of the base and the links. These nonlinear forces

are represented in the following form:

$$\mathbf{c} = \begin{bmatrix} \mathcal{C}_b \\ \mathcal{C}_l \end{bmatrix} = \dot{\mathbf{M}}\dot{\boldsymbol{\theta}} - \frac{1}{2} \frac{\partial}{\partial \mathbf{q}} \left(\dot{\mathbf{q}}^T \mathbf{M} \dot{\mathbf{q}} \right) \quad (2.20)$$

Equation (2.18) represents the dynamics of the composite rigid-body (CRB); (2.19) describes the same dynamics with respect to the local coordinate frames.

2.2 Momentum conservation law

2.2.1 Linear momentum conservation law

In the field of robotics, linear and angular momenta and their conservation laws play an important role. In particular, these provide the reactionless motion constraint for space robots; in the field of humanoids, these are used to built balancing controllers and also whole body motion controllers. Considering the invariance of the system Lagrangian under variations of position and rotation of a dynamic system, we can obtain the conservation laws in what follows.

First, we derive the linear momentum conservation law of free-floating base robots. Empirically, we know that physical laws is not changed with translation of dynamic systems; the translation indicates that the whole part of the system move in the same direction, simultaneously.

We assume that the system consists of $n+1$ bodies like manipulator mechanisms. The position vectors pointing to each body are defined as \mathbf{r}_i . Then, under a variation of translation $\delta \mathbf{r}_i$, the variation of the system Lagrangian can be written as follows:

$$\delta L = \sum_{i=0}^n \frac{\partial L}{\partial \mathbf{r}_i} \delta \mathbf{r}_i \quad (2.21)$$

Because the variation of the Lagrangian must be zero with an arbitrary value of $\delta \mathbf{r}_i$, the following condition must satisfy:

$$\sum_{i=0}^n \frac{\partial L}{\partial \mathbf{r}_i} = \mathbf{0} \quad (2.22)$$

According to (2.17), the above condition is equivalent to the following equation:

$$\sum_{i=0}^n \frac{d}{dt} \left(\frac{\partial L}{\partial \dot{\mathbf{r}}_i} \right) = \mathbf{0} \quad (2.23)$$

where $\sum \frac{\partial L}{\partial \dot{\mathbf{r}}_i}$ is an invariable and $\mathbf{p}_i = \frac{\partial L}{\partial \dot{\mathbf{r}}_i}$ is defined as *linear momentum*. Hence, (2.23) represents the linear momentum conservation law. Using the same expression of (2.5), the conservation law can be written in the following well-known form:

$$\mathbf{p} = \sum_{i=0}^n m_i \mathbf{v}_i \quad (2.24)$$

In the case of free-floating base robots, a variation of translation can be considered as the base position vector $\delta \mathbf{r}_b$. Then, the linear momentum conservation law of free-floating base robots can be obtained as:

$$\frac{d}{dt} \left(\frac{\partial L}{\partial \mathbf{v}_b} \right) = \mathbf{0} \quad (2.25)$$

This is equivalent to the following equation:

$$\mathbf{p} = \mathbf{M}_v \mathbf{v}_b + \mathbf{M}_{v\omega} \boldsymbol{\omega}_b + \mathbf{M}_{v\dot{\boldsymbol{\theta}}} \dot{\boldsymbol{\theta}} \quad (2.26)$$

The above expression of the conservation law has been used in various studies.

2.2.2 Angular momentum conservation law

We derive the angular momentum conservation law of free-floating base robots. In contrast to linear momentum conservation law, angular momentum conservation law is obtained from invariance of the system Lagrangian under an infinitesimal rotation of dynamic systems.

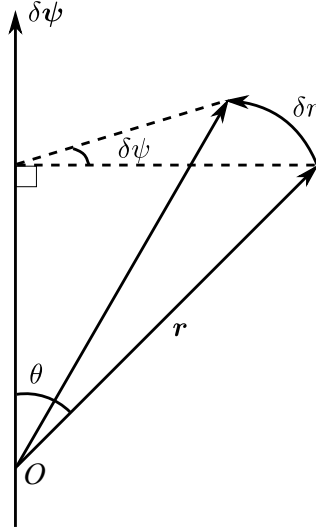


Fig. 2.2: Relationship between a variation of translation and a rotational variation.

First, we derive, also, the general form of angular momentum conservation law. We introduce an infinitesimal rotation vector $\delta\boldsymbol{\psi}$. Then, a position vector pointing to an arbitrary particle of a rotating system varies according to $\delta\boldsymbol{\psi}$. The position variation is written as follows (see Fig. 2.2):

$$\|\delta\mathbf{r}\| = r \sin \alpha \|\delta\boldsymbol{\psi}\| \quad (2.27)$$

Under an arbitrary infinitesimal rotation, the velocity of each body also varies. The variation of the velocity is written as:

$$\delta\mathbf{v} = \delta\boldsymbol{\psi} \times \mathbf{v} \quad (2.28)$$

With the above relation, the variation of the system Lagrangian under an

infinitesimal rotation can be written as:

$$\begin{aligned}
 \delta L &= \sum_{i=0}^n \left\{ \dot{\mathbf{p}}_i (\delta \boldsymbol{\psi}^T \mathbf{r}_i) + \mathbf{p}_i (\delta \boldsymbol{\psi}^T \mathbf{v}_i) \right\} \\
 &= \delta \boldsymbol{\psi} \frac{d}{dt} \sum_{i=0}^n \mathbf{r}_i \times \mathbf{p}_i \\
 &= 0
 \end{aligned} \tag{2.29}$$

Because $\delta \boldsymbol{\psi}$ can be an arbitrary value, the following condition must be satisfied:

$$\frac{d}{dt} \sum_{i=0}^n \mathbf{r}_i \times \mathbf{p}_i = \mathbf{0} \tag{2.30}$$

Hence, we found out that the quantity $\sum \mathbf{r}_i \times \mathbf{p}_i$ conserves; $\mathbf{l}_F = \mathbf{r}_i \times \mathbf{p}_i$ is defined as *angular momentum*, where $(\circ)_F$ represent the angular momentum with respect to the inertial frame $\{F\}$. Using the same expression of (2.5), we can rewrite the angular momentum conservation law in the following form:

$$\mathbf{l}_F = \sum_{i=0}^n \left\{ \mathbf{I}_i \boldsymbol{\omega}_i + m_i \mathbf{r}_i \times \mathbf{v}_i \right\} \tag{2.31}$$

In the case of free-floating robots, this equation can be expressed as:

$$\mathbf{l}_F = \mathbf{M}_{v\omega}^T \mathbf{v}_i + \mathbf{M}_\omega \boldsymbol{\omega}_b + \mathbf{M}_{\omega l} \dot{\boldsymbol{\theta}} + \mathbf{r}_b \times \mathbf{p} \tag{2.32}$$

2.3 Reaction Null-Space

Reaction Null-Space was originally proposed for reactionless motion control of space robots. With the ETS-VII experiment, the possibility of reactionless motion control was confirmed. In what follows, we describe the Reaction Null-Space formulation in terms of both momentum and dynamics.

2.3.1 Momentum based derivation

The spatial momentum conservation law is obtained in the following form:

$$\mathcal{L}_B = \mathbf{M}_b \mathcal{V}_b + \mathbf{M}_{bl} \dot{\boldsymbol{\theta}} \quad (2.33)$$

where $\mathcal{L}_B = [\mathbf{p}^T \mathbf{l}_B^T]^T$ is spatial momentum with respect to the base frame $\{B\}$. From the above equation, we can confirm that there are two partial momenta: $\mathbf{M}_b \mathcal{V}_b$ represents the partial momentum related to base motion; $\mathbf{M}_{bl} \dot{\boldsymbol{\theta}}$ is stemming from manipulator motion. In particular, the later one has been referred to as the *coupling momentum*, and is characterized by the coupling inertia matrix.

Solving (2.33) for joint velocity, we can obtain a joint-space decomposition in terms of the dynamic coupling as follows:

$$\dot{\boldsymbol{\theta}} = \mathbf{M}_{bl}^+ (\mathcal{L}_B - \mathbf{M}_b \mathcal{V}_b) + \mathbf{P}_{RNS} \dot{\boldsymbol{\theta}}_a \quad (2.34)$$

where $(\circ)^+$ defines pseudoinverse matrix, $\mathbf{P}_{RNS} = \mathbf{E} - \mathbf{M}_{bl}^+ \mathbf{M}_{bl} \in \mathbb{R}^{n \times n}$ is the projector onto the null-space of the coupling inertia matrix. $\dot{\boldsymbol{\theta}}_a \in \mathbb{R}^n$ is an arbitrary vector with dimensions of joint velocity. The first term represents joint velocities inducing a base motion; on the other hand, the second term does not impose any motion at the base. Hence, the motions are referred to as *reactionless motion*. Since the property of pseudoinverse, the above two terms are orthogonal with any values of $(\mathcal{L}_B - \mathbf{M}_b \mathcal{V}_b)$ and $\dot{\boldsymbol{\theta}}_a$. This joint space decomposition has been referred to as *Reaction Null-Space* in terms of momentum.

2.3.2 Dynamics based derivation

Let us recall the equation of motion (2.18), as follows:

$$\mathbf{M}_b \dot{\mathcal{V}}_b + \mathbf{M}_{bl} \ddot{\boldsymbol{\theta}} + \mathbf{C}_b = \mathbf{0} \quad (2.35)$$

From the above equation, we can also see that there is a coupling between the base dynamics and the manipulator one through the coupling inertia matrix. Through the same approach under the momentum-based derivation, the Joint dynamics can be divided into two parts in the following form:

$$\ddot{\boldsymbol{\theta}} = \mathbf{M}_{bl}^+(\mathbf{M}_b\dot{\mathcal{V}}_b - \mathcal{C}_b) + \mathbf{P}_{RNS}\dot{\boldsymbol{\theta}}_a \quad (2.36)$$

The first term on the r.h.s. represents joint accelerations inducing a base motion, the second term defines reactionless acceleration, whose meaning is the same as the momentum derivation. Note that the motions of (2.34) and (2.36) are not basically equivalent, since there is non-integrability between the two formulations; this non-integrability is due to the pseudoinverse.

2.4 Summary

In this section, we described the equation of motion of a free-floating base robots from the Euler-Lagrange formulation. We showed the two important conservation laws, which are linear and angular momentum conservation law, with assuming invariance of the system Lagrangian under variation of position and orientation of dynamic systems. Then, we derived the Reaction Null-Space formulation with dimensions of both momentum and dynamics. Joint velocity/acceleration can be divided into two parts through the inertia coupling matrix. The first part is a motion set inducing a base motion, the second part does not effect the base motion. Hence, the second one is referred to as reactionless motion. Based on this formulation, we will describe reactionless motion of a free-floating space manipulator and motion/force control for redundant manipulators, in the following sections.

Part I

Reactionless Motion Control

Chapter 3

Review of Reactionless Motion and Analysis

3.1 Reactionless motion control

We consider a free-flying space robot model consisting of a satellite base and a serial manipulator arm of n -DoF. In space environment, it is known that linear and angular momenta are conserved when there is no external force. Actually, the gravity gradient torque and solar radiation force violate this conservation. However, since the duration time of space robot missions is relatively short, we can assume that the momenta are conserved. Motion of a free-floating space robot is described via the spatial momentum conservation law as follows:

$$\begin{bmatrix} \mathbf{p} \\ \mathbf{l}_B \end{bmatrix} = \begin{bmatrix} \mathbf{M}_v & \mathbf{M}_{v\omega} \\ \mathbf{M}_{v\omega}^T & \mathbf{M}_\omega \end{bmatrix} \begin{bmatrix} \mathbf{v}_b \\ \boldsymbol{\omega}_b \end{bmatrix} + \begin{bmatrix} \mathbf{M}_{vm} \\ \mathbf{M}_{\omega m} \end{bmatrix} \dot{\boldsymbol{\theta}} \quad (3.1)$$

In this case, the link part represents a manipulator. Hence, we make use of the subscript $(\circ)_m$ to represent “manipulator”.

For free-flying space manipulators, the angular momentum conservation law, especially, is of primary importance. Indeed, it has been noted that even slight variations of the base attitude may cause a failure in the communication between the robot and the ground control center. The angular

momentum conservation law can be written in the following form, when zero initial momentum is assumed:

$$\mathbf{l}_B = \tilde{\mathbf{M}}_\omega \boldsymbol{\omega}_b + \tilde{\mathbf{M}}_{\omega m} \dot{\boldsymbol{\theta}} \quad (3.2)$$

where the notation $(\tilde{\circ})$ represents a quantity that includes the base linear motion effect: $\tilde{\mathbf{M}}_\omega = \mathbf{M}_\omega - \mathbf{M}_{v\omega}^T \mathbf{M}_v^{-1} \mathbf{M}_{v\omega}$, $\tilde{\mathbf{M}}_{\omega m} = \mathbf{M}_{\omega m} - \mathbf{M}_{v\omega}^T \mathbf{M}_v^{-1} \mathbf{M}_{vm}$. In the above equation, the first term on the r.h.s. is the partial angular momentum stemming from base rotation. The second term results from manipulator motion: it represents the base disturbance in terms of momentum and is referred to as the *coupling angular momentum* [13].

To deal with the reaction problem, reactionless motion control can be a useful approach. Reactionless motions are variations of the manipulator configuration that conserve a zero initial base angular momentum throughout a manipulator motion. As explained already in Chapter 2, these motions are obtained from the null-space vectors of the coupling inertia matrix. Then, reactionless motion velocities are obtained as:

$$\dot{\boldsymbol{\theta}} = \mathbf{P}_{RNS} \dot{\boldsymbol{\theta}}_a \quad (3.3)$$

The velocities, of course, satisfy the following equation:

$$\tilde{\mathbf{M}}_{\omega m} \dot{\boldsymbol{\theta}} = \mathbf{0} \quad (3.4)$$

The above equation implies the reactionless constraint.

Because $\dot{\boldsymbol{\theta}}_a$ is projected onto $\ker(\tilde{\mathbf{M}}_{\omega m})$, any values of $\dot{\boldsymbol{\theta}}_a$ satisfy the reactionless constraint (3.4). The main concern of this study is how to make use of reactionless motions in practice. Before proceeding with the discussion of the practical usages, we should examine the features of reactionless motion. The following section provides an analysis on reactionless motion with a planar model.

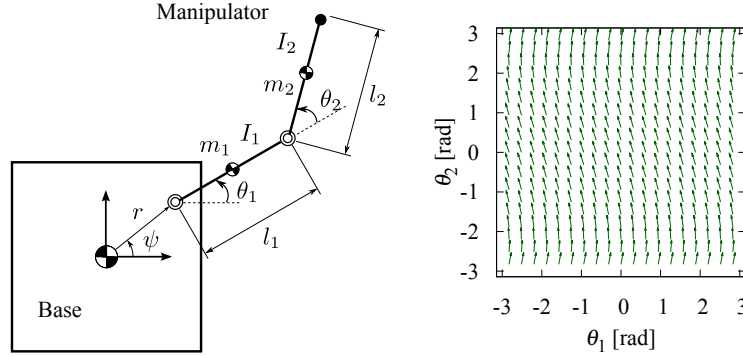


Fig. 3.1: A planar two-DoF space manipulator model with $m_i = 100$ kg, $l_i = 1.0$ m ($i = 1, 2$); the base mass is $m_b = 1000$ kg. The vector field is obtain with $r = 0$ m.

3.2 Qualitative study of reactionless motion

3.2.1 Vector field of reactionless motion

Existing results from reactionless motion control have been reported in the Introduction. There are, however, some characteristics of reactionless motion that have not been mentioned so far.

Consider first a simple planar two-DoF manipulator on a satellite base, as shown in Fig. 3.1. This model is the simplest one with the capability of reactionless motion generation. Reactionless motion with this model can be represented as follows:

$$\dot{\boldsymbol{\theta}} = b\mathbf{n}(\boldsymbol{\theta}) \quad (3.5)$$

where $\mathbf{n}(\boldsymbol{\theta}) \in \mathbb{R}^2$ is the only generic null-space vector in the kernel of the coupling inertia matrix, and b is an arbitrary scalar dimensioned as joint velocity. $\mathbf{n}(\boldsymbol{\theta})$ can be uniquely obtained through appropriate methods, i.e. Singular Value Decomposition (SVD) or the co-factor method. We assume that $\mathbf{n}(\boldsymbol{\theta})$ is already normalized, and b is a time-independent constant scalar, for the sake of simplicity. Hence, (3.5) can be regarded as an autonomous

nonlinear system. The right hand side in (3.5) defines the vector field of reactionless motion in joint space.

For the sake of simplicity, we assume that the manipulator is attached at the CoM of the base. The mass and inertia moment of the base are $m_b = 1000$ kg, $I_b = 667$ kgm²; the length, mass and inertia moments of the links are $l_i = 1.0$ m, $m_i = 100$ kg and $I_i = 8.33$ kgm² ($i = 1, 2$), respectively. The resultant vector field is depicted in Fig. 3.1. Because the manipulator is attached symmetrically, the vector field has rotational symmetry w.r.t. Joint 1. From the vector field, an important property becomes apparent: reactionless motion is predominantly composed of Joint 2 motion. Because reactionless motion conserves angular momentum at zero (or at a constant), motion in the joints that induce a large angular momentum cannot vary significantly. With this model, the angular momentum induced by Joint 1 motion must be larger than that of Joint 2 due to the large inertia moment and the long moment arm. As a result, the above mentioned behavior is observed.

3.2.2 Fixed point and bifurcation

In the above example, the system does not have any fixed points. It turns out, however, that the variation of the manipulator attachment position induces such points and moreover, a bifurcation can be observed. The attachment position is made variable according to:

$$\begin{bmatrix} x_a \\ y_a \end{bmatrix} = r \begin{bmatrix} \cos \psi \\ \sin \psi \end{bmatrix} \quad (3.6)$$

where r is the distance between the attachment position and the base CoM, and ψ is the angle as shown in Fig. 3.1. Among these parameters, r plays an important role as a *bifurcation parameter* in this system. Note that we can assume $\psi = 0$ because this parameter does not influence the topological structure of the system due to the existing rotational symmetry. Hence, it

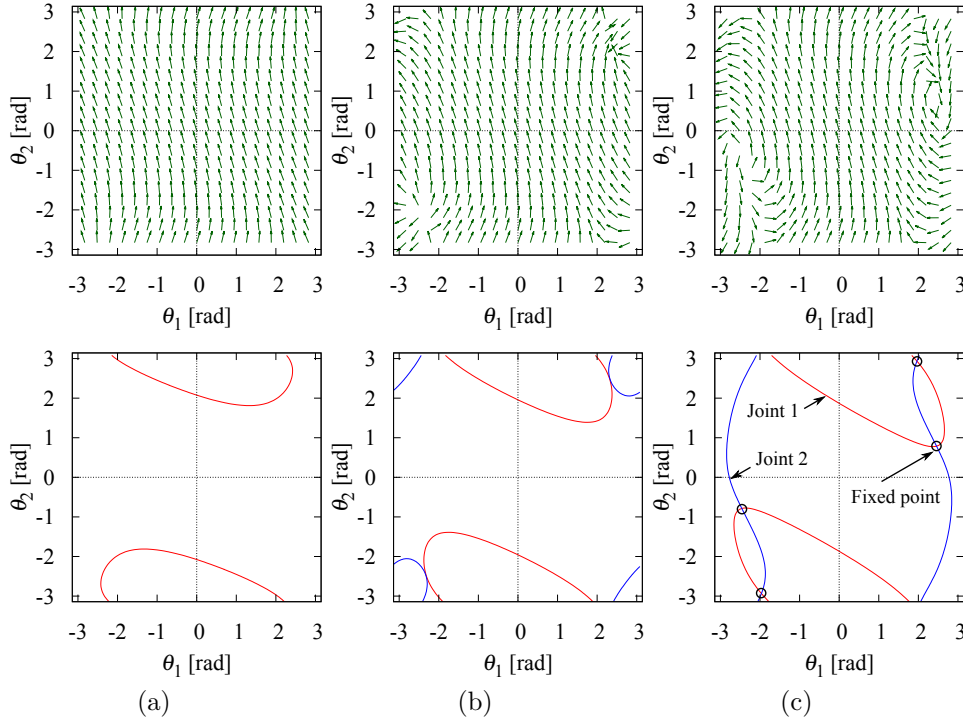


Fig. 3.2: The vector field and nullclines for each joint direction when r varies as: (a) $r = 0.5$ m, (b) $r = 0.945$ m and (c) $r = 1.5$ m.

is sufficient to variate the attachment position along the x -axis of the base frame.

In Fig. 3.2, the vector field and nullclines for several values of r are shown. In the figures, the upper part represents the vector field and the lower part depicts nullclines for each joint direction: the lines in red are for Joint 1, those in blue are for Joint 2. When $r = 0.5$ m, we can see that there is no fixed point, because the motion of Joint 2 never stops at any point in joint space. On the other hand, the occurrence of a bifurcation can be observed when $r \approx 0.945$ m. Then, two fixed points are created at the intersection points of the two nullclines. Further increase of the bifurcation parameter ($r = 1.5$ m) leads to separation of the created fixed points. Finally, when

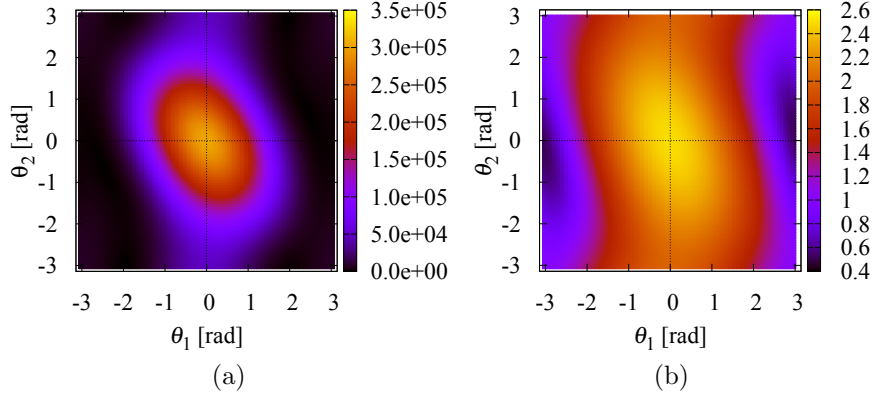


Fig. 3.3: This figure shows the determinant of $(\mathbf{M}_{\omega m} \tilde{\mathbf{M}}_{\omega m}^T)$ and the distance between the manipulator CoM and the base one as color map: (a) $\det(\tilde{\mathbf{M}}_{\omega m} \tilde{\mathbf{M}}_{\omega m}^T)$ and (b) the distance between the manipulator CoM and the base one.

$r \rightarrow \infty$, two of the fixed points converge to $\theta_2 \rightarrow 0$ rad and the rest to $\theta_2 \rightarrow \pm\pi$ rad.

3.2.3 Rank deficiency of the coupling inertia matrix

In above discussion, we clarified the existence of fixed points with regard to reactionless motion. This phenomenon is related to the rank deficiency of the coupling inertia matrix. In contrast to kinematic singularities, the singularities of the coupling inertia matrix have not been discussed, so far. We provide some insight with the planar model mentioned above.

Determinant $\det(\tilde{\mathbf{M}}_{\omega m} \tilde{\mathbf{M}}_{\omega m}^T)$ for $r = 1.5$ m is shown as a colored map in Fig. 3.3 (a). The determinant takes large values at the bright areas, while the most dark area represents the singularities. It is apparent that the determinant takes its maximum value at $\boldsymbol{\theta} = \mathbf{0}$. This is an extended-arm configuration s.t. the manipulator CoM is located farthest away from the base CoM. Note that determinant $\det(\tilde{\mathbf{M}}_{\omega m} \tilde{\mathbf{M}}_{\omega m}^T)$ can be related to the distance between the two CoMs as shown in Fig. 3.3 (b). Comparing the

two plots in Fig. 3.3, it can be seen that the determinant takes large values whenever the distance is relatively large. Large CoM distance yields large moment of momentum and hence, large magnitude of the coupling angular momentum. Furthermore, note that there is no fixed point within the area where the distance is large. In the case of a spatial model, the directions of the joint axes play an important role in addition to the above qualitative characteristics.

3.3 Summary

In this chapter, we described some characters of reactionless motion with a planar model. From a qualitative analysis, we found out that the manipulator attachment position plays an important role in terms of bifurcation. Then, through vector field, we confirmed that the fixed points of reactionless motion are generated, increasing the length between the manipulator attachment position and the base CoM.

Chapter 4

Proposal of Reactionless Tasks

In this chapter, we discuss motion tasks suitable for execution under reactionless motion control, with a seven-DoF redundant manipulator. First, we will show that the reactionless motion of the model consists of the predominant wrist and elbow motion. Based on these motions, we propose the following three tasks [36]: (i) inspection task using a hand-held camera, (ii) point-to-point position control, (iii) deployment task from a stowed configuration. The performance of these tasks are verified via numerical simulation.

4.1 Manipulator model

4.1.1 Model description

We consider a free-flying space robot model consisting of a satellite base, and a serial-link seven-DoF kinematically redundant manipulator. The manipulator is characterized by a kinematic chain with a distinctive lower/upper arm subchain, including a rotational “elbow” joint, a “shoulder” and a “wrist” joint, all of them with offsets. The kinematic structure and simulation model are displayed in Fig. 4.1. The manipulator attachment position is determined from the ETS-VII design, at $[-0.79 \ -0.29 \ 1.0]^T$ m with respect to the base CoM coordinate frame [5]. The dynamic model parameters are shown in

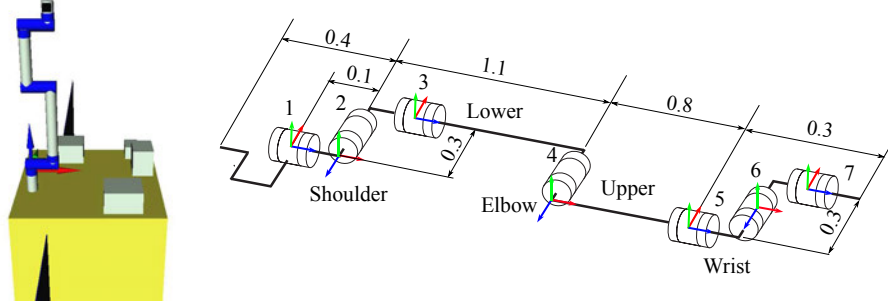


Fig. 4.1: Our manipulator model with seven-DoF mechanism at the initial configuration ($\theta_i = 0 \text{ rad}, \forall \theta_i$).

Table 4.1: Dynamic model parameters

i	Mass [kg]	Inertia moment [kgm ²]		
	m_i	I_{xi}	I_{yi}	I_{zi}
1	30.0	0.0671	0.0671	0.0851
2	30.0	0.0843	0.267	0.267
3	45.0	3.81	3.81	0.127
4	40.0	0.113	2.19	2.19
5	20.0	0.213	0.213	0.0250
6	20.0	0.0250	0.0292	0.0292
7	25.0	0.0990	0.0990	0.0313

Tab. 4.1.

4.1.2 Reactionless motion representation

Before proceeding with the analysis of the reactionless motion task, we have to identify the reactionless motion capability with the manipulator model. First, note that the DoF of reactionless motion is four, which is obtained as the difference between the number of joints (seven) and the base attitude variables (three). The following discussion provides a useful representation of the four-DoF reactionless motion.

For the analysis, we divide the kinematic chain into two subchains: the positioning subchain comprising joints 1 through 4, and the wrist subchain comprising the rest of the joints. Then, we focus on the amplitude of the angular momentum produced by each of the two subchains. Because of the serial-link structure, the wrist subchain is characterized with relatively small mass and length of the moment arm.

Dividing joint velocity into the positioning and wrist subchain related terms, we can rewrite the reactionless constraint as follows:

$$\tilde{\mathbf{M}}_{P\omega m}\dot{\boldsymbol{\theta}}_P + \tilde{\mathbf{M}}_{W\omega m}\dot{\boldsymbol{\theta}}_W = \mathbf{0} \quad (4.1)$$

where $\dot{\boldsymbol{\theta}} = [\dot{\boldsymbol{\theta}}_P \ \dot{\boldsymbol{\theta}}_W]$, $\tilde{\mathbf{M}}_{\omega m} = [\tilde{\mathbf{M}}_{P\omega m} \ \tilde{\mathbf{M}}_{W\omega m}]$; $(\circ)_P$ and $(\circ)_W$ represent the quantities related to the positioning and wrist subchains. In the above equation, the first term is the partial angular momentum produced by the positioning subchain; the second term is stemming from the wrist subchain.

Next, we focus on the amplitude of these angular momentum. Because of the small mass and the length of moment arm of the wrist subchain, the angular momentum produced by the motion of the wrist subchain will be far smaller than that obtained from the positioning subchain. Therefore, we can assume that the positioning subchain can compensate the base disturbance induced by the wrist subchain motion, completely. This implies one particular reactionless motion patterns, characterized with “unconstrained” wrist motion plus small compensating variations in the positioning subchain, as shown in Fig. 4.2 (a). This motion is a three-DoF reactionless motion and is referred to as the *predominant wrist motion*, hereafter. This motion can be obtained as follows:

$$\dot{\boldsymbol{\theta}} = \begin{bmatrix} \mathbf{B}(\boldsymbol{\theta}) \\ \mathbf{E} \end{bmatrix} \dot{\boldsymbol{\theta}}_W \quad (4.2)$$

where $\mathbf{B} = -\tilde{\mathbf{M}}_{P\omega m}^+ \tilde{\mathbf{M}}_{W\omega m} \in \mathbb{R}^{4 \times 3}$ is a linear map from the wrist subchain motion to the positioning subchain motion ensuring the reactionless constraint.

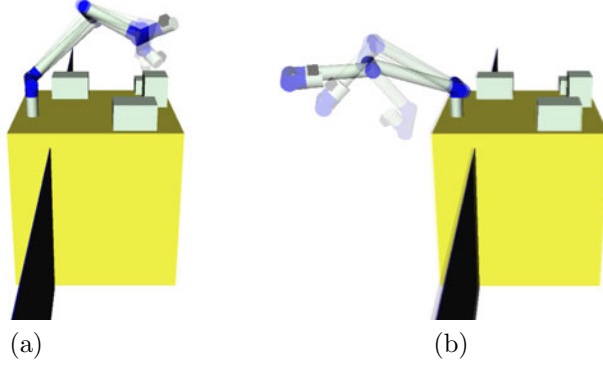


Fig. 4.2: Reactionless motion of the manipulator model: (a) the predominant wrist motion and (b) the elbow folding motion.

The remaining one-DoF reactionless motion is uniquely determined from the null-space vector of the coupling inertia submatrix that is related to the positioning subchain $\tilde{\mathbf{M}}_{\omega m P}$.

$$\dot{\boldsymbol{\theta}} = b \begin{bmatrix} \mathbf{n}(\boldsymbol{\theta}) \\ \mathbf{0} \end{bmatrix} \quad (4.3)$$

where b is an arbitrary scalar. From the angular momentum conservation, we can assume that motions in Joints 1 and 2 will be relatively small for the above two reactionless motion patterns. Hence, this motion approximately consists of the elbow folding/unfolding motion as shown in Fig. 4.2 (b).

Since these two patterns are orthogonal, their superposition will represent all possible reactionless motions for the given manipulator model, as follows:

$$\dot{\boldsymbol{\theta}} = \begin{bmatrix} \mathbf{B}(\boldsymbol{\theta}) \\ \mathbf{E} \end{bmatrix} \dot{\boldsymbol{\theta}}_w + b \begin{bmatrix} \mathbf{n}(\boldsymbol{\theta}) \\ \mathbf{0} \end{bmatrix} \quad (4.4)$$

From the above analysis, we can then arrive at the following conclusion: because the end-effector position largely depends on the motion in the positioning subchain, it follows that under reactionless motion, the positioning DoF of end-effector will be approximately one. This feature results only

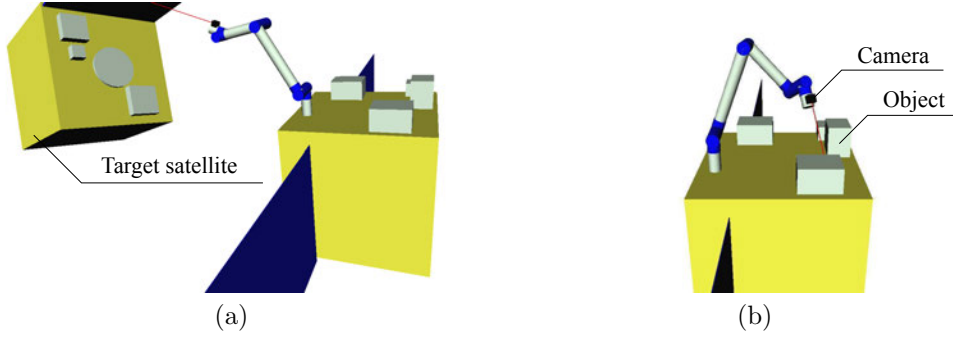


Fig. 4.3: Inspection task using the hand-held camera: (a) target satellite to be refueled or captured and (b) own-satellite attached devices.

from the specific kinematic structure of the positioning subchain, comprising two upper/lower arm links (i.e. it is similar to the two-link planar example discussed previously). Therefore, we will henceforth focus on reactionless end-effector orientation control with the predominant wrist motion and reactionless manipulator configuration control. This makes our research different from previous studies.

Based on the two type of reactionless motions, we propose the following three tasks for reactionless motion: (i) inspection task using a hand-held camera, (ii) point-to-point positioning task and (iii) deployment task from a stowed configuration. First, we describe the inspection task in what follows.

4.2 Inspection task using a hand-held camera

One frequently appearing task for free-floating space robots is inspection with a hand-held camera of devices mounted on the own satellite base or on the satellite to be serviced, as shown in Fig. 4.3. Such task was also performed within the ETS-VII mission [2] but without using reactionless control. For camera inspection, once the arm is positioned appropriately, the camera view angle for inspection is changed by rotating the wrist. This task

is expected to be performed multiple times during a number of missions, such as construction, maintenance, debris removal and so on. Hence, this task is a good candidate for execution under reactionless motion control for improved work efficiency.

The following three control subtasks are considered necessary to accomplish camera inspection.

1. Reactionless constraint of the base attitude (three-DoF).
2. Orientation control of the wrist (three-DoF).
3. Stabilization of the wrist position.

The first control subtask ensures reactionless motion. The second one is essential for camera inspection. The third control subtask is necessary to avoid a large deflection of the wrist from the initial position, since there is no position control subtask. The above subtasks will be simultaneously realized through consecutive null-space projections [37, 38], known also as the task-of-priority approach [39]. Priorities are assigned among the tasks according to their relative importance. A higher-priority task can then be accomplished without being disturbed from the lower-priority tasks. This is ensured by projecting lower-priority tasks onto the common null-space of all higher-priority tasks.

4.2.1 Control command

The priorities are assigned as follows. The reactionless constraint is the highest-priority subtask, wrist orientation control is the second-priority one and wrist position stabilization is the lowest-priority subtask. The control command for the joint velocity can then be obtained as follows:

$$\dot{\boldsymbol{\theta}}^{ref} = \bar{\mathbf{J}}_{\omega_e}^+ \boldsymbol{\omega}_e^{ref} + k_g \mathbf{P} \mathbf{J}_{v_w}^T \Delta \mathbf{p}_w \quad (4.5)$$

where $\boldsymbol{\omega}_e \in \mathbb{R}^3$ is the angular velocity of the end-effector and $\Delta \mathbf{p}_w (= \mathbf{p}_w - \mathbf{p}_w^{init}) \in \mathbb{R}^3$ is the wrist deflection from the initial position. Matrix $\bar{\mathbf{J}}_{\omega_e} = [\mathbf{J}_{\omega_e} \mathbf{P}_{RNS}] \in \mathbb{R}^{3 \times 7}$ is the restricted Jacobian matrix [40] for the wrist subtask. Matrices $\mathbf{J}_{\omega_e}, \mathbf{J}_{v_w} \in \mathbb{R}^{3 \times 7}$ stand for the Jacobians w.r.t. the angular/linear velocity of the end-effector, respectively. $\mathbf{P} = \mathbf{P}_{RNS}(\mathbf{E} - \bar{\mathbf{J}}_{\omega_e}^+ \bar{\mathbf{J}}_{\omega_e})$ is the combined null-space projector for the lowest-priority task. k_g is a positive gradient gain.

The structure of the control command is as follows. The first term is the end-effector orientation control projected onto the null-space of the coupling inertia matrix: this term can accomplish the end-effector orientation control under the reactionless constraint. The second term minimizes the following potential function to stabilize the wrist position:

$$V = \frac{1}{2} \|\Delta \mathbf{p}_w\|^2. \quad (4.6)$$

This term does not disturb the higher priority tasks because it is projected onto the null-space of all higher priority tasks. It should be noted that $\bar{\mathbf{J}}_{\omega_e}^+$ may become rank-deficient. This is an algorithmic singularity which occurs when the end-effector and reactionless motion control subtasks are in conflict. The details of this singularity will be described, below.

4.2.2 Numerical simulation

In what follows, we examine the performance under (4.5) by comparing it to that under a conventional inverse Jacobian controller that keeps the positioning subchain motionless:

$$\dot{\boldsymbol{\theta}}_W^{ref} = \mathbf{J}_{W\omega_e}^{-1} \boldsymbol{\omega}_e^{ref} \quad (4.7)$$

$$\dot{\boldsymbol{\theta}}_P^{ref} = \mathbf{0} \quad (4.8)$$

We assume the following two task scenarios for observing: (i) a satellite to be serviced (Fig. 4.3 (a)) and (ii) the devices attached on satellite base

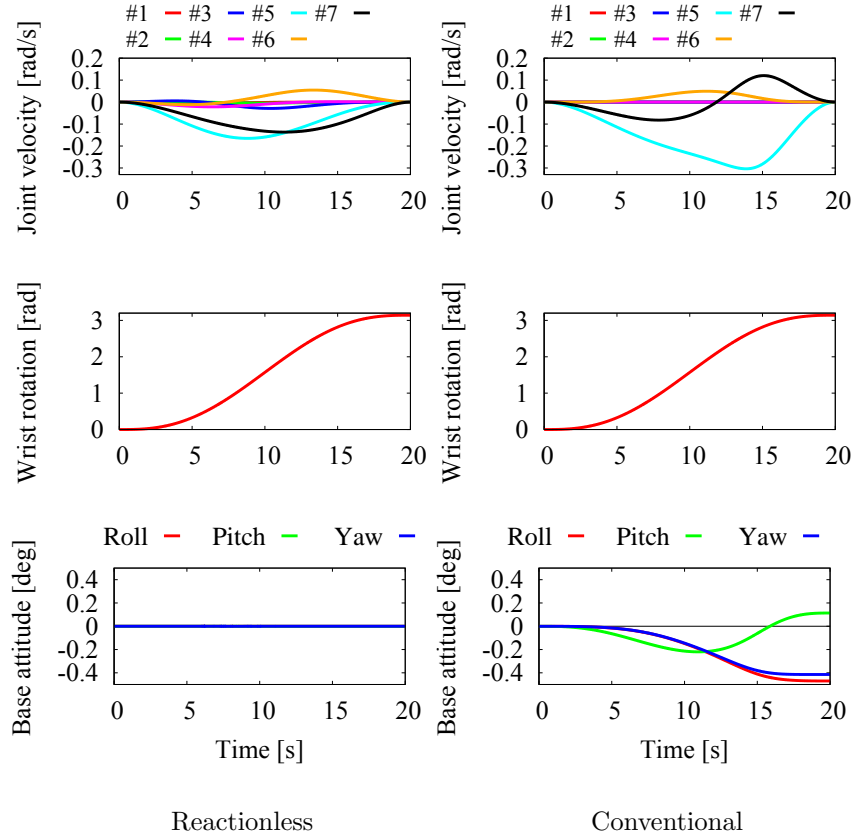


Fig. 4.4: Simulation result under the satellite observation mission (Fig. 4.3 (a)).

(Fig. 4.3 (b)). First, we verify the satellite observation case. The initial configuration is set as $[-90 \ -30 \ 0 \ -70 \ 180 \ -30 \ 0]^T$ deg as shown in Fig. 4.3 (a), the reference angular velocity is $\omega_e^{ref} = \pi[s(t) \ 0 \ 0]^T$, where $0 \leq s(t) \leq 1$ denotes a fifth-order spline function. The simulation time and the gain are set at 20 s and $k_g = 100 \text{ kg/m} \cdot \text{s}$, respectively. The simulation results are displayed in Fig. 4.4. From the angular velocity error graphs is can be seen that the end-effector task is accomplished successfully in both simulations. Note, however, that under reactionless motion control there is

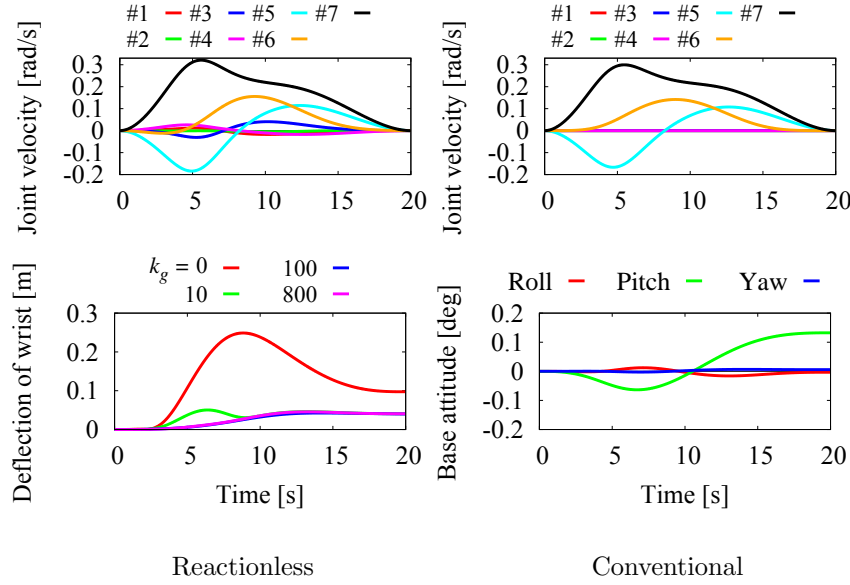


Fig. 4.5: Simulation result under the inspection of own-satellite mounted devices (Fig. 4.3 (b)).

no base attitude deviation. Also, this motion is realized with a relatively small displacement of the positioning subchain, according to the respective joint velocity graph. In contrast, under the conventional control method there is a relatively large base attitude deviation¹, despite the low inertia parameters of the wrist.

In the second scenario, we assume that the initial configuration is set to $[90 \ -20 \ 180 \ 110 \ 0 \ 20 \ 0]^T$ deg as shown in Fig. 4.3 (b), the desired end-effector velocity is $\omega_e^{ref} = \pi[0 \ 0 \ -s(t)]^T$ rad/s. The other conditions are the same as in the previous simulation. The simulation results are shown in Fig. 4.5. First, it becomes apparent that also in this case, the base remains undisturbed under reactionless motion while under conventional control, a relatively large base attitude deviation is observed. Under reactionless mo-

¹The maximum allowable base attitude deviation for the ETS-VII mission was about ± 0.05 deg.

tion, the effect of the cost function leads to a sufficiently small deviation from the initial wrist position as shown in Fig. 4.5.

In summary, a somewhat surprising result was obtained with the conventional controller: a relatively large base attitude deviation was observed despite the small mass and inertia moment of the wrist subchain. We can then conclude that reactionless camera inspection is useful to overcome this problem.

4.3 Singularities within the inspection task

4.3.1 Problem statement

In this section, we deal with possible singularities that could be encountered during the proposed reactionless task. There are three types of such singularities, as follows:

- Kinematic singularity: $\det(\mathbf{J}_{\omega_e} \mathbf{J}_{\omega_e}^T) = 0$.
- Singularities of the coupling inertia matrix: $\det(\tilde{\mathbf{M}}_{\omega_m} \tilde{\mathbf{M}}_{\omega_m}^T) = 0$.
- Algorithmic singularities: $\det(\bar{\mathbf{J}}_{\omega_e} \bar{\mathbf{J}}_{\omega_e}^T) = 0$ with non-singular \mathbf{J}_{ω_e} and full row-rank $\tilde{\mathbf{M}}_{\omega_m}$.

Kinematic singularities have been much discussed by various researchers, e.g. [41, 42]. The damped least-squares (DLS) method was applied [43, 44] to deal with these type of singularity. The infinite growth of the joint velocity in the neighborhood of a singularity can be suppressed by a suitably defined damping factor. This method, however, has some drawbacks [45]: it causes workspace errors both in speed and motion direction. In addition, the determination of the damping factor is counter-intuitive. Another method, called the Singularity Consistent method, was proposed in [46]. Under this method,

the manipulator can follow the desired path exactly, without causing a large joint velocity².

In contrast, the second and third types of singularities have not been discussed extensively, so far. Fortunately, the singularities of the coupling inertia matrix do not pose a problem here because we use the null-space of the coupling inertia matrix. Indeed, in (4.5) the rank of restricted Jacobian $\bar{\mathbf{J}}_{\omega_e}$ depends upon the conditioning of \mathbf{J}_{ω_e} only, since $\text{rank} \mathbf{P}_{RNS}$ grows when $\text{rank} \mathbf{J}_{\omega_e}$ decreases.

On the other hand, algorithmic singularities should be handled with care. There are few studies that treat this type of singularities. In [47], the algorithmic singularities of a planar six-DoF dual arm model were discussed. For reactionless motion control of flexible base robots, a singularity treatment technique was proposed in [17]. However, these two methods cannot be applied in our case.

Using SVD, the (pseudo)inverse of $\bar{\mathbf{J}}_{\omega_e}$ can be written as:

$$\bar{\mathbf{J}}_{\omega_e}^+ = \frac{1}{\sigma_1} \mathbf{v}_1 \mathbf{u}_1^T + \frac{1}{\sigma_2} \mathbf{v}_2 \mathbf{u}_2^T + \frac{1}{\sigma_3} \mathbf{v}_3 \mathbf{u}_3^T \quad (4.9)$$

where $\sigma_1 \geq \sigma_2 \geq \sigma_3$ are the singular values, $\mathbf{v}_i \in \mathbb{R}^7$, $\mathbf{u}_i \in \mathbb{R}^3$ are the left and right singular vectors associated with σ_i . In the neighborhood of a singularity where σ_3 approaches zero, the last term attains an extremely large value.

In what follows, an example of an algorithmic singularity will be presented. The initial configuration is the same as in the satellite observation task (cf. Fig. 4.3 (a)). The commanded angular velocity is however different: $\boldsymbol{\omega}_e^{ref} = [0 \ -0.2 \ 0]^T$ rad/s. The simulation results are displayed in Fig. 4.6.

In the graphs, the vertical line represents the time instant when the manipulator is passing near a singularity whereby $\det(\bar{\mathbf{J}}_{\omega_e} \bar{\mathbf{J}}_{\omega_e}^T)$ approaches zero but the other two determinants, $\det(\mathbf{J}_{\omega_e} \mathbf{J}_{\omega_e}^T)$ and $\det(\tilde{\mathbf{M}}_{\omega_m} \tilde{\mathbf{M}}_{\omega_m}^T)$, do not.

²The term “path” should be distinguished from “trajectory”: the former is characterized only geometrically while the latter includes time/velocity relations.

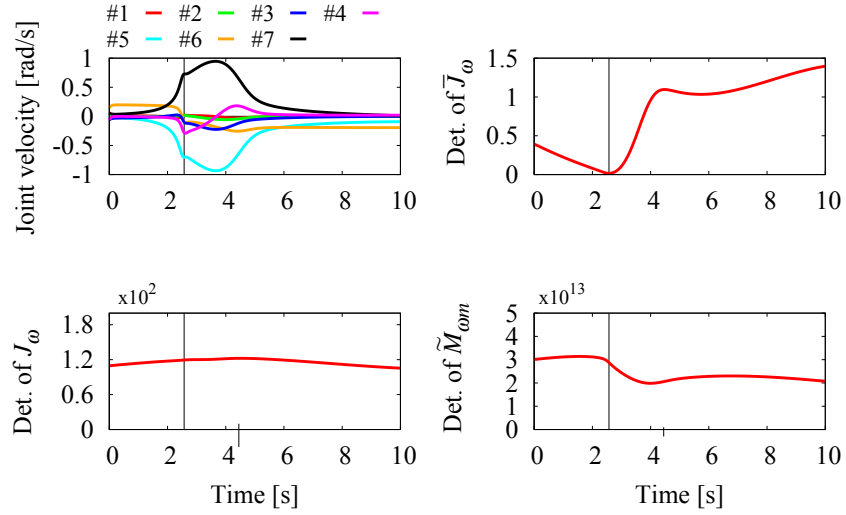


Fig. 4.6: An example of the algorithmic singularity within the proposed method.

Hence, this singularity can be recognized as an algorithmic one. From the joint velocity graphs it is seen that near the singularity, Joints 5 and 7 rotate in opposite directions with high joint rates. This type of behavior is observed at singularities of the Euler angles [48] as well as at wrist singularities [49].

From our observation, it seems that such algorithmic singularities do not occur frequently. But nevertheless, we will show that singularity treatment techniques such as the DLS and Singularity Consistent methods, can be effective w.r.t. algorithmic singularities.

4.3.2 Singularity treatment with the Damped Least-Squares inverse

Originally, the DLS generalized inverse is obtained by adding damping factors to the denominators in (4.9) to suppress high joint rates. We resume, however, to a DLS inverse that is obtained with a so-called numerical filter-

ing technique [50]. This approach can alleviate the problem of large errors. Accordingly, the generalized inverse of $\bar{\mathbf{J}}_{\omega_e}$ is obtained in the following form:

$$\bar{\mathbf{J}}_{\omega_e}^\# = \bar{\mathbf{J}}_{\omega_e}^T \left(\bar{\mathbf{J}}_{\omega_e} \bar{\mathbf{J}}_{\omega_e}^T + \lambda^2 \mathbf{u}_3 \mathbf{u}_3^T \right)^{-1} \quad (4.10)$$

where λ is a damping factor, $\mathbf{u}_3 \in \mathbb{R}^3$ is the left singular vector associated with the minimum singular value σ_3 , $(\circ)^\#$ represents the DLS inverse. Further on, through SVD (4.10) can be rewritten as:

$$\bar{\mathbf{J}}_{\omega_e}^\# = \sum_{i=1}^2 \frac{1}{\sigma_i} \mathbf{v}_i \mathbf{u}_i^T + \frac{\sigma_3}{\sigma_3^2 + \lambda^2} \mathbf{v}_3 \mathbf{u}_3^T \quad (4.11)$$

where $\sigma_1 \geq \sigma_2 \geq \sigma_3$ are the singular values of $\bar{\mathbf{J}}_{\omega_e}$ and $\mathbf{u}_i \in \mathbb{R}^3$, $\mathbf{v}_i \in \mathbb{R}^7$ are the associated left and right singular vectors. Compared with (4.9), it can be seen that the DLS inverse with numerical filtering is characterized by inserting a damping factor only into the last term, with the minimum singular value. Hence, compared to the original DLS inverse which adds damping into all terms, the error of the solution can be reduced [50]. Based on [51], the damping factor is obtained as follows:

$$\lambda^2 = \begin{cases} 0 & \varepsilon < \sigma_3 \\ \left(1 - \frac{2\sigma_3^2}{\varepsilon^2} + \frac{\sigma_3^4}{\varepsilon^4}\right) \lambda_{max}^2 & \sigma_3 \leq \varepsilon \end{cases} \quad (4.12)$$

where ε defines the singular region, which is introduced in the neighborhood of the singularity, λ_{max} sets the maximum value of the damping factor. Note that we added an additional term, the σ_3^4 related term, into (4.12) to obtain a smooth transition at the border of the singular region.

The performance of the DLS inverse for this controller is verified via numerical simulation. The simulation conditions are the same as in Section 4.3.1. The singular region is defined by $\varepsilon = 0.2$ and the maximum damping value set at $\lambda_{max}^2 = 2$. The results are displayed in Fig. 4.7. In the graphs, the singular region is indicated by the two vertical lines ($1.71 \text{ s} \leq t \leq 4.18 \text{ s}$). From

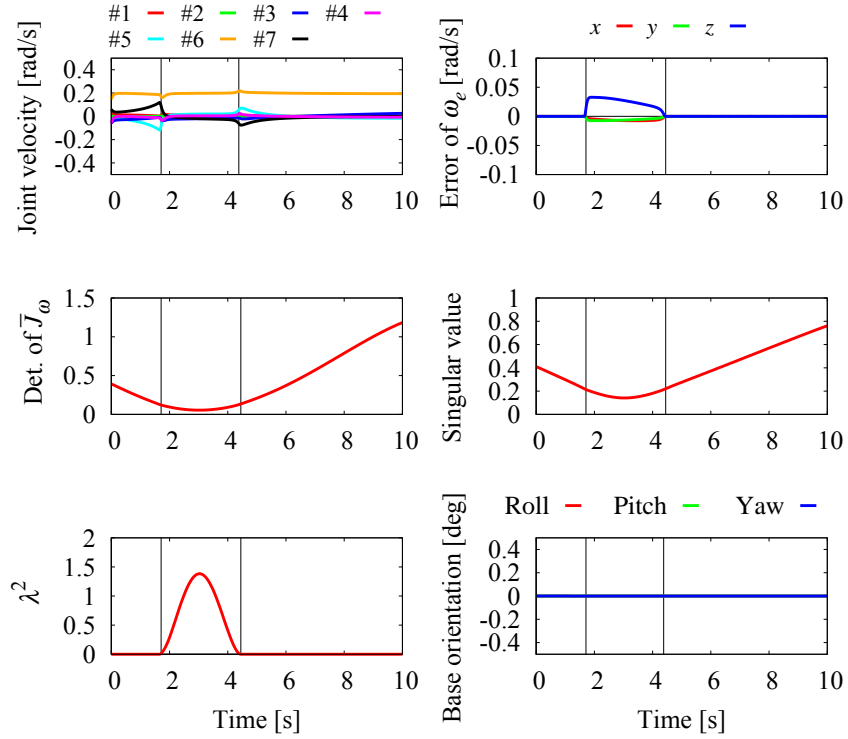


Fig. 4.7: Simulation results under the damped least-squares inverse with numerical filtering.

the results it is apparent that the growth of the joint velocity has been successfully suppressed through the damping factor. However, an end-effector tracking error can be observed within the singular region. This is caused by the damping factor, as already explained. On the other hand, the base attitude does not deviate, even within the singular region.

The Singularity Consistent method

We will examine the possibility to make use of the Singularity Consistent (SC) method for singularity treatment. It was clarified that the DLS method introduces an error in the direction of motion since the singular direction,

i.e. \mathbf{v}_3 , has to be avoided. In contrast, the SC method actively makes use of this direction and therefore, the manipulator can follow the direction of the desired end-effector velocity, correctly. An error only appears in the speed along the path. If we consider a teleoperation task, such an error is not a problem because the operator can modify the desired end-effector speed according to the task conditions. Teleoperation under the SC method is discussed in [52, 53].

We will make use of natural motion [54, 55], i.e. end-effector motion with velocity in proportion to the determinant of the Jacobian matrix. There is no need to define a singular region then, and hence, to switch the control input.

According to the SC method, the inverse of $\bar{\mathbf{J}}_{\omega_e}$ can be obtained as follows:

$$\bar{\mathbf{J}}_{\omega_e}^+ = b \sum_{i=1}^3 \mu_i \mathbf{v}_i \mathbf{u}_i^T \quad (4.13)$$

$$\mu_i = \prod_{j=1, j \neq i}^3 \sigma_j \quad (4.14)$$

where b is a constant scalar. From (4.14), we can see that μ_1 and μ_2 become small near the singularity, because their values are proportional to the minimum singular value that approaches 0 in the vicinity of the singularity. Hence, the \mathbf{v}_3 related term is actively used.

We verify the performance of this method through numerical simulation. The simulation conditions are the same as in the DLS case. Empirically, the constant scalar was set to $b = 1.7$. In addition, to avoid a large joint velocity obtained from the null-space term, we multiply the term by the determinant of $\bar{\mathbf{J}}_{\omega_e} \bar{\mathbf{J}}_{\omega_e}^T$ as follows:

$$\dot{\boldsymbol{\theta}}^{ref} = \bar{\mathbf{J}}_{\omega_e}^+ \boldsymbol{\omega}_e^{ref} + k_g \det(\bar{\mathbf{J}}_{\omega_e} \bar{\mathbf{J}}_{\omega_e}^T) \mathbf{P}(\mathbf{J}_{v_w}^T) \Delta \mathbf{p}_w \quad (4.15)$$

The simulation results are displayed in Fig. 4.8. The results show that the rapid change of the joint velocity can be avoided. In addition to this feature,

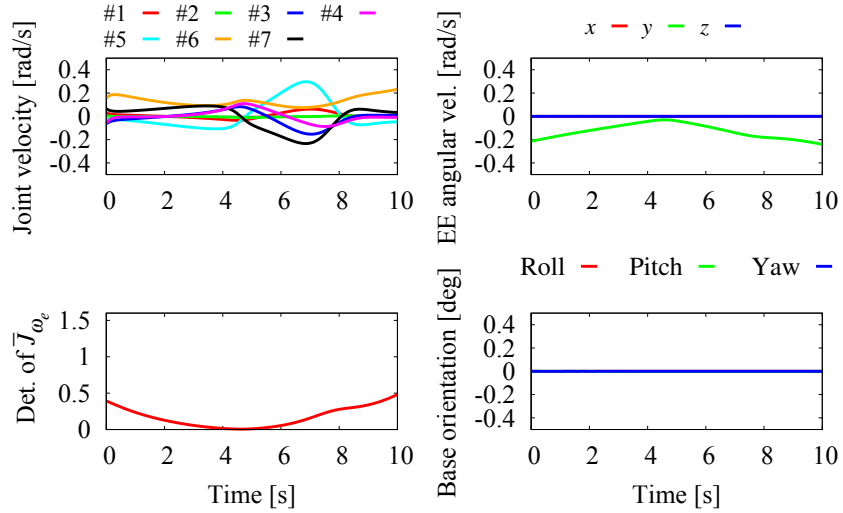


Fig. 4.8: Simulation results under the singularity consistent method.

it is seen that the end-effector follows the desired velocity direction y , which is in contrast with the result from the DLS simulation. Hence, adjustment of the speed is only needed by the operator under teleoperation.

4.4 Point-to-point positioning task

As the second reactionless task, we focus on point-to-point (PTP) positioning tasks of the end-effector. PTP positioning tasks would be used several situation such as pre-positioning task of the camera inspection, assembly and so on. Among the several positioning tasks, we restrict our attention to a specific subset of PTP tasks: arm reconfiguration tasks wherein the hand does not hold an object. It would be desirable to execute such tasks under reactionless motion control.

However, this is impossible for arbitrary points since reactionless motions are quite restricted. Nevertheless, reactionless motion can be useful if the PTP motion is planned appropriately. One possibility is to combine two

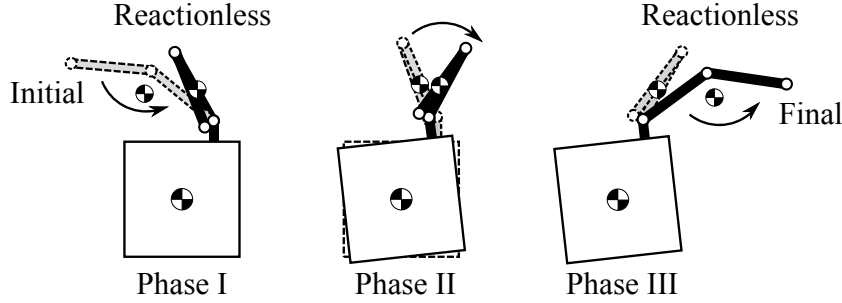


Fig. 4.9: A motion obtained via the 3-Phase method.

reactionless motions with a non-restricted PTP motion that induces the base disturbance. This method was originally proposed in [56]; it has been referred to as the *3-Phase method* and applied to a planar flexible base robots. Note that despite the advantage of the method was verified with a planar flexible base robots, the cases of free-floating base robots and also three-dimensional models have not been discussed before. We verify the performance of this method with the three-dimensional free-floating robot.

4.4.1 The 3-Phase method

First, we review the 3-Phase method. The 3-Phase method deals with the following issue: find a joint path that connects specific initial and final configurations with three sub-paths. We divide a motion into three Phase, which are Phase I, II and III, according to the three sub-paths. In Phase I and III, reactionless motion is used. In Phase II, these two reactionless motion paths are connected via a joint path that is not reactionless. The primary concern is how to determine the three sub-paths to obtain small base disturbance during the PTP sub-paths in Phase II. In [56], a folded arm configuration as shown in Fig. 4.9 was employed in Phase II. Using this configuration, the base disturbance can be reduced. We provide a theoretical argument of reaction reduction with the folded configuration in what follows. The coupling an-

gular momentum, which is the base reaction with dimension of momentum, can be represented in the following form:

$$\begin{aligned} \tilde{M}_{\omega m} \dot{\boldsymbol{\theta}} = & \left\{ \sum_{i=1}^n \mathbf{I}_i \mathbf{J}_{\omega_i} \right\} \dot{\boldsymbol{\theta}} + \\ & \left\{ \sum_{i=1}^n m_i [\mathbf{r}_{b \rightarrow i}^\times] \mathbf{J}_{v_i} \right\} \dot{\boldsymbol{\theta}} - \left\{ m_c [\mathbf{r}_{b \rightarrow c}^\times] \mathbf{J}_c \right\} \dot{\boldsymbol{\theta}}, \end{aligned} \quad (4.16)$$

It is apparent that the coupling angular momentum consists of three kinds of angular momentum. The first term represents the angular momentum induced by purely rotational motion of each link; the second and third term are the angular momentum arising from the moment of the linear momentum of each link and the CoM of the manipulator. The coefficient matrix of the first term is related to the inertia tensor of the manipulator. Hence, at the folded configuration, this term becomes the smallest value. On the other hand, the second and third term are related to the CoM positions. The base reaction related to these term also takes small amount using the folded configuration, because the distance along which the manipulator CoM moves becomes short, as shown in Fig. 4.9. In addition, the norm of $\mathbf{r}_{b \rightarrow i}$ and $\mathbf{r}_{b \rightarrow c}$ become small value at the configuration. Hence, the angular momentum related to the linear momentum of each link can be reduced. For this reason, the folded configuration is used in Phase II.

4.4.2 Verification via numerical simulations

We verify the performance of the 3-Phase method via numerical simulations, compared with several conventional controllers. The initial configuration is $[-20 \ -40 \ 0 \ -60 \ 180 \ 180 \ 0]^T$ deg; the final one is $[-120 \ 50 \ 0 \ -60 \ 180 \ 180 \ 0]^T$ deg. Note that these two configurations cannot be linked via reactionless motion. The motion in Phase I is obtained from the initial configuration toward a folded configuration (FA-1). Phase III is determined

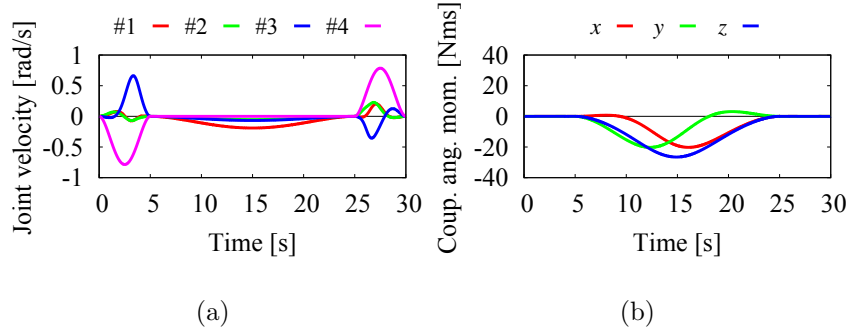


Fig. 4.10: The simulation results under the 3-phase method: (a) the joint velocity and (b) the coupling angular momentum.

as a reversed (reactionless) motion starting from the final configuration toward other folded configuration (FA-2). These two reactionless motions are obtained as the second term in (4.2) as follows:

$$\dot{\boldsymbol{\theta}}^{ref} = \frac{\dot{\theta}_4^{ref}(t)}{n_4} \begin{bmatrix} \mathbf{n} \\ \mathbf{0} \end{bmatrix} \quad (4.17)$$

$$\dot{\theta}_4^{ref}(t) = \dot{\theta}_4^{des}(t) + k\Delta\theta_4(t) \quad (4.18)$$

where n_4 is the forth element of \mathbf{n} , $\theta_4(t)^{des}$ is the desired trajectory of joint 4; $\Delta\theta_4(t) = \theta_4^{des}(t) - \theta_4$ is the tracking error. k is a feedback gain. The two folded configurations are distinct and uniquely defined as resultant configurations along the respective reactionless motion, wherein $\theta_4 = -\pi$ rad. In Phase I and III, the motions were executed in 5 s, and Phase II in 20 s.

For the comparison, the same positioning task was executed under the joint space interpolation with straight line (JS-C), the inverse Jacobian controller (IJ-C) and the transposed Jacobian controller (TJ-C). For the task space controllers (IJ and TJ-C), the final condition was set to the final position of the end-effector in the 3-Phase method as $[-1.7 \ 0.45 \ 1.7]^T$ m. The three controllers were executed in 30 s. Note that orientation of the end-effector is not considered for the sake of simplicity. Hence, only the positioning subchain was driven.

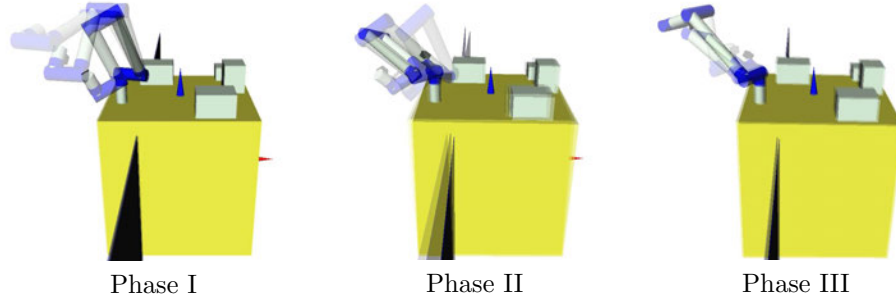


Fig. 4.11: The snapshot of the motion obtained via the 3-phase method.

Table 4.2: The maximum value of the base deviation.

	Maximum deviation [deg]	Ratio
3-Phase	1.95	1.00
JS-C	3.61	1.84
IJ-C	3.21	1.64
TJ-C	3.85	1.96

First, we show the results obtained in the 3-Phase method in Fig. 4.10. From the results, the joint motion can be smoothly obtained and only Phase II introduced the coupling angular momentum.

To evaluate the performance in terms of the base reaction, we compare the base attitude deviations under all methods. The time profiles of the base attitude deviation are displayed in Tab. 4.2. The maximum deviation and the its ratio between the compared methods and the 3-phase are shown in Tab. 4.2.

From the results, it can be seen that the maximum deviation under the 3-phase method is about two times smaller than that under the others. Hence, we can conclude that the 3-phase method has a advantage in terms of the base reaction.

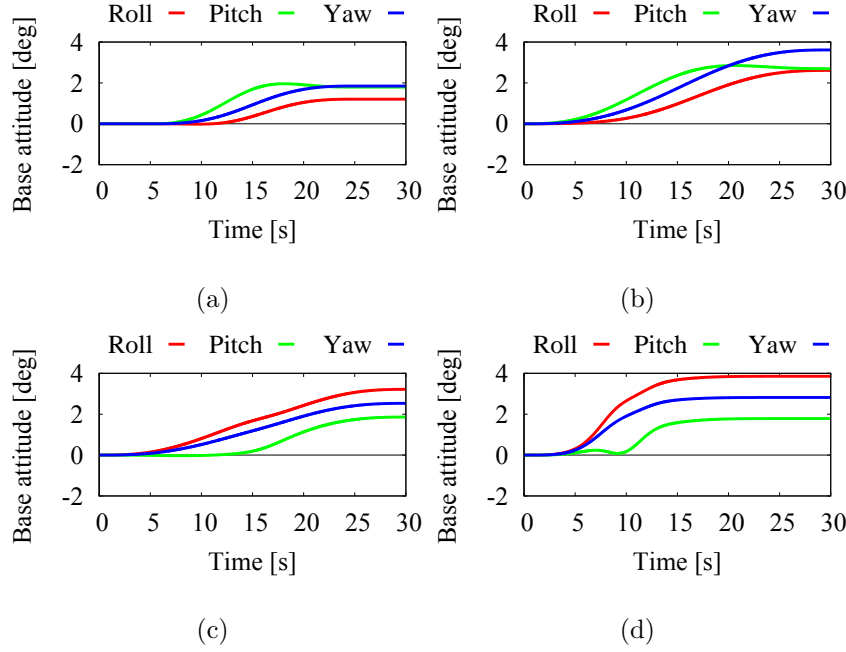


Fig. 4.12: The base attitude deviations under the all methods: (a) 3-phase method, (b) JS-C, (c) IJ-C and (d) TJ-C.

4.5 Deployment task

Finally, we discuss the possibility of reactionless motion control under the deployment motion task from a stowed configurations. When launching a free-floating space robot into orbit, the manipulator has to be stowed to overcome several loads. These configurations are referred to as the *stowed configurations*. An example is displayed in Fig. 4.13 (upper left). During on-orbit experiments, deployment from the configuration has to be executed at least few times. We propose reactionless motion control in the following two case: (i) full reactionless deployment and (ii) partial reactionless deployment.

4.5.1 Full reactionless task

First, we examine the possibility of a deployment task under fully reactionless condition. For the sake of simplicity, we only use the positioning subchain because the effect of wrist motion is relatively small at this motion task. As a result, the DoF of reactionless motion becomes one due to considering only the positioning subchain. Therefore, the reactionless motion path is uniquely determined according to a initial configuration. The final (deployed) configuration can be selected as any configurations along the reactionless path. The selection will depend upon the subsequent task. The benefit is that the speed/acceleration along the reactionless path connecting the two configurations can be set freely that allows for a very time-efficient deployment.

We define the candidates for the stowed configuration of the our manipulator model as follows:

$$\begin{aligned} \boldsymbol{\theta}_{st} = \{ \boldsymbol{\theta} \in \mathbb{R}^7 | \theta_i = \pm\pi/2, \theta_j = 0, \pm\pi, \forall \theta_k \} \\ (i = 1, 2, j = 3 \text{ to } 5, k = 6, 7) \end{aligned} \quad (4.19)$$

Among them, we pick up a configuration that is well-conditioned for the reactionless motion: $[\pi/2 \ -\pi/2 \ 0 \ -\pi \ \pi \ \pi \ 0]^T$ rad. Snapshots of the deployment sequence during 30 s are shown in Fig. 4.13. The motion was obtained via (4.18) with the constant speed of joint 4: $\dot{\theta}_4^{des} = 0.183$ rad/s. It can be seen that the reactionless path is passing through an appropriate point for an inspection task at $t = 30$ s. In that case, this motion task can be useful. The possibility of the reactionless deployment was confirmed at least this case.

However, it should be noted that this motion task is only available when a useful reactionless motion path can be prepared for specific tasks. Instead of the full-reactionless motion, we propose a deployment method using reactionless motion partially based on the 3-phase method in what follows.

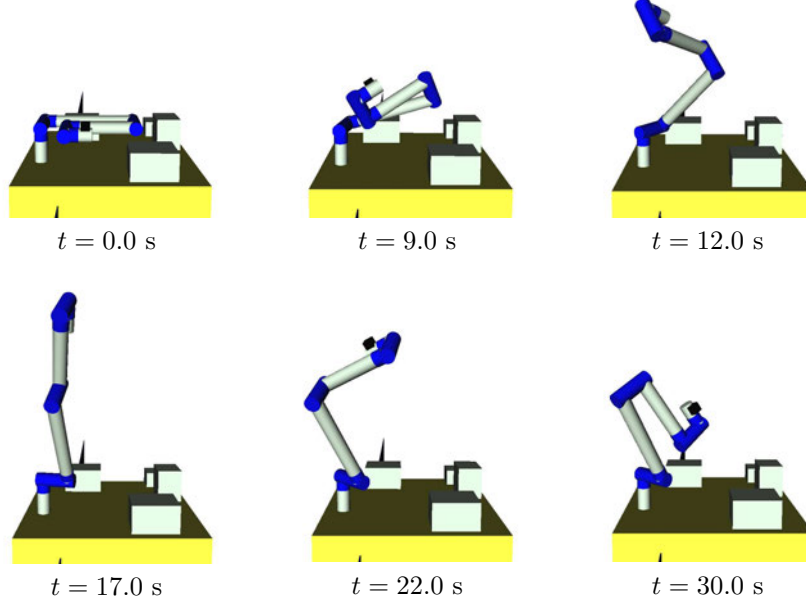


Fig. 4.13: Motion snapshots from the deployment task under reactionless motion control.

Partial reactionless deployment

Here, we present a deployment motion task for reduction of the base reaction. We use a specific part of the 3-phase method; in particular Phase II and III. Because the stowed configuration is a folded configuration, the sub-part of the 3-phase method can be used, straightforwardly. From the results of the 3-phase method, the base reaction can be reduced.

We show an example of the motion task. The pre-positioning task for an inspection task, which was shown in Fig. 4.3 (b), is assumed. The initial configuration is set to the same stowed configuration that was used before. The final configuration is set to $[90 \ 50 \ 0 \ -300 \ 0 \ 20 \ 0]^T$ deg. The middle point configuration at which the two motions are switched is obtained as the terminal configuration from the final one to the elbow folded configuration

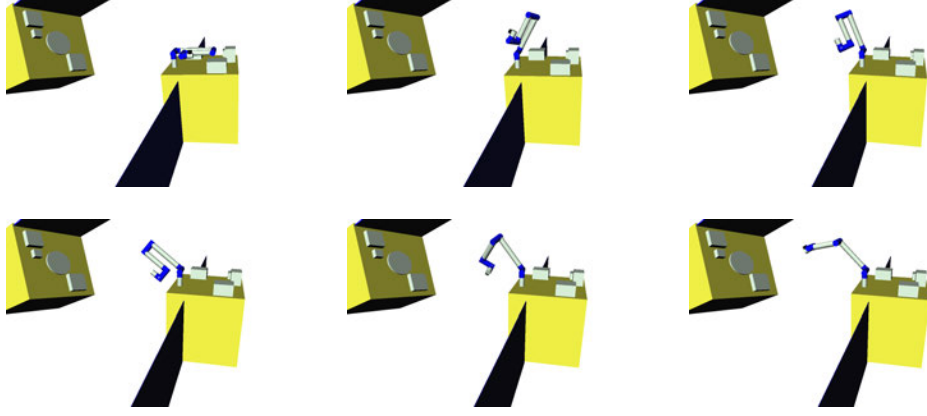


Fig. 4.14: The snapshot of the motion under partial reactionless deployment.

$\theta_4 = \pi$ rad.

The snapshot of the motion task is displayed in Fig. 4.14. For comparison, the joint space controller with straight line trajectory was performed under the same condition. The snapshot is displayed in Fig. 4.15. From the results, the maximum base attitude deviation under partial reactionless task was 5.48 deg; on the other hand, 7.66 deg base attitude was observed under the comparison controller. Hence, 28.5% reduction of the base attitude deviation can be realized.

4.6 Summary

In this chapter, we discussed the motion tasks that are suitable for execution under reactionless motion control. The following three tasks were considered: (i) inspection task using a hand-held camera, (ii) PTP positioning task and (iii) deployment task from the stowed configuration. We showed that the proposed methods using reactionless motion control has a advantages compared with several conventional controllers in terms of the base reaction.

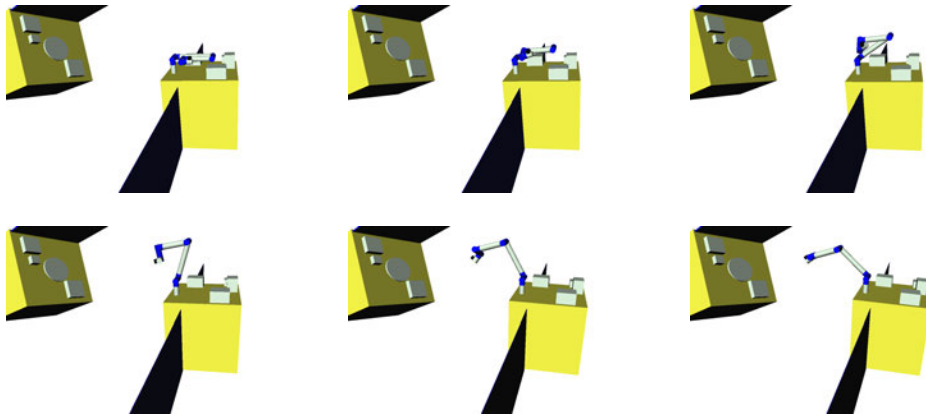


Fig. 4.15: The snapshot of the motion under the conventional joint space interpolation.

Chapter 5

Energy Consumption Analysis

So far, reaction wheels have been used to stabilize the base attitude against the base reaction induced by a manipulator motion. However, as explained in Chapter 1, the output torque of reaction wheels are far smaller than the base reaction. In addition to this problem, it is known that reaction wheels need a large amount of energy if a large output torque is produced [25]. On the other hand, reactionless motion control need not use reaction wheels. Hence, we can expect that energy consumption during a task can be reduced through reactionless motion control. In fact, we will show that reactionless motion coincides with the instantaneous minimum energy motion.

5.1 Kinetic energy

In this work, we assume that kinetic energy is used to evaluate energy consumption. For the sake of simplicity, we ignore energy losses arising from friction, heat and the electric parts. The kinetic energy of the space robot system can be written as [4, 18]:

$$T = \frac{1}{2} \boldsymbol{\omega}_b^T \tilde{\mathbf{M}}_\omega \boldsymbol{\omega}_b + \boldsymbol{\omega}_b^T \begin{bmatrix} \tilde{\mathbf{M}}_{\omega m} & \tilde{\mathbf{M}}_{\omega r} \end{bmatrix} \begin{bmatrix} \dot{\boldsymbol{\theta}} \\ \dot{\boldsymbol{\phi}} \end{bmatrix} + \frac{1}{2} \begin{bmatrix} \dot{\boldsymbol{\theta}}^T & \dot{\boldsymbol{\phi}}^T \end{bmatrix} \begin{bmatrix} \tilde{\mathbf{M}}_m & \mathbf{0} \\ \mathbf{0} & \tilde{\mathbf{M}}_r \end{bmatrix} \begin{bmatrix} \dot{\boldsymbol{\theta}} \\ \dot{\boldsymbol{\phi}} \end{bmatrix} \quad (5.1)$$

where the first term on the r.h.s. represents the partial kinetic energy stemming from base rotation, the second term is the coupling kinetic energy between the base and the manipulator or the reaction wheels. Finally, the third term is the partial kinetic energy produced by the manipulator and the reaction wheels.

With the assumption $\boldsymbol{\omega}_b \approx \mathbf{0}$, (5.1) simplifies as:

$$T = \frac{1}{2} \dot{\boldsymbol{\theta}}^T \tilde{\mathbf{M}}_m \dot{\boldsymbol{\theta}} + \frac{1}{2} \dot{\boldsymbol{\phi}}^T \tilde{\mathbf{M}}_r \dot{\boldsymbol{\phi}}. \quad (5.2)$$

Further on, from angular momentum conservation, the reaction wheel speed can be represented as a function of the joint velocity, $\dot{\boldsymbol{\phi}} = -\tilde{\mathbf{M}}_{\omega r}^{-1} \tilde{\mathbf{M}}_{\omega m} \dot{\boldsymbol{\theta}}$. Substitute this expression into (5.2) to obtain the kinetic energy as a function of the joint velocity:

$$\begin{aligned} T &= \frac{1}{2} \dot{\boldsymbol{\theta}}^T \left(\tilde{\mathbf{M}}_m + \tilde{\mathbf{M}}_{\omega m}^T (\tilde{\mathbf{M}}_{\omega r} \tilde{\mathbf{M}}_r^{-1} \tilde{\mathbf{M}}_{\omega r}^T)^{-1} \tilde{\mathbf{M}}_{\omega m} \right) \dot{\boldsymbol{\theta}} \\ &= \frac{1}{2} \dot{\boldsymbol{\theta}}^T \left(\tilde{\mathbf{M}}_m + I_r^{-1} \tilde{\mathbf{M}}_{\omega m}^T \tilde{\mathbf{M}}_{\omega m} \right) \dot{\boldsymbol{\theta}} \\ &= \frac{1}{2} \dot{\boldsymbol{\theta}}^T \boldsymbol{\Lambda} \dot{\boldsymbol{\theta}} \end{aligned} \quad (5.3)$$

where $\boldsymbol{\Lambda} = \boldsymbol{\Lambda}_m + \boldsymbol{\Lambda}_r$ is the inertia matrix of the manipulator under zero attitude deviation. Matrices $\boldsymbol{\Lambda}_m = \tilde{\mathbf{M}}_m$ and $\boldsymbol{\Lambda}_r = I_r^{-1} \tilde{\mathbf{M}}_{\omega m}^T \tilde{\mathbf{M}}_{\omega m} \in \mathbb{R}^{n \times n}$ are inertias associated with the manipulator and the reaction wheels, respectively. In the above derivation, we assume that $\tilde{\mathbf{M}}_{\omega r} \approx \tilde{\mathbf{M}}_r$. Also it is assumed that the reaction wheels are located on mutually orthogonal axes for zero-momentum stabilization and that $\tilde{\mathbf{M}}_r = \text{diag}(I_r, I_r, I_r)$.

Further on, the direction of instantaneous minimum energy motion can be obtained through SVD of matrix $\boldsymbol{\Lambda}$ [57]:

$$\boldsymbol{\Lambda} = \sigma_1 \mathbf{u}_1 \mathbf{v}_1^T + \sigma_2 \mathbf{u}_2 \mathbf{v}_2^T + \cdots + \sigma_n \mathbf{u}_n \mathbf{v}_n^T \quad (5.4)$$

where σ_i ($\sigma_1 \geq \sigma_2 \geq \cdots \geq \sigma_n$) are the singular values. The meaning of the right singular vectors, \mathbf{v}_i , can be interpreted as normalized joint velocity,

while that of singular value σ_i as kinetic energy induced by joint motion \mathbf{v}_i . Then, σ_n represents the instantaneous minimum kinetic energy, while \mathbf{v}_n^T determines the minimum energy motion direction.

5.2 Motion equivalence

Here, we compare reactionless motion and the instantaneous minimum energy motion via numerical analysis. For the sake of simplicity, we focus on models comprising only one-DoF reactionless motion.

Two-DoF planar manipulator

First, a two-DoF planar model is considered, as shown in Fig. 3.1. The link lengths, masses and inertia moments are set to $l_i = 1.0$ m, $m_i = 100$ kg and $I_i = 8.3$ kgm² ($i = 1, 2$), respectively. The reaction wheel's mass and inertia moment are set to $m_r = 10$ kg, $I_r = 0.11$ kgm². The manipulator attachment position is defined as $r = 0.945$ m and $\psi = 0$ rad.

The following cost function will be used to evaluate the energy relation for reactionless motion and instantaneous minimum energy motion:

$$C_{ratio} = \frac{T_{RNS}}{T_{min}}. \quad (5.5)$$

T_{RNS} and T_{min} denote the kinetic energies under reactionless and instantaneous minimum energy motion, respectively. Because $T_{RNS} \geq T_{min}$ at all configurations, $C_{ratio} \geq 1$ is ensured. This function will be calculated at a mesh of 10K points in joint space, with $-\pi \leq \theta_i \leq \pi$, ($i = 1, 2$). For each coordinate, the joint angles are discretized with $\Delta\theta_i = 6.28 \times 10^{-2}$ rad.

According to (5.4), $\dot{\boldsymbol{\theta}}_{min}$ can be obtained as \mathbf{v}_2 and reactionless motion is obtained through SVD of the coupling inertia matrix. The distribution of C_{ratio} is displayed in Fig. 5.1. From the result, we can confirm that $C_{ratio} \approx 1$ at almost all points. Indeed, the average of C_{ratio} is 1.002 among all points.

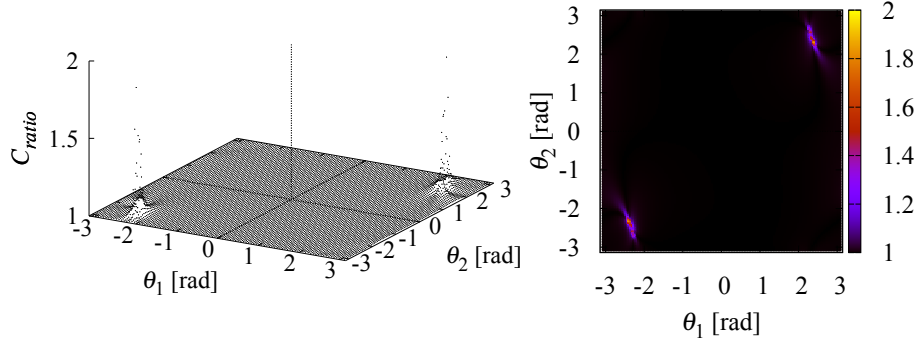


Fig. 5.1: The distribution of the cost function with the two-DoF model.

Hence, these motions are equivalent with this model. Here, we should note that there are large errors at specific points. This non-correspondence will be discussed below.

The role of parameter variation

Before examining the energy ratio with a spatial model, we should identify the influence arising from parameter variation. Here, we focus on variations of the mass and the CoM position of each link according to the following equations:

$$m_i^* = \alpha m_i \quad (5.6)$$

$$l_{ci}^* = \beta l_{ci} \quad (5.7)$$

where $0.5 \leq \alpha \leq 1.5$, $0.5 \leq \beta \leq 1.5$ are the variation factors and $l_{ci} = l_i/2$ denotes the CoM position of each link. The average of C_{ratio} under such variations is displayed in Fig. 5.2. This figure shows that reactionless motion approximately coincides with instantaneous minimum motion even if the parameters are varied. In particular, high equivalence can be observed when α takes large values.

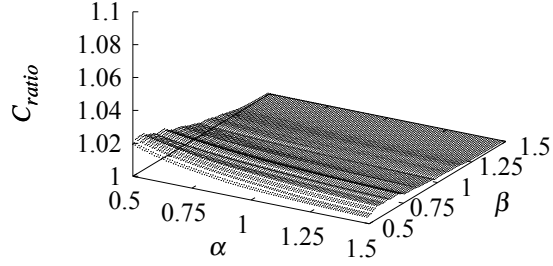


Fig. 5.2: This figure shows how the average of C_{ratio} is affected by parameter variation.

Four-DoF spatial manipulator

The positioning subchain of the seven-DoF redundant manipulator introduced in Section 4.1 will be used to evaluate the energy ratio. The reaction wheel parameters are the same as in the planar case. The same cost function is also used to evaluate the equivalence. The calculation range is as follows:

$$\begin{aligned}
 -\pi &\leq \theta_i \leq \pi \\
 \Delta\theta_i &= 0.125 \text{ rad } (i = 1, 3, 4)
 \end{aligned}
 \tag{5.8}$$

$$\begin{aligned}
 -\frac{\pi}{2} &\leq \theta_2 \leq \frac{\pi}{2} \\
 \Delta\theta_2 &= 0.0628 \text{ rad}
 \end{aligned}
 \tag{5.9}$$

where we restrict the range of Joint 2 because almost all configurations outside the above range have no meaning due to the collision with the satellite. The cost function is calculated at 6.25×10^6 points.

Because of the number of parameters is large, we show the distribution of C_{ratio} parametrized for Joint 1 and 2. First, in Fig. 5.3 (a) a distribution map is shown that does not include large errors. The map was obtained with the parametrization $(\theta_1, \theta_2) = (-3.05, 0.403)$ rad. Except few configu-

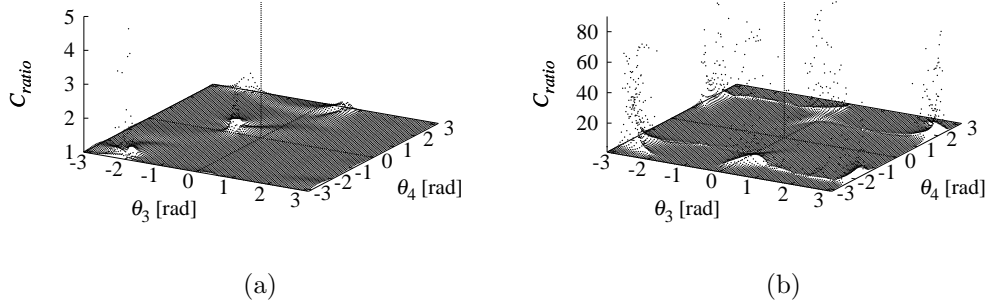


Fig. 5.3: The disutribution of cost function with the four-DoF spatial manipulator model: (a) regularly appearing distribution $(\theta_1, \theta_2) = (-3.05, 0.403)$ rad and (b) near the singularity $(\theta_1, \theta_2) = (-\pi, 0)$ rad.

rations, reactionless motion coincides with the energy minimum motion, as in the planar case. However, we observe some inconsistency at specific configurations. An example is shown in Fig. 5.3 (b) with the parametrization $(\theta_1, \theta_2) = (-\pi, 0)$ rad. Despite these large errors, the average value of C_{ratio} is 1.14. Hence, it can be concluded that reactionless motion produces approximately minimum energy motion. In what follows, we discuss the reasoning behind this observation and the cases of inconsistency.

Discussion

To reason about the equivalence, we should identify a property of kinetic energy produced by both manipulator and reaction wheels under zero base-attitude deviation. This property appears in the inertia matrix. $\mathbf{\Lambda}_m$ and $\mathbf{\Lambda}_r$

are rewritten in the following form:

$$\Lambda_m = \sum_{i=1}^n \left\{ m_i \mathbf{J}_{vi}^T \mathbf{J}_{vi} + \mathbf{J}_{\omega i}^T \mathbf{I}_i \mathbf{J}_{\omega i} \right\} \quad (5.10)$$

$$\begin{aligned} \Lambda_r = \frac{1}{I_r} \sum_{i=1}^n \left\{ m_i^2 \mathbf{J}_{vi}^T [\mathbf{r}_{b \rightarrow i}^\times]^T [\mathbf{r}_{b \rightarrow i}^\times] \mathbf{J}_{vi} + \mathbf{J}_{\omega i}^T \mathbf{I}_i \mathbf{J}_{\omega i} + \right. \\ \left. m_i \mathbf{J}_{\omega i}^T \mathbf{I}_i [\mathbf{r}_{b \rightarrow i}^\times] \mathbf{J}_{vi} + [m_i \mathbf{J}_{\omega i}^T \mathbf{I}_i [\mathbf{r}_{b \rightarrow i}^\times] \mathbf{J}_{vi}]^T \right\} \quad (5.11) \end{aligned}$$

where $m_i, \mathbf{I}_i \in \mathbb{R}^3$ are i -th link mass and inertia tensor, $\mathbf{J}_{vi}, \mathbf{J}_{\omega i} \in \mathbb{R}^{3 \times n}$ stand for the Jacobian w.r.t. linear and angular velocity of each link, $\mathbf{r}_{b \rightarrow i} \in \mathbb{R}^3$ is the position vector of the i -th link CoM w.r.t. the base CoM. Here, we assume a general n -link manipulator model. Note that terms related to base translation are ignored for the sake of simplicity.

From (5.10), it can be seen that the kinetic energy induced by the manipulator motion is represented as a linear function in terms of the inertia parameters of manipulator. On the other hand, the reaction wheel related energy is a quadratic function of the same parameters; it is also in proportion to the inverse of the inertia moment of the reaction wheel, which is usually much smaller than 1. Hence, we can conclude that the kinetic energy produced by the reaction wheels is much larger than that by the manipulator. This feature would make reactionless motion potentially effective in terms of energy consumption because the usage of reaction wheels can be avoided.

On the other hand, comparing the results in Fig. 3.2 (b) and Fig. 5.1, we can find that there is some inconsistency around the singularities of the coupling inertia matrix. In particular, at such a singularity, any motion would not disturb the base attitude because the dimension of the null-space of the coupling inertia matrix increases. A second reactionless motion vector appears then at the singularity and both null-space vectors span the tangent space of joint space $T_\theta(\mathbb{R}^2)$. This means that reactionless motion must be at the energy minimum. On the other hand, near a singularity, reactionless

motion deviates from the instantaneous energy minimum motion. At these configurations, because the base disturbance is minute, a large effort of the reaction wheels is hardly needed. Namely, the kinetic energy stemming from the reaction wheels becomes small, and hence a manipulator motion whose kinetic energy is minimum or at least smaller than that reactionless motion induces can be closer to the minimum energy motion than reactionless motion be.

5.2.1 Comparative study for the inspection task

Simulation condition

We evaluate the performance of reactionless motion control in terms of energy consumption during the inspection maneuver. From the above analysis it became apparent that reactionless motion produces nearly minimum energy motion and that the use of reaction wheels would be inefficient from the viewpoint of energy consumption, when compensating base disturbance.

We consider the following cost functions to evaluate the performance:

$$C_{max} = \frac{1}{2} \max_{t_0 \leq t \leq t_f} \left(\dot{\boldsymbol{\theta}}^T(t) \boldsymbol{\Lambda} \dot{\boldsymbol{\theta}}(t) \right) \quad (5.12)$$

$$C_{sum} = \frac{1}{2} \int_{t_0}^{t_f} \dot{\boldsymbol{\theta}}^T(t) \boldsymbol{\Lambda} \dot{\boldsymbol{\theta}}(t) dt. \quad (5.13)$$

In order to realize zero base-attitude deviation with the reaction wheels, the reaction wheel torque should be:

$$\boldsymbol{\tau}_r^{ref} = -\frac{d}{dt}(\tilde{\mathbf{M}}_{\omega m} \dot{\boldsymbol{\theta}}^{ref}(t)) \quad (5.14)$$

where $\dot{\boldsymbol{\theta}}^{ref}$ is the pre-defined reference control command for the manipulator. We compare the above costs under the camera inspection task under five conditions with different initial configurations and desired motions. In all cases, the simulation time is set at 20 s and the comparison controller is the inverse Jacobian controller using only the wrist assembly, as explained in the previous section.

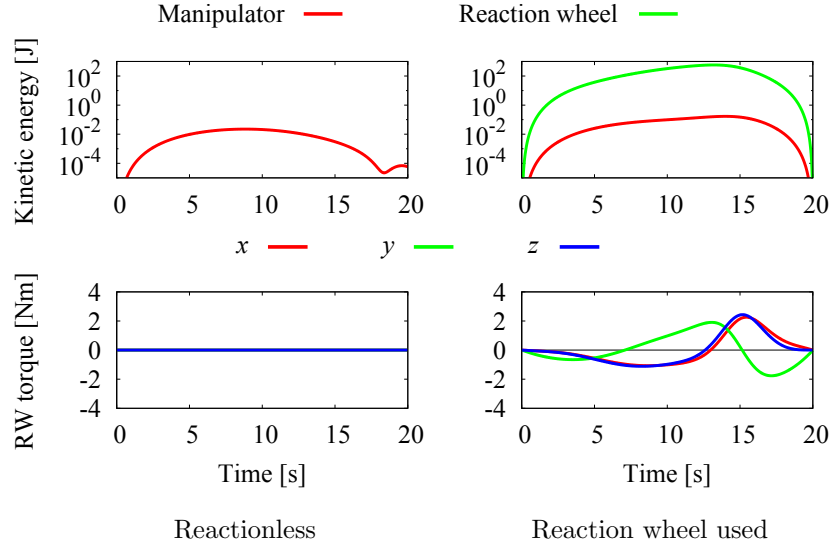


Fig. 5.4: An example of energy consumption comparison.

5.2.2 Simulation results

First, as an example, consider the conditions used in Section 4.2 (the case of Fig. 4.3 (a)): the initial configuration is set to $[-90 \ -30 \ 0 \ -70 \ 180 \ -30 \ 0]^T$ deg, the reference angular velocity is $\omega_e^{ref} = \pi[s(t) \ 0 \ 0]^T$, where $0 \leq s(t) \leq 1$ denotes a fifth-order spline function; the simulation time and the gain are set at 20 s and $k_g = 100$ kg/(m · s), respectively. The results are displayed in Fig. 5.4. We can see that the kinetic energy produced by the reaction wheels is quite larger than that by the manipulator motion. Hence, in this case, we can confirm that reactionless motion control has an advantage in terms of energy consumption, as described above. In addition, if we plan to perform this inspection task with reaction wheels, the manipulator has to be driven at lower speed because the limitation of the reaction wheel torque is in general quite low. For instance, in the ETS-VII experiment it was 0.1 Nm.

Next we compare the cost for five different initial configurations and desired motions chosen randomly. The results are displayed in Fig. 5.5. The red

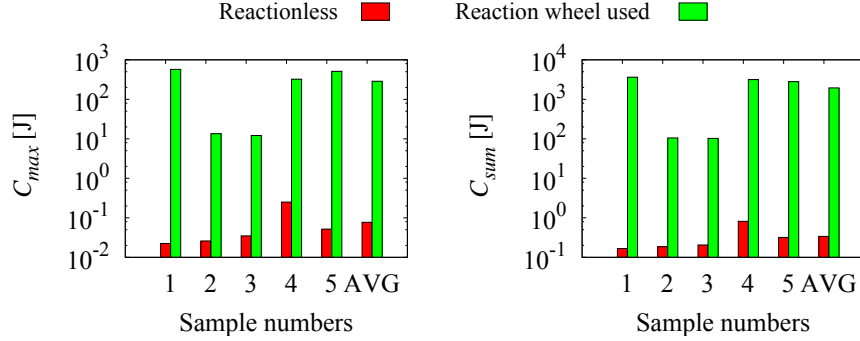


Fig. 5.5: Comparison of energy consumption under five conditions

bar expresses the results under reactionless motion control; the green bar shows the results when reaction wheels are used. Note that vertical axis represents the cost in logarithmic scale. From the results it can be seen that energy consumption under reactionless motion is quite smaller than that with reaction wheels. Actually, almost 10^3 times reduction is observed in each cost function. This result stems from the large energy consumption of the reaction wheels, as explained in (5.11). In summary, we can conclude that under reactionless motion control it is possible to reduce both, energy consumption as well as the duration of the mission.

5.3 Summary

In this chapter, we discussed the energy consumption under zero attitude deviation. We formulated the kinetic energy of a free-floating space robot in terms of joint velocity under zero attitude deviation. From the result, we confirmed that the kinetic energy stemming from the reaction wheels is represented as a quadratic function of the inertia parameters of the manipulator and position vector positioning to the each line CoM, while the kinetic energy of the manipulator is a linear function of the both quantities. Hence, the energy consumption of the reaction wheels must be much larger than that

of the manipulator. This feature makes reactionless motion control effectiveness in terms of energy consumption. In fact, through numerical verification, we showed that reactionless motion coincides with the instantaneous minimum energy motion. We compared the energy consumption of reactionless motion control with that of using reaction wheels during some inspection tasks that was proposed in Chapter 4. We obtained an interesting result that the kinetic energy during reactionless motions task is 10^3 times smaller than that during reaction wheel used task, on average. In summary, we can conclude that reactionless motion control has an advantage with respect to energy efficiency.

Part II

Motion/Force Control

Chapter 6

Formulation and Modeling

In this chapter, we describe motion/force control of redundant manipulators. First, we explain the Operational Space (OS) formulation that has been traditionally used for motion/force control and also impedance control by various researchers. Then, we describe a new control scheme based on the Reaction Null-Space formulation. Finally, we show the performance of the proposed method with two examples.

6.1 Formulations

6.1.1 OS formulation based control

From a historical point of view, we, firstly, explain the OS formulation based motion/force control in what follows.

Equation of motion in end-effector coordinates

Let us consider a serial n -link fixed base redundant manipulator as shown in the right part of Fig. 6.1. The model has n -active joints and n -rigid body links. We assume that the system has redundant DoF(s), i.e. $n > 6$. According to the OS formulation [29], the dynamics of a serial-link manipulator in

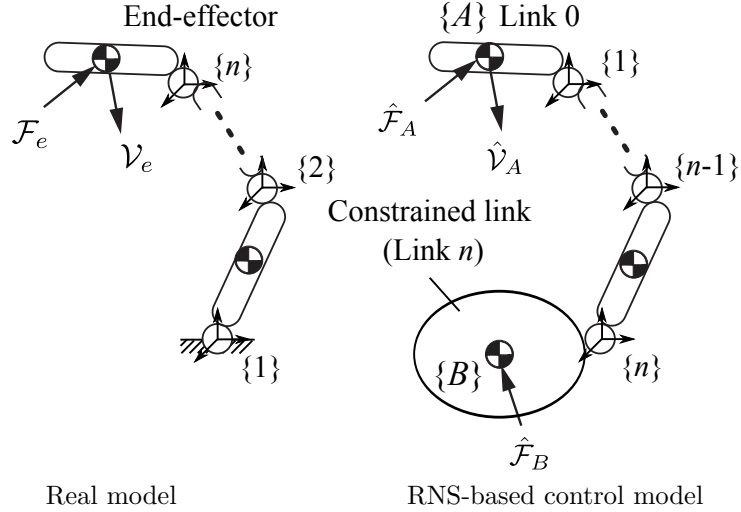


Fig. 6.1: Model of n -link manipulator model and its $n+1$ link control model for the RNS-based controller.

end-effector coordinates are described in the following form:

$$\mathbf{M}_e \dot{\mathcal{V}}_e + \mathcal{C}_e + \mathcal{G}_g = \mathcal{F}_e + \mathcal{F}_\kappa \quad (6.1)$$

where $\mathcal{V}_e \in \mathbb{R}^6$ is spatial velocity of the end-effector, $\mathbf{M}_e \in \mathbb{R}^{6 \times 6}$ defines the operational space inertia matrix and also is referred to as the inversion of *Mobility Tensor*, \mathcal{C}_e , $\mathcal{G}_g \in \mathbb{R}^6$ stand for Coriolis and centrifugal force and gravity force, respectively. \mathcal{F}_e , \mathcal{F}_κ is control command with dimensions of force, and the contact force imposed on the end-effector from environments.

On the other hand, because the end-effector variables cannot become generalized coordinates of redundant manipulators, the above equation of motion cannot be obtained directly. Hence, a transformation is needed from the equation of motion in joint-space.

The equation of motion in joint space is described as follows:

$$\mathbf{M}_l \ddot{\boldsymbol{\theta}} + \mathbf{c}_l + \mathbf{g}_l = \boldsymbol{\tau} + \mathbf{J}_e^T \mathcal{F}_\kappa \quad (6.2)$$

where $\boldsymbol{\theta} \in \mathbb{R}^n$ stands for the joint coordinate vector, $\mathbf{M}_l \in \mathbb{R}^{n \times n}$ is the joint-

space inertia matrix, \mathbf{c}_l , \mathbf{g}_l denote Coriolis and centrifugal force and gravity force vectors in joint-space, respectively. $\boldsymbol{\tau} \in \mathbb{R}^n$ is joint torque vector, $\mathbf{J}_e \in \mathbb{R}^{6 \times n}$ is the Jacobian associated with the end-effector

Through the Jacobian, the end-effector velocity/acceleration are expressed in terms of the joint variables as follows:

$$\mathbf{v}_e = \mathbf{J}_e \dot{\boldsymbol{\theta}} \quad (6.3)$$

$$\dot{\mathbf{v}}_e = \mathbf{J}_e \ddot{\boldsymbol{\theta}} + \dot{\mathbf{J}}_e \dot{\boldsymbol{\theta}}. \quad (6.4)$$

On the other hand, from the result of statics, end-effector force can be related to joint torque:

$$\boldsymbol{\tau} = \mathbf{J}_e^T \mathcal{F}_e \quad (6.5)$$

From (6.2) to (6.5), we can obtain the following definitions of the inertia matrix and non-linear and gravity force vector in end-effector coordinates:

$$\mathbf{M}_e = (\mathbf{J}_e \mathbf{M}_l^{-1} \mathbf{J}_e^T)^{-1} \quad (6.6)$$

$$\mathcal{C}_e = [\mathbf{J}_e^{M+}]^T \mathbf{c}_l - \mathbf{M}_e \dot{\mathbf{J}}_e \dot{\boldsymbol{\theta}} \quad (6.7)$$

$$\mathcal{G}_e = [\mathbf{J}_e^{M+}]^T \mathbf{g}_l \quad (6.8)$$

where $\mathbf{J}_e^{M+} = \mathbf{M}_l^{-1} \mathbf{J}_e^T \mathbf{M}_e$ is the inertia weighted generalized inverse of the Jacobian.

Control command

Consider now a motion/force control scenario wherein the end effector is partially constrained by the environment. The end-effector dynamics become

$$\mathcal{F}_e - \mathbf{M}_e \dot{\mathbf{v}}_e - \mathcal{C}_e - \mathcal{G}_e = \mathcal{F}_\kappa \quad (6.9)$$

To meet the control objective, a reference end-effector force is designed as

$$\mathcal{F}_e^{ref} = \mathcal{F}_m^{ref} + \mathcal{F}_\kappa^{ref} \quad (6.10)$$

$$\mathcal{F}_m^{ref} = \mathbf{M}_e \mathbf{S} \dot{\mathbf{v}}_e^{ref} + \mathcal{C}_e + \mathcal{G}_e \quad (6.11)$$

$$\mathcal{F}_\kappa^{ref} = \mathbf{S}_\perp \mathcal{F}_c^{ref} \quad (6.12)$$

where \mathcal{F}_m^{ref} and \mathcal{F}_κ^{ref} are two components referring to end-effector motion and contact force, respectively. $\mathbf{S} \in \mathbb{R}^{6 \times 6}$ is a selection matrix suitably defined to specify the unconstrained motion direction, while $\mathbf{S}_\perp \in \mathbb{R}^{6 \times 6}$ is its complement. $\dot{\mathcal{V}}_e^{ref}$ and \mathcal{F}_c^{ref} are reference value for the motion and force tasks, respectively, that usually involve feedback control terms.

Further on, since the manipulator is redundant, there is an infinite set of control joint torques that could be applied without affecting the resultant forces at the end-effector [29].

$$\boldsymbol{\tau} = \mathbf{J}_e^T \mathcal{F}_e^{ref} + (\mathbf{E} - \mathbf{J}_e^T \mathbf{J}_e^{M+}) \boldsymbol{\tau}_a \quad (6.13)$$

where $(\mathbf{E} - \mathbf{J}_e^T \mathbf{J}_e^{M+})$ denotes a projector onto the null-space of the transposed inertia-weighted generalized inverse of the Jacobian, \mathbf{E} standing for the $n \times n$ identity matrix. $\boldsymbol{\tau}_a$, an arbitrary joint torque vector, parametrizes (in a non-minimal way) the set of joint torques that do not impose any end-effector force. Moreover, there is also another infinite set of control joint torques that produce the same end-effector acceleration as a given end-effector force:

$$\boldsymbol{\tau} = \mathbf{M}_l \mathbf{J}^\# \mathbf{M}_e^{-1} \mathcal{F}_e^{ref} + \mathbf{M}_l (\mathbf{E} - \mathbf{J}_e^\# \mathbf{J}_e) \ddot{\boldsymbol{\theta}}_a \quad (6.14)$$

where $\ddot{\boldsymbol{\theta}}_a \in \mathbb{R}^n$ stands for an arbitrary joint acceleration vector, $(\circ)^\#$ denotes generalized inverse of the corresponding matrix. The two joint-torque sets (6.13) and (6.14) are compatible (or dynamically consistent), only when the inertia-weighted generalized inverse of the Jacobian is applied in (6.14). This leads to *complete dynamic decoupling* between the particular components responsible for the motion/force control task and the null-space components.

The property of complete dynamic decoupling plays an important role in motion/force and impedance control design, since task and null-space control components can be designed independently. However, the nominal behavior in joint space determined by the task-space control component may become unstable due to ill-conditioning of the inertia weighted generalized inverse.

Also, the joint velocity may grow in an uncontrollable fashion because of the non-integrability of joint acceleration. Although these problems can be alleviated via the null-space control component, it would be much more desirable to have a controller with a satisfactory nominal behavior.

6.1.2 Reaction Null-Space based control

In what follows, we describe the RNS-based motion/force control for fixed-base redundant manipulators.

End-link dynamics based on free-floating base coordinates

For the RNS based motion/force control, we consider a free-floating base serial-link manipulator with $n+1$ links, as shown in the right part of Fig. 6.1. The two end-links are denoted as A and B . Without loss of generality, in what follows end-link A will be designed as the root link. It is convenient to assume that the root link is connected to the inertial frame via a virtual six-DoF joint. Hence, there are $n+6$ generalized coordinates: the n joint coordinated plus the six coordinates of the root end-link A . There are three points of interest: characteristic points on each of the two end-links (points A and B in Fig. 6.1) and the total center of mass. External spatial forces $\hat{\mathcal{F}}_A$ and $\hat{\mathcal{F}}_B$ act at points A and B , respectively. The motion of the two end-links is characterized by spatial velocities $\hat{\mathcal{V}}_A$ and $\hat{\mathcal{V}}_B$. Note that we distinguish the quantities of RNS based control model from these of the real model through the notation ($\hat{\circ}$).

The system dynamics are described by two coupled equations:

$$\hat{\mathbf{M}}_A \dot{\hat{\mathcal{V}}}_A + \hat{\mathbf{M}}_{Al} \ddot{\hat{\boldsymbol{\theta}}} + \hat{\mathbf{C}}_A + \hat{\mathbf{G}}_A = \hat{\mathcal{F}}_A + \hat{\mathbf{T}} \hat{\mathcal{F}}_B \quad (6.15)$$

$$\hat{\mathbf{M}}_{Al}^T \dot{\hat{\mathcal{V}}}_A + \hat{\mathbf{M}}_l \ddot{\hat{\boldsymbol{\theta}}} + \hat{\mathbf{c}}_l \hat{\mathbf{g}}_l = \hat{\boldsymbol{\tau}} + \hat{\mathbf{J}}_B^T \hat{\mathcal{F}}_B \quad (6.16)$$

First, note that in (6.15) there are two linear force components. $\hat{\mathbf{M}}_{Al} \ddot{\hat{\boldsymbol{\theta}}}$ reflects the inertial coupling between end-link A and the rest of the links. Component

$\hat{\mathbf{M}}_A \dot{\mathcal{V}}_A$, on the other hand, represents the inertia force of the composite rigid body (CRB) obtained when the joints are momentarily locked. The CRB dynamics are characterized by the inertial properties of the entire system; they are represented in terms of end-link A coordinates.

Next, note that (6.16) would represent the dynamics of a “conventional” fixed-base manipulator, where link A is fixed. This manipulator is composed of all bodies except link A ; because end-link A is the root, quantities $\hat{\mathbf{M}}_l$, $\hat{\mathbf{c}}_l$, $\hat{\mathbf{g}}_l$ and $\hat{\mathbf{J}}_B$ are those of the fixed-base manipulator, link B being its end-effector. To adapt this floating-base notation to the fixed-base manipulator described above, we will keep end-link A as the root link, but designate it as the end-effector. End link B , on the other hand, will be fully constrained to become the fixed base. This implies the renumbering of joints and links in reverse order, as illustrated in Fig. 6.1.

Control command

Our goal is to design a controller with a task-space control component that can ensure the desirable nominal behavior in joint space, such that large joint-velocity peaks and velocity build-up can be avoided. The derivation is based on the hybrid motion/force control approach presented in [58]. End-effector A contacts the environment under a motion/force task scenario, being thereby constrained along $k < 6$ directions. This can be expressed via the equation $\hat{\mathbf{J}}_\kappa(\dot{\mathbf{q}})\dot{\mathbf{q}} = \mathbf{0}$, $\hat{\mathbf{J}}_\kappa(\dot{\mathbf{q}}) \in \mathbb{R}^{k \times (6+\kappa)}$ denoting the constraint Jacobian containing partial derivatives related to the environment constraint $\kappa(\dot{\mathbf{q}}) = \text{const}$. End-effector A ’s spatial force is then $\hat{\mathcal{F}}_A = \hat{\mathbf{J}}_{\kappa A}^T \hat{\boldsymbol{\lambda}}$, where $\hat{\boldsymbol{\lambda}} \in \mathbb{R}^k$ is the Lagrange multiplier for the forces of constraint and $\hat{\mathbf{J}}_{\kappa A}(\dot{\mathbf{q}}) \in \mathbb{R}^{k \times 6}$ is a submatrix of the constraint Jacobian s.t. $\hat{\mathbf{J}}_{\kappa A} \hat{\mathcal{V}}_A = \mathbf{0}$. Further on, denote $\hat{\mathcal{V}}_A = \hat{\mathbf{S}}_v \hat{\boldsymbol{\nu}}_A$ where $\hat{\boldsymbol{\nu}}_A$ is end-effector A ’s velocity along the unconstrained directions and $\hat{\mathbf{S}}_v(\dot{\mathbf{q}})$ is defined from $\hat{\mathbf{S}}_f^T \hat{\mathbf{S}}_v = \mathbf{0}$, $\hat{\mathbf{S}}_f = \hat{\mathbf{J}}_{\kappa A}^T(\dot{\mathbf{q}})$.

Using (6.15), we first obtain the reference joint acceleration for the task-

space (particular-solution) control component:

$$\ddot{\boldsymbol{\theta}} = \hat{\mathbf{M}}_{Al}^+(\hat{\mathbf{S}}_f \hat{\mathbf{f}}_\lambda - \hat{\mathbf{M}}_A \hat{\mathbf{S}}_v \hat{\boldsymbol{\alpha}}_v - \hat{\mathbf{M}}_A \dot{\hat{\mathbf{S}}}_v \hat{\boldsymbol{\nu}}) + \hat{\mathbf{M}}_{Al}^+(\hat{\mathbf{T}} \hat{\mathcal{F}}_B - \hat{\mathcal{C}}_B - \hat{\mathcal{G}}_B) \quad (6.17)$$

This control acceleration ensures complete decoupling between the motion and force subtasks for the closed-loop system. The respective joint torque control component derived via (6.16) is

$$\begin{aligned} \hat{\boldsymbol{\tau}}^{ref} = & (\hat{\mathbf{M}}_{Al}^T - \hat{\mathbf{M}}_l \hat{\mathbf{M}}_{Al}^+ \hat{\mathbf{M}}_A) \hat{\mathbf{S}}_v \hat{\boldsymbol{\alpha}}_v + \hat{\mathbf{M}}_l \hat{\mathbf{M}}_{Al}^+ \hat{\mathbf{S}}_f \hat{\mathbf{f}}_\lambda \\ & + (\hat{\mathbf{M}}_l \hat{\mathbf{M}}_{Al}^+ \hat{\mathbf{T}} - \hat{\mathbf{J}}_B^T) \hat{\mathcal{F}}_B \\ & + \hat{\mathbf{c}}_l + \hat{\mathbf{g}}_l - \hat{\mathbf{M}}_l \hat{\mathbf{M}}_{Al}^+ (\hat{\mathcal{C}}_A + \hat{\mathcal{G}}_A + \hat{\mathbf{M}}_A \dot{\hat{\mathbf{S}}}_v \hat{\boldsymbol{\nu}}) \end{aligned} \quad (6.18)$$

This control torque compensates the joint-space non-linear and gravity forces and ensures a double-integrator type closed-loop behavior $\ddot{\boldsymbol{\theta}} = \ddot{\boldsymbol{\theta}}^{ref}$. When compared to the particular-solution control torque derived under the OS formulation, $\boldsymbol{\tau} = \mathbf{J}_e^T \mathcal{F}_e^{ref}$, \mathcal{F}_e^{ref} given in (6.10), the above expression is somewhat messier. But we can expect a better nominal behavior in joint-space, as explained. The following remarks are due. First, note that with the controller we have to compensate the exact non-linear force term $\hat{\mathcal{C}}_A$ instead of compensating its approximation $\hat{\mathcal{C}}_A \approx \dot{\hat{\mathbf{M}}}_A \hat{\mathcal{V}}_A + \hat{\mathbf{M}}_{Al} \dot{\boldsymbol{\theta}}$ that was required for momentum conservation; otherwise, the task-space behavior cannot be guaranteed anymore.

Constraint force

To implement the RNS-based control, a constraint force that makes the link B the fixed base has to be presented. The constraint force is obtained through



method of Lagrange multiplier in what follows.

First, we obtain the kinematic equation of the constrained link velocity as follows:

$$\begin{aligned} \hat{\mathcal{V}}_B &= \hat{\mathbf{T}}^T \hat{\mathcal{V}}_A + \hat{\mathbf{J}}_B \dot{\boldsymbol{\theta}} \\ &= \hat{\mathbf{J}}_{const} \dot{\hat{\mathbf{q}}} \end{aligned} \quad (6.19)$$

where $\hat{\mathbf{J}}_{const} = [\hat{\mathbf{T}} \ \hat{\mathbf{J}}] \in \mathbb{R}^{6 \times (n+6)}$ stands for constraint Jacobian, $\dot{\mathbf{q}} = [\mathcal{V}_A^T \ \dot{\boldsymbol{\theta}}^T]^T$ denotes the generalized velocity vector. Since the condition of fixed base is $\mathcal{V}_B = \mathbf{0}$, the following equation, hence, has to be satisfied:

$$\hat{\mathbf{J}}_{const} \ddot{\mathbf{q}} + \dot{\hat{\mathbf{J}}}_{const} \dot{\mathbf{q}} = \mathbf{0} \quad (6.20)$$

On the other hand, the equation of motion of the control model can be expressed in the following compact form:

$$\hat{\mathbf{M}} \ddot{\mathbf{q}} + \hat{\mathbf{c}} + \hat{\mathbf{g}} = \hat{\mathbf{Q}} + \hat{\mathbf{J}}_{const}^T \hat{\mathcal{F}}_B \quad (6.21)$$

Then, substituting (6.21) into (6.20) and solving it for $\hat{\mathcal{F}}_B$, we can obtain the constraint force as follows:

$$\hat{\mathcal{F}}_B = (\hat{\mathbf{J}}_{const} \hat{\mathbf{M}}^{-1} \hat{\mathbf{J}}_{const}^T)^{-1} \left(\hat{\mathbf{J}}_{const} \hat{\mathbf{M}}^{-1} (\hat{\mathbf{c}} + \hat{\mathbf{g}} - \hat{\mathbf{Q}}) - \dot{\hat{\mathbf{J}}}_{const} \dot{\mathbf{q}} \right) \quad (6.22)$$

Finally, the constraint force is substituting into (6.17) and (6.18).

6.2 Examples

6.2.1 Planar three-DoF manipulator

In what follows, we provide two examples to evaluate the performance of the proposed control. First, we consider a planar three-DoF redundant manipulator as shown in Fig. 6.2 (a). We assume that the end-effector contacts with an environment at a point. Contact force acting to the end-effector has only force component; the moment of force component is ignored. And also the end-effector orientation is not considered here. Hence, the system has one degree-of-redundancy.

The control model for the RNS based control is displayed in Fig. 6.2 (b). As shown in the figure, link 3 of the control model is regarded as the constrained

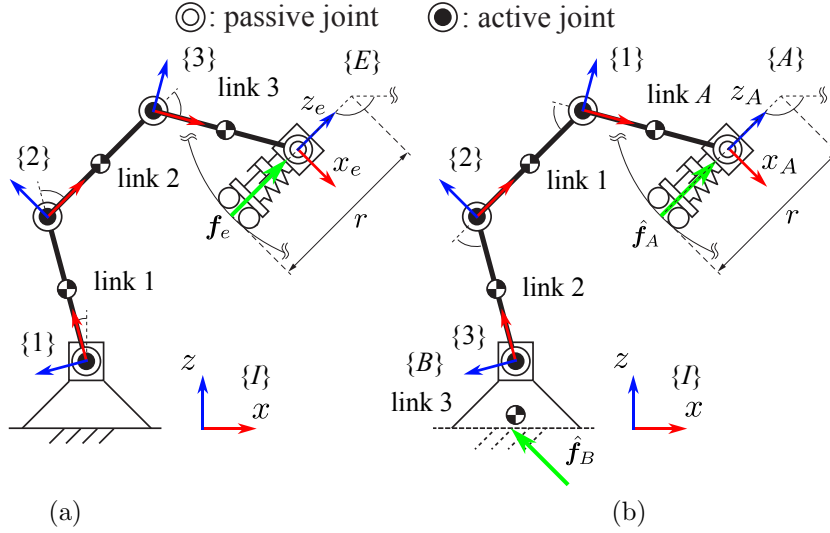


Fig. 6.2: Three-link planar redundant manipulator: (a) real model and (b) control model.

link. The equation of motion of the control model is described as follows:

$$\begin{bmatrix} \hat{M}_v & \hat{M}_{v\omega} & \hat{M}_{vl} \\ \hat{M}_{v\omega}^T & \hat{M}_\omega & \hat{M}_{\omega l} \\ \hat{M}_{vl}^T & \hat{M}_{\omega l}^T & \hat{M}_l \end{bmatrix} \begin{bmatrix} \hat{v}_A \\ \hat{\omega}_A \\ \hat{\theta} \end{bmatrix} + \begin{bmatrix} \hat{c}_{vA} \\ \hat{c}_{\omega A} \\ \hat{c}_l \end{bmatrix} + \begin{bmatrix} \hat{g}_{vA} \\ \hat{g}_{\omega A} \\ \hat{g}_l \end{bmatrix} = \begin{bmatrix} \hat{f}_A \\ 0 \\ \hat{\tau} \end{bmatrix} + \begin{bmatrix} \hat{T} \\ \hat{J}_B \end{bmatrix} \begin{bmatrix} \hat{f}_B \\ \hat{n}_B \end{bmatrix} \quad (6.23)$$

where the dimension of each coordinate are $\hat{v}_A \in \mathbb{R}^2$, $\hat{\omega}_A$ and $\hat{\theta} \in \mathbb{R}^3$. Then, the size of the matrices is determined according to the dimension of the coordinate variables. Because we assume end-effector linear motion only, the equation of motion has to be modified. First, estimated from the middle part of (6.23), the angular acceleration of link A can be obtained as follows:

$$\dot{\hat{\omega}}_A = -\hat{M}_\omega^{-1} (\hat{M}_{v\omega}^T \hat{v}_A + \hat{M}_{\omega l} \ddot{\theta} + \hat{c}_{\omega A} + \hat{g}_{\omega A} - \hat{T}_\omega [\hat{f}_B^T \quad \hat{n}_B]^T) \quad (6.24)$$

where $\hat{T}_\omega \in \mathbb{R}^{1 \times 3}$ is the pose matrix associated with rotation. Then, substituting (6.24) into the upper part of (6.23), we can obtain the following

equation of motion with reduced form:

$$\begin{aligned}
& (\hat{\mathbf{M}}_v - \hat{\mathbf{M}}_{v\omega} \hat{M}_\omega^{-1} \hat{\mathbf{M}}_{v\omega}^T) \ddot{\mathbf{v}}_A + (\hat{\mathbf{M}}_{vl} - \hat{\mathbf{M}}_{v\omega} \hat{M}_\omega^{-1} \hat{\mathbf{M}}_{\omega l}) \ddot{\boldsymbol{\theta}} + \\
& (\hat{\mathbf{c}}_{v_A} - \hat{\mathbf{M}}_{v\omega} \hat{M}_\omega \hat{c}_{\omega_A}) + (\hat{\mathbf{g}}_{v_A} - \hat{\mathbf{M}}_{v\omega} \hat{M}_\omega \hat{g}_{\omega_A}) \\
& = (\hat{\mathbf{T}}_v - \hat{\mathbf{M}}_{v\omega} \hat{M}_\omega^{-1} \hat{\mathbf{T}}_\omega) [\hat{\mathbf{f}}_B^T \quad \hat{n}_B]^T
\end{aligned} \tag{6.25}$$

Then, the reference joint acceleration can be obtained as:

$$\begin{aligned}
\ddot{\boldsymbol{\theta}}^{ref} = & (\hat{\mathbf{M}}_{vl} - \hat{\mathbf{M}}_{v\omega} \hat{M}_\omega^{-1} \hat{\mathbf{M}}_{\omega l}) + \left\{ (\hat{\mathbf{M}}_v - \hat{\mathbf{M}}_{v\omega} \hat{M}_\omega^{-1} \hat{\mathbf{M}}_{v\omega}^T) \ddot{\mathbf{v}}_A^{ref} + \right. \\
& (\hat{\mathbf{c}}_{v_A} - \hat{\mathbf{M}}_{v\omega} \hat{M}_\omega \hat{c}_{\omega_A}) + (\hat{\mathbf{g}}_{v_A} - \hat{\mathbf{M}}_{v\omega} \hat{M}_\omega \hat{g}_{\omega_A}) \\
& \left. - (\hat{\mathbf{T}}_v - \hat{\mathbf{M}}_{v\omega} \hat{M}_\omega^{-1} \hat{\mathbf{T}}_\omega) [\hat{\mathbf{f}}_B^{Tref} \quad \hat{n}_B]^T \right\}
\end{aligned} \tag{6.26}$$

Parameters transformation

Under the RNS-based motion/force controller, we have to consider the relations of model parameters between the two models. End-effector coordinates, joint coordinate and joint torque are transformed according to the following

:

$$[\hat{x}_A \quad \hat{z}_A \quad \hat{\psi}_A]^T = [x_e \quad z_e \quad \psi_e]^T \tag{6.27}$$

$$[\hat{\theta}_1 \quad \hat{\theta}_2 \quad \hat{\theta}_3]^T = -[\theta_3 \quad \theta_2 \quad \theta_1]^T \tag{6.28}$$

$$[\hat{\tau}_1 \quad \hat{\tau}_2 \quad \hat{\tau}_3]^T = -[\tau_3 \quad \tau_2 \quad \tau_1]^T \tag{6.29}$$

In addition, the model parameters, such as link length, mass and inertia moment, are determined as follows:

$$[\hat{l}_A \quad \hat{l}_1 \quad \hat{l}_2 \quad \hat{l}_3]^T = [l_3 \quad l_2 \quad l_1 \quad \hat{l}_3]^T \tag{6.30}$$

$$[\hat{m}_A \quad \hat{m}_1 \quad \hat{m}_2 \quad \hat{m}_3]^T = [m_3 \quad m_2 \quad m_1 \quad \hat{m}_3]^T \tag{6.31}$$

$$[\hat{I}_A \quad \hat{I}_1 \quad \hat{I}_2 \quad \hat{I}_3]^T = [I_3 \quad I_2 \quad I_1 \quad \hat{I}_3]^T \tag{6.32}$$

Note that the parameters of link 3 do not have a physical meaning because there is no corresponding part in the real model. Hence, these can be arbitrary values.

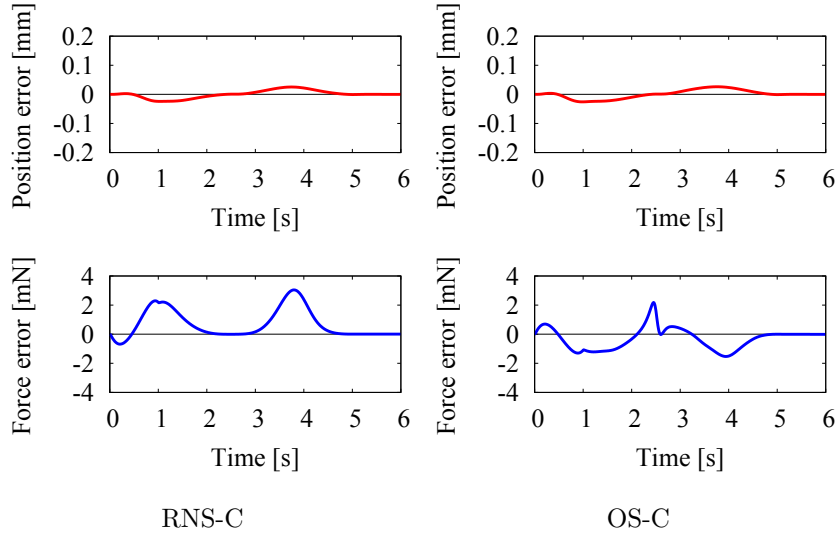


Fig. 6.3: Simulation results of end-effector position and force. The position error is along x -direction, while the force error is represented along z direction, in the end-effector frame.

Simulation

We verify the performance of the RNS-based motion/force control with the three-DoF model. The initial configuration is set to $\boldsymbol{\theta} = [-105 \ -50 \ -60]^T$ deg. The desired path in the unconstrained direction is defined via a fifth-order spline function, s.t. the end effector tracks the circular arc, whose center and radius are $[1.91 \ 1.91]^T$ m, of ± 45 deg in both directions (one full cycle). At the half cycle, the boundary conditions for the two splines are stationary, such that the end-effector pauses instantaneously. The feedback control loops for motion along unconstrained direction (x) is designed as

$$\hat{v}_{A_x}^{ref} = \hat{v}_{A_x}^{des} + k_d(\hat{v}_{A_x}^{des} - \hat{v}_{A_x}) + k_p(\hat{x}_{A_x}^{des} - \hat{x}_{A_x}) \quad (6.33)$$

where k_d and k_p are feedback gains. These are set at $k_d = 10 \text{ s}^{-1}$ and $k_p = 100 \text{ s}^{-2}$, respectively.

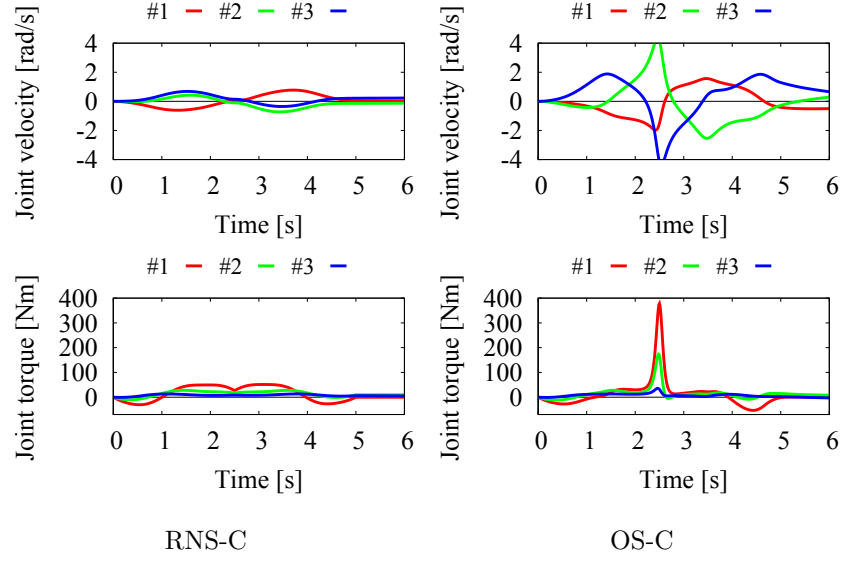


Fig. 6.4: Simulation results of the joint variables.

The desired force in the constrained direction z is designed as a fifth-order spline function during the first second, with a maximum value set at 10 N, to be kept constant for the remaining time. The feedback control loops for the force direction is designed as

$$\hat{f}_{Az}^{ref} = \hat{f}_{Az}^{des} + k_f(\hat{f}_{Az}^{des} - \hat{f}_{Az}) \quad (6.34)$$

where $k_f = 5$ is feedback gain. Note that the setting of the feedback gains is not critical due to the stability properties of the controller. The above values were selected empirically to yield minimal position/force tracking errors. In addition, we also executed the OS formulation under the same conditions for comparison. Note that, under the RNS-based control, the constrained link mass and length are set to $\hat{m}_3 = 10^5$ kg and $\hat{l}_3 = 0$ m. The role of the constrained link parameters will be mentioned in Chapter 7. Note that we assume zero gravity because gravity compensation induces a cyclic joint

motion with a large velocity under the OS formulation based control. The reason will be mentioned in the next chapter.

Fig. 6.3 and Fig. 6.4 show the task and joint-space simulation results obtained with RNS-C and OS-C. From Fig. 6.3, it is apparent that the order of end-effector position/force error are almost identical for the two controllers. This means that the properties of full motion/force decoupling could be validated with both controllers. Further on, from the joint-space behavior results shown in Fig. 6.4, it becomes apparent that the joint velocity obtained from the OS-C simulation undergoes much larger fluctuations than that in the RNS-C one; the respective peak values are 4.22 rad/s against 0.73 rad/s.

From these results, we can conclude that the RNS based motion/force control has a good capability as same as the OS formulation one does on the end-effector tracking performance. In addition, from the perspective of joint behavior, the RNS based control would be better performance than the OS formulation one.

6.2.2 Seven DoF redundant manipulator

Next, we verify the performance of the controllers with a seven-DoF redundant manipulator. The manipulator model is based on the arm of *Rollin' Justin*. The kinematic structure of the model and its control model for the RNS-based controller are depicted in Fig. 6.5. With this model, we straightforwardly use the control input describe in (6.18). The model parameters transformation would be done through the same manner in the case of the planar model. Namely, \hat{m}_7 , $\hat{\mathbf{I}}_7$ and \hat{l}_3 are the constrained link parameters of this model.

The initial configuration is set to $[20 \ -20 \ 0 \ 100 \ 0 \ 10 \ 0]^T$ deg. We assume that z direction in $\{E\}$ is the constrained direction due to the wall, while x - y plane in $\{E\}$ is the unconstrained direction as shown in Fig. 6.6. The desired motion path in the unconstrained direction is defined as a straight

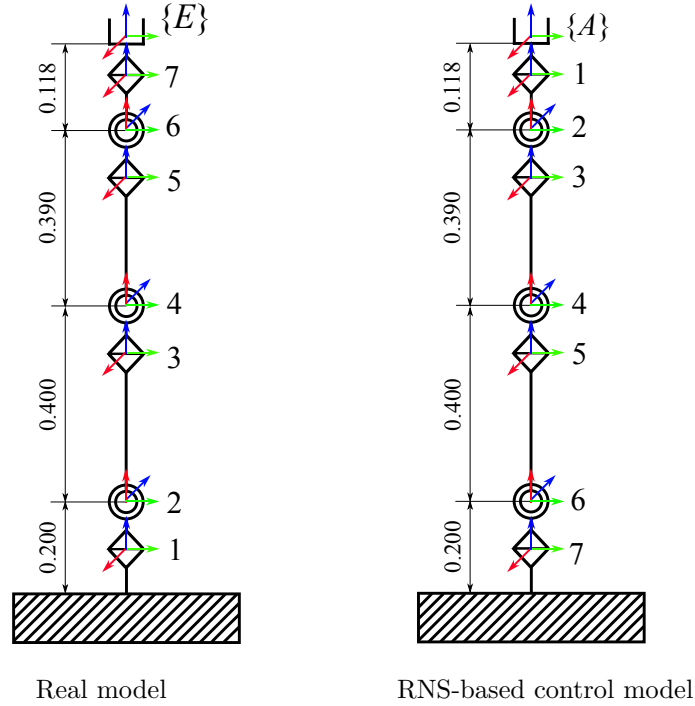


Fig. 6.5: Simulation model based on the arm of Rollin' Justin.

line along x -axis to $[0.24 \ 0.43 \ 0.43]^T$ m via fifth-order spline function. The desired motion is designed as a repeat motion between the initial position and the final one during 2.5 s, respectively. The desired force trajectory acting to z axis is defined as a fifth-order spline function during the first second, with a maximum value set at 10 N. In this case, simulation of the OS formulation is also executed under the same conditions. Note that, in both cases, orientation of the end-effector is fixed for the sake of simplicity.

Simulation results are displayed in Fig. 6.7 and Fig. 6.8. These quantities are measured in the inertial frame. From the results, it becomes apparent that the task-space behavior is almost identical for the two controllers. On the other hand, there is a different behavior in joint-space, especially joint velocity, in the same way as the planar case.

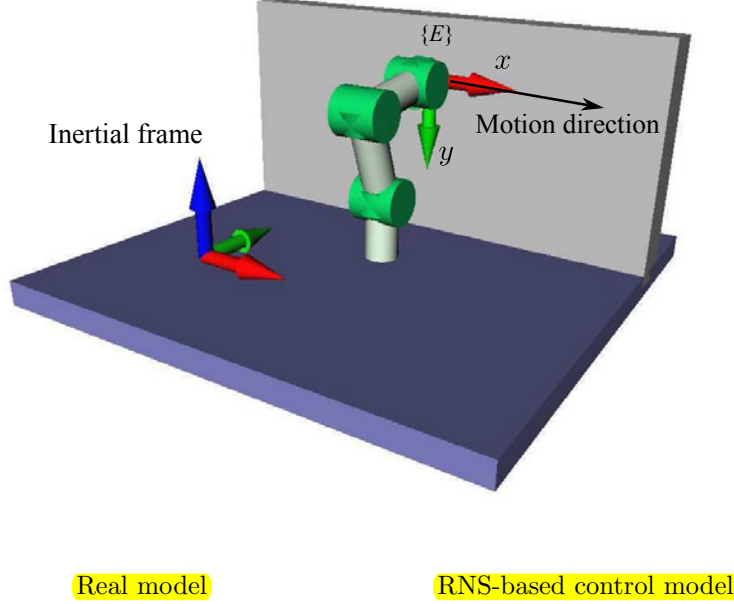


Fig. 6.6: Motion control direction is along x axis, while force control direction is along z axis, in the end-effector frame $\{E\}$.

6.3 Summary

This chapter described motion/force control methods. From a historical point of view, we first explained the OS formulation that has been used in various control schemes, such as hybrid motion/force control and impedance control. Then, a new introduced motion/force control method based on Reaction Null-Space was presented. Through numerical simulation with a planar and spatial models, we verified their performance from the perspective of both task-space and joint-space. It was confirmed that the task-space behaviors were almost identical for the two controllers. On the other hand, there was a difference between the two controllers in joint-space; the amplitude of joint velocities under the RNS-based control can be reduced smaller than

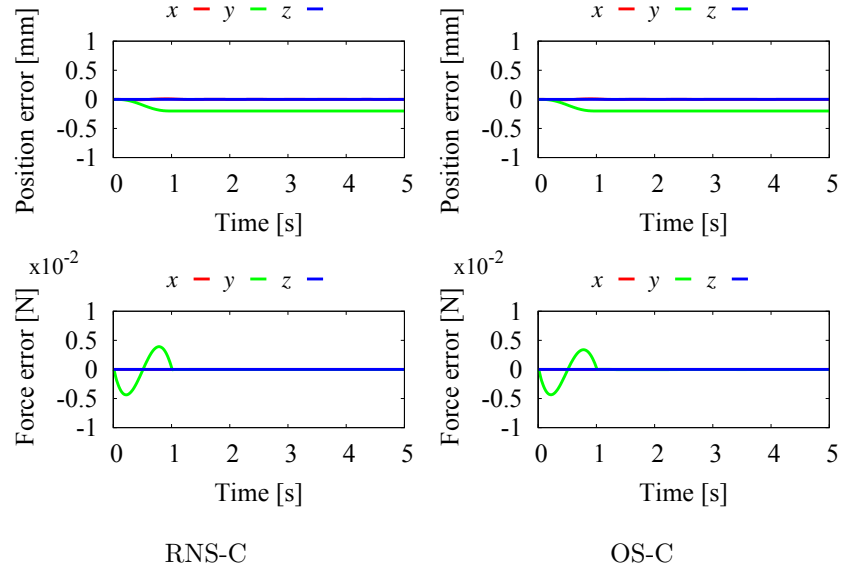


Fig. 6.7: Simulation results of end-effector position and force measured in the inertial frame.

that under the OS formulation.

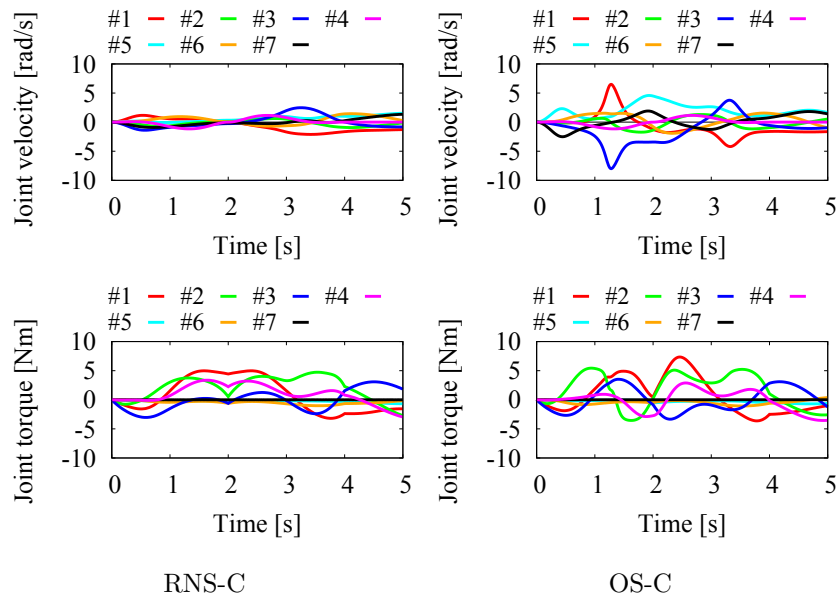


Fig. 6.8: Simulation results of joint-space behavior.

Chapter 7

Analysis of Joint Motion Behavior

In this chapter, we focus on the joint motion under the RNS-based motion/force control. As explained already in Chapter 6, the terminal link mass can have an arbitrary value in the control model. We examine the influence arising from change of the mass through numerical simulation.

7.1 Influence of the inertia parameter

As explained already in Chapter 6, the control model for the RNS-based control has an additional link compared to the real model. When we consider terrestrial manipulators, the meaning of the link is the ground. On the other hand, assuming unfixed base robots such as humanoids and space robots, the link is a floating base. In particular, in the case of fixed-base manipulators, the constrained link parameters can have arbitrary values because these do not have a physical meaning. However, the parameters play an important role under the RNS-based control, because the control method makes use of the dynamic coupling between the terminal link and other links. Hence, it is important to examine the influence of the inertia parameter to the system behavior. In what follows, we examine the influence with a planar model and

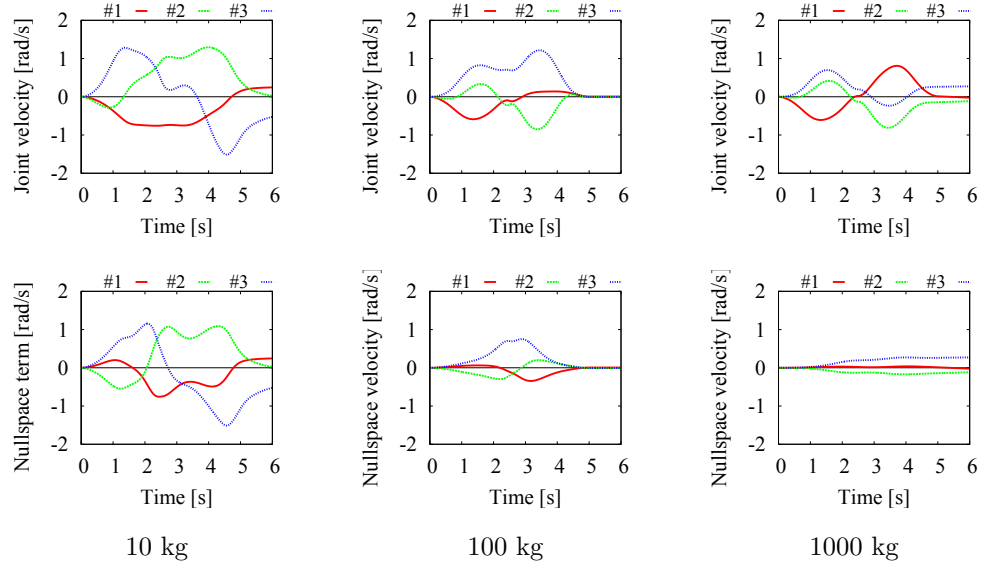


Fig. 7.1: The time profiles of the joint velocity and the null-space velocity: the upper part represents the joint velocity; the lower part is the null-space velocity, respectively.

the spatial model used in Chapter 6, via numerical simulations.

7.1.1 Analysis through simulation

Let us consider the three-link planar model that is shown in Fig. 6.2. In the real model, we suppose that the each link mass is $m_i = 10$ kg, the each link length is $l_i = 1$ m, ($i = 1, 2, 3$). The constrained link mass is supposed to take the following values: 10, 100, 1000 kg. The inertia moment of the constrained link varies proportional to the mass value. In addition, to focus on the joint motion, we assume that there is no interaction between the end-effector and the environment, without losing generality. The desired trajectory of the end-effector is a circular arc whose center is located on $[1.91, 1.91]^T$ m and radius is 0.707 m, respectively.

We show the time profile of the joint velocity and the null-space velocities

in Fig. 7.1. In the figure, the upper part shows the joint velocity with ~~the~~ each constrained link mass; the lower part is the null-space velocity, respectively. From the results, we can confirm that the null-space velocity is gradually decreased, when increasing the constrained link mass. Our concern is the existence of the limit to which the motion under the RNS-based control converges, when the constrained link mass/inertia moment become very large. Actually, this limit exists and coincides with the minimum acceleration norm solution, which is obtained from resolved acceleration control [59] with the particular solution only. In what follows, we discuss this interesting feature.

7.1.2 Discussion

Minimum acceleration constraint

First, we obtain the condition of the minimum acceleration norm solution. The equation describing the relation between end-effector acceleration and joint acceleration is expressed in the following form:

$$\dot{\mathcal{V}}_e = \mathbf{J}_e \ddot{\boldsymbol{\theta}} + \dot{\mathbf{J}}_e \dot{\boldsymbol{\theta}} \quad (7.1)$$

From the above equation, given an end-effector acceleration, the joint space can be divided ~~onto~~ the two orthogonal sub~~space~~ as follows:

$$\ddot{\boldsymbol{\theta}} = \mathbf{J}_e^+ (\dot{\mathcal{V}}_e - \dot{\mathbf{J}}_e \dot{\boldsymbol{\theta}}) + \mathbf{P}_J \ddot{\boldsymbol{\theta}}_a \quad (7.2)$$

where $\mathbf{P}_J = \mathbf{E} - \mathbf{J}_e^+ \mathbf{J}_e \in \mathbb{R}^{n \times n}$ is the projection ~~into~~ the null-space of the Jacobian, $\ddot{\boldsymbol{\theta}}_a \in \mathbb{R}^n$ is an arbitrary vector with dimensions of joint acceleration. The first term is the joint motion whose character is the minimum acceleration norm, the second term is the orthogonal term. We define the joint acceleration set \mathcal{Q}_J as (7.2). **Using the motion decomposition in (7.2) is referred to as the resolved acceleration control.**

The RNS constraint

Let us recall the constraint under the RNS-based control as follows:

$$\ddot{\boldsymbol{\theta}} = -\hat{\mathbf{M}}_{Al}^+(\hat{\mathbf{M}}_A\dot{\mathbf{V}}_A + \hat{\mathbf{C}}_A) + \hat{\mathbf{M}}_{Al}^+\hat{\mathbf{T}}\mathcal{F}_B + \hat{\mathbf{P}}_{RNS}\ddot{\boldsymbol{\theta}}_a \quad (7.3)$$

Note that we assume zero gravity environments without losing generality. Among these acceleration terms, we define a joint acceleration set related to the RNS-constraint as follows:

$$\mathcal{Q}_{M_{Al}} = \{\ddot{\boldsymbol{\theta}} \in \mathbb{R}^n | \ddot{\boldsymbol{\theta}} = -\hat{\mathbf{M}}_{Al}^+(\hat{\mathbf{M}}_A\dot{\mathbf{V}}_A + \hat{\mathbf{C}}_A) + \hat{\mathbf{P}}_{RNS}\ddot{\boldsymbol{\theta}}_a\} \quad (7.4)$$

This set consists of the accelerations appearing in (7.3) except the acceleration related to the constrained force. Namely, $\mathcal{Q}_{M_{Al}}$ represents the acceleration set that is satisfied with a completely free-floating model.

The interpretation

First, we assume that the order of the constrained link mass is the same as **taht** of the other links mass. In this case, $\mathcal{Q}_{M_{Al}}$ must differ from \mathcal{Q}_J , generally. Then, the constrained force related term acts to make the acceleration obtained from the RNS belong to \mathcal{Q}_J . The geometrical interpretation is shown in Fig. 7.2 (a). **This is the mechanism that the RNS-based controller satisfies.**

Next, we consider the case when the constrained link **mass** takes a huge value. In this case, the linear and angular velocity of the constrained link become zero, according to the momenta conservation laws, as follows:

$$\hat{\mathbf{v}}_n = \lim_{\hat{m}_n \rightarrow \infty} \frac{1}{\hat{m}_n} \sum_{i=0}^{n-1} \hat{m}_i \hat{\mathbf{v}}_i = \mathbf{0} \quad (7.5)$$

$$\hat{\boldsymbol{\omega}}_n = \lim_{\hat{I}_n \rightarrow \infty} \frac{1}{\hat{I}_n} \sum_{i=0}^{n-1} \{\hat{\mathbf{I}}_i \hat{\boldsymbol{\omega}}_i + \hat{m}_i \hat{\mathbf{r}}_i^\times \hat{\mathbf{v}}_i\} = \mathbf{0} \quad (7.6)$$

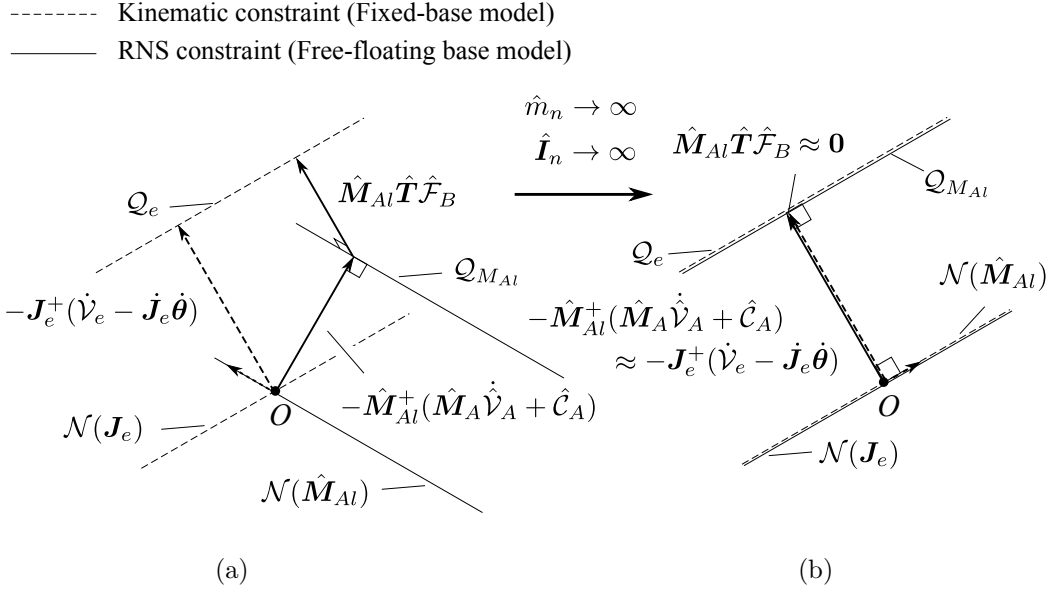


Fig. 7.2: A geometrical interpretation of the RNS constraint: (a) with a small mass of the constrained link and (b) with a large value of the mass.

Therefore, the free-floating base robot behaves as a n -link fixed base robot even if there is no constrained force. This means that $\mathcal{Q}_{M_{Al}}$ gradually converges to \mathcal{Q}_J , when increasing the value of the constrained link mass. The interpretation is shown in Fig. 7.2 (b). Consequently, the motion under the RNS-based control coincides with that under the resolved acceleration control, i.e. minimum acceleration norm.

7.1.3 Verification via numerical simulations

In what follows, we verify the character through numerical simulations with the planar model. We compare a specific part of $\mathcal{Q}_{M_{Al}}$ with \mathcal{Q}_J under $\ddot{\theta}_a = \mathbf{0}$ in the both set. The simulation conditions are the same ones used in Section 7.1.1. To evaluate the equivalence, we make use of the root mean square (RMS) of the motion error between under the RNS-based control and

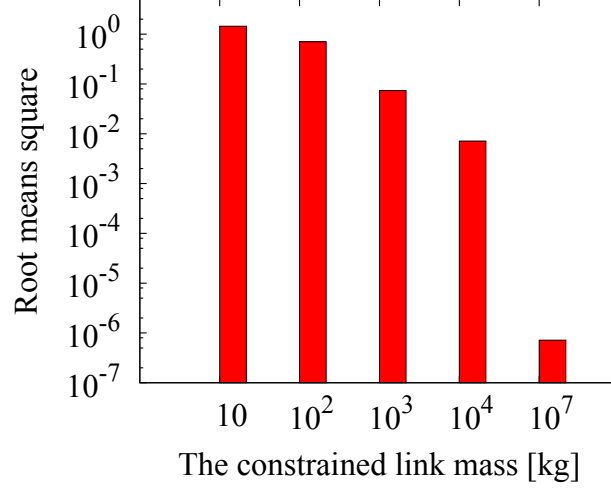


Fig. 7.3: The root means square of the motion error.

the resolved acceleration control as follows:

$$\text{RMS}[\Delta\theta] = \sqrt{\frac{1}{t_f - t_0} \int_{t_0}^{t_f} \|\Delta\theta(t)\|^2} \quad (7.7)$$

$$\Delta\theta(t) = \theta_{RNS}(t) - \theta_{RA}(t) \quad (7.8)$$

where θ_{RNS} and θ_{RA} stand for the joint motion under the RNS-based control and the resolved acceleration control, respectively.

The simulation results are displayed in Fig. 7.3. The simulations were conducted with some values of the constrained link mass. In the graph, note that y -axis is represented via log scale. From the results, we can confirm that the motion error described in (7.8) is gradually reduced, when increasing the value of the constrained link mass. Hence, the character is proved.

7.2 Stabilization of joint motion

Despite acceleration-based kinematic control schemes have advantages in terms of responsive and precise motion, there is a problem with instability of the joint motion. The problem has been discussed by several researchers [33, 60, 61]. In particular, it has been pointed out that the local torque optimization frequently yields unstable behavior. For this problem, an important analysis that clarifies the mechanism of the instability was done in [62]. In that work, it was shown that the null-space acceleration/torque vectors that yield the local torque minimization work as a positive feedback input on the null-space velocity. As a result, ~~the~~ instability can be observed. To obtain a stable behavior of ~~the~~ joint motion, it is mentioned that global optimization is necessary for torque minimization [34]. In the same work, some redundancy resolution schemes were also compared with a three-link model. These schemes are minimum acceleration norm, local torque minimization and the weighted minimum acceleration norm with the inertia matrix. Among them, the local torque minimization and the inertia weighted minimum acceleration schemes became destabilized. On the other hand, the minimum acceleration norm did not become unstable, frequently. However, the method also can be unstable under specific conditions. An analysis indicated that all redundancy resolution schemes with dimension of acceleration can become unstable [62]: i.e. there is a finite escape time in all schemes.

As a different matter related to the instability, it is well-known that the null-space velocities remain at the end of motion, with acceleration based control methods.

To overcome these problems, velocity based acceleration control methods have been focused on by some researchers [63–65]. The solution is obtained as the time differential of velocity based solutions. The solution does not

cause the instability because of the property of the minimum velocity norm constraint. In [65], local torque minimization was carried out based on the velocity based methods.

As seen in Chapter 6 and Section 7.1.1, ~~the remaining~~ joint velocity at the end of motion was observed. ~~For~~ the problem, we obtain the velocity based acceleration solution for the RNS-based control, in what follows.

7.2.1 ~~The~~ velocity-level based acceleration solution

We begin to formulate the solution, considering a velocity level equation. In this case, the velocity level equation is the momenta equations. These equations can be written as follows:


$$\hat{\mathbf{M}}_A \dot{\mathcal{V}}_A + \hat{\mathbf{M}}_{Al} \dot{\boldsymbol{\theta}} = \mathbf{0} \quad (7.9)$$

We assume no interaction and zero gravity, for the sake of simplicity. Given the assumption, we do not lose generality. When considering zero null-space motion, the joint velocity can be expressed as follows:

$$\dot{\boldsymbol{\theta}} = -\hat{\mathbf{M}}_{Al}^+ \hat{\mathbf{M}}_A \dot{\mathcal{V}}_A \quad (7.10)$$

This equation implies the minimum velocity constraint. Taking derivative of (7.10) in terms of time, we can obtain the velocity based acceleration solution as follows:

$$\begin{aligned} \ddot{\boldsymbol{\theta}} &= -\frac{d}{dt}(\hat{\mathbf{M}}_{Al}^+) \hat{\mathbf{M}}_A \dot{\mathcal{V}}_A - \hat{\mathbf{M}}_{Al}^+ (\dot{\hat{\mathbf{M}}}_A \dot{\mathcal{V}}_A + \hat{\mathbf{M}}_A \ddot{\mathcal{V}}_A) \\ &= -\hat{\mathbf{M}}_{Al}^+ (\dot{\hat{\mathbf{M}}}_A \dot{\mathcal{V}}_A + \hat{\mathcal{C}}_A) + \hat{\mathbf{P}}_{RNS} (\dot{\boldsymbol{\theta}}_a - \dot{\hat{\mathbf{M}}}_{Al}^T (\hat{\mathbf{M}}_{Al} \hat{\mathbf{M}}_{Al}^T)^{-1} \hat{\mathbf{M}}_A \dot{\mathcal{V}}_A) \end{aligned} \quad (7.11)$$

where the time differential of the pseudoinverse can be obtained as follow 

$$\frac{d}{dt}(\hat{\mathbf{M}}_{Al}^+) = -\hat{\mathbf{M}}_{Al}^+ \dot{\hat{\mathbf{M}}}_{Al} \hat{\mathbf{M}}_{Al}^+ + \hat{\mathbf{P}}_{RNS} \dot{\hat{\mathbf{M}}}_{Al}^T (\hat{\mathbf{M}}_{Al} \hat{\mathbf{M}}_{Al}^T)^{-1} \quad (7.12)$$

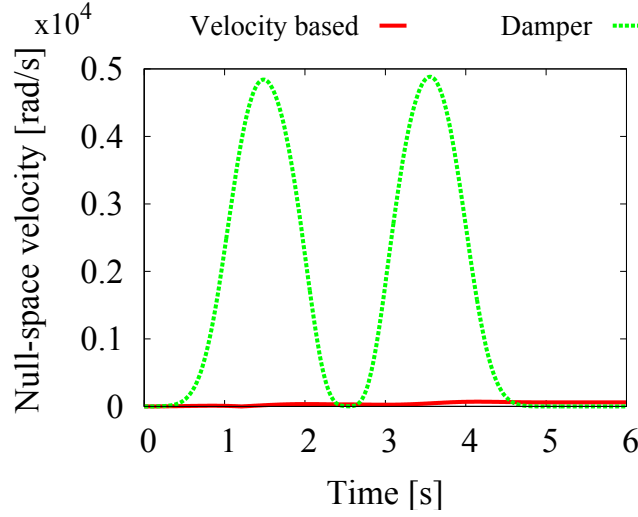


Fig. 7.4: Time profile of the Euclidean norm of the null-space velocity: the line in red represents the velocity based acceleration solution; the line in green stands for the velocity with the damper.

Comparing (7.11) with (7.3), we can see that there is an additional acceleration term in (7.11), as follows:

$$\ddot{\boldsymbol{\theta}} = -\hat{\mathbf{P}}_{RNS} \dot{\mathbf{M}}_{Al}^T (\hat{\mathbf{M}}_{Al} \hat{\mathbf{M}}_{Al}^T)^{-1} \hat{\mathbf{M}}_A \mathcal{V}_A \quad (7.13)$$

Equation (7.11) is the minimum velocity solution in terms of acceleration.

7.2.2 Verification via numerical simulations

Here, we verify the validness of the obtained solution through numerical simulations with the three-link planar model. The simulation conditions and the desired motion of the end-effector were the same ones that are used in Section 7.1.1. The constrained link mass was set to 10^4 kg.

To evaluate the validness, the resultant joint velocity is decomposed into the two parts as follows:

$$\dot{\boldsymbol{\theta}} = (\mathbf{E} - \hat{\mathbf{P}}_{RNS}) \dot{\boldsymbol{\theta}} + \hat{\mathbf{P}}_{RNS} \dot{\boldsymbol{\theta}} \quad (7.14)$$

Under the minimum velocity norm condition, the second term in (7.14) must be zero. Hence, we make use of the Euclidean norm of the second term as the cost function. To obtain a comparative evaluation, we executed a simulation with adding a damping term into the null-space acceleration in (7.3): $\ddot{\theta}_a = -\mathbf{K}_d \dot{\theta}$. The value of the damper $\mathbf{K}_d = \text{diag}(k_d, k_d, k_d)$ was a high limit without causing instability: $k_d = 2770 \text{ s}^{-1}$.

We show the time profiles of the Euclidean norms in Fig. 7.4. In the graph, the line in red represents the velocity-level based solution; the line in green stands for the result with the damping term. Comparing with these results, we can see that the order of the null-space velocity with the damping is much larger than that with the velocity level-based solution. Hence, we can conclude that the proposed stabilization term has a good potential in terms of joint stabilization.

7.3 Summary

In this chapter, we discuss the joint motion under the RNS-based control. As an interesting character, we found out that the joint motion under the RNS-based control converges to that under the resolved acceleration control, increasing the constrained link mass.

As a different issue, we dealt with the instability of the joint motion arising from non-integrability of acceleration-level based control methods. We derived a velocity-level based acceleration solution to obtain a stable motion. This solution was verified via numerical simulation; that has a potential in terms of joint stabilization.

Chapter 8

Conclusions and Future Research Directions

8.1 Conclusions


The aim of this work was developing control methods based on the Reaction Null-Space formulation for redundant manipulators. In particular, we tackled two control issues: (i) reactionless motion control for free-floating space robots and (ii) motion/force control for fixed-base redundant manipulators.

In the case of the first issue, we aimed to propose some tasks suitable for execution under reactionless motion control. First, we examined the properties of reactionless motion with a planar two-DoF model. Through vector field analysis, we confirmed that the manipulator attachment position plays an important role as a bifurcation parameter. Then, the reactionless motions of a seven-DoF redundant manipulator was discussed. From the perspective of the kinematic structure of the model, we represent reactionless motion of the model as superposition of the predominant wrist and elbow motion. Based on these motions, we proposed three motion tasks: (a) an inspection task using a hand camera, (b) a point-to-point positioning task and (c) a deployment task from a stowed configuration. The performances were verified through numerical simulation.

As an interesting feature of reactionless motion control, we found out that reactionless motion coincides with instantaneous minimum energy motion when no base-attitude deviation is assumed. This feature arises from the high energy consumption of reaction wheels. The kinetic energy to compensate the base reaction induced by manipulator motion is represented as a quadratic function of the manipulator parameters, while the kinetic energy of manipulator is a linear function. Hence, reactionless motion is feasible from the perspective of energy efficiency due to the no usage of reaction wheels. This feature was verified via numerical calculation. Finally, we compared the energy consumption of reactionless motion with that of reaction wheels used control system, under the inspection task explained above. From the above results, we can conclude that reactionless motion control is feasible from the perspective of both time and energy efficiency.


On the other hand, we proposed motion/force control based on the Reaction Null-Space formulation. We formulated the control scheme and verified it with a planar and a spatial model through numerical simulation. From the results, we confirmed that the performance of the task space control is as accurate as that of a method based on the Operational Space formulation, which is the most well-known/used method.

We found out that the joint motion under ~~the~~ Reaction Null-Space control coincides with that under ~~the~~ kinematic control with minimum acceleration norm solution, when the constrained link mass/inertia is massive.


As a different issue in redundancy, we tackled  joint stabilization problem. It is known that unstable behavior of joint motion appears even when the task space is stable, due to **the non-integrability of the control method.** With regard to this problem, we formulated a velocity-based stabilization term for ~~the~~ Reaction Null-Space control. Then, it was confirmed that the performance is better than that of a simple damping term.

8.2 Future tasks

Reactionless motion control

- Singularity of the coupling inertia matrix: Even  the kinematic singularities have been much discussed, ~~the singularity within~~ the coupling inertia matrix has been unclear, so far. Because the matrix is highly nonlinear and complicated, we cannot discuss it analytically. So, we have to create numerical schemes to the singularities.
- Manipulator design for reactionless motion control: In this work, we only dealt with a seven-DoF redundant manipulator. With the model, ~~the~~ position control of the end-effector under reactionless motion is impossible. However, position control of the end-effector can be used in several tasks such as assembly, inspection and construction and so on. Hence, we should improve the performance of the control method. One possible way is making use of appropriate manipulators for execution of reactionless motion control. By adding additional DoFs, we can expect that the movable region of the end-effector under reactionless motion broadens.

Motion/Force control

- Influences stemming from the particular solution component: We compared the proposed Reaction Null-Space based control with the Operational Space formulation based control. Then, it was confirmed that the control accuracy of  task space was identical, while joint space behavior was quite different. Even so, if we add a null-space component, the two joint motions become the same one. Our concern is whether the particular components make the system dynamics different even when a redundant control is executed. Especially we should discuss it from the perspective of zero dynamics.

References

- [1] A. Flores-Abad, O. Ma, K. Pham, and S. Ulrich, “A review of space robotics technologies for on-orbit servicing,” *Progress in Aerospace Sciences*, vol. 68, pp. 1–26, Jul. 2014.
- [2] M. Oda, K. Kibe, and F. Yamagata, “ETS-VII, space robot in-orbit experiment satellite,” in *Proceedings of IEEE International Conference on Robotics and Automation*, vol. 1, 1997, pp. 739–744.
- [3] T. Yangsheng Xu, Kanade, *Space Robotics: Dynamics and Control*. Springer, 1993.
- [4] Y. Masutani, F. Miyazaki, and S. Arimoto, “Sensory feedback control for space manipulators,” in *Proceedings of IEEE International Conference on Robotics and Automation*, 1989, pp. 1346–1351.
- [5] K. Yoshida, “Engineering test satellite VII flight experiments for space robot dynamics and control: theories on laboratory test beds ten years ago, now in orbit,” *The International Journal of Robotics Research*, vol. 22, no. 5, pp. 321–335, 2003.

- [6] Y. Umetani and K. Yoshida, "Resolved motion rate control of space manipulators with generalized Jacobian matrix," *IEEE Transactions on Robotics and Automation*, vol. 5, no. 3, pp. 303–314, 1989.
- [7] S. Dubowsky and M. Torres, "Path planning for space manipulators to minimize spacecraft attitude disturbances," in *Proceedings of IEEE International Conference on Robotics and Automation*, 1991, pp. 2522–2528.
- [8] K. Yoshida, "Practical coordination control between satellite attitude and manipulator reaction dynamics based on computed momentum concept," in *Proceedings of IEEE/RSJ International Conference on Intelligent Robots and Systems (IROS'94)*, 1994, pp. 1578–1585.
- [9] F. Aghili, "Coordination control of a free-flying manipulator and its base attitude to capture and detumble a noncooperative satellite," in *Proceedings of IEEE/RSJ International Conference on Intelligent Robots and Systems*, Oct. 2009, pp. 2365–2372.
- [10] S. Dubowsky and E. Papadopoulos, "The kinematics, dynamics, and control of free-flying and free-floating space robotic systems," *IEEE Transactions on Robotics and Automation*, vol. 9, no. 5, pp. 531–543, 1993.
- [11] D. Nenchev, K. Yoshida, and Y. Umetani, "Analysis, design and control of free-flying space robots using fixed-attitude-restricted jacobian matrix," in *Proceedings of The Fifth International Symposium on Robotics Research*, 1990, pp. 251–258.
- [12] D. Nenchev, K. Yoshida, P. Vichitkulsawat, and M. Uchiyama, "Reaction null-space control of flexible structure mounted manipulator systems," *IEEE Transactions on Robotics and Automation*, vol. 15, no. 6,

pp. 1011–1023, 1999.

- [13] D. Nenchev and K. Yoshida, “Impact analysis and post-impact motion control issues of a free-floating Space robot subject to a force impulse,” *IEEE Transactions on Robotics and Automation*, vol. 15, no. 3, pp. 548–557, Jun. 1999.
- [14] K. Yoshida, K. Hashizume, and S. Abiko, “Zero reaction maneuver: flight validation with ETS-VII space robot and extension to kinematically redundant arm,” in *Proceedings of IEEE International Conference on Robotics and Automation*, 2001, pp. 441–446.
- [15] D. Hirano, Y. Fujii, S. Abiko, R. Lampariello, K. Nagaoka, and K. Yoshida, “Simultaneous Control for End-Point Motion and Vibration Suppression of a Space Robot Based on Simple Dynamic Model,” in *Proceedings of IEEE International Conference on Robotics and Automation*, 2014, pp. 6631–6637.
- [16] T. Oki, H. Nakanishi, and K. Yoshida, “Whole-body motion control for capturing a tumbling target by a free-floating space robot,” in *Proceedings of IEEE/RSJ International Conference on Intelligent Robots and Systems*. IEEE, Oct. 2007, pp. 2256–2261.
- [17] N. Hara, D. Nenchev, and D. Sato, “Momentum conserving path tracking through dynamic singularities with a flexible-base redundant manipulator,” in *2010 IEEE/RSJ International Conference on Intelligent Robots and Systems*, 2010, pp. 5392–5397.
- [18] D. Dimitrov and K. Yoshida, “Utilization of the bias momentum approach for capturing a tumbling satellite,” in *Proceedings of IEEE/RSJ International Conference on Intelligent Robots and Systems*, 2004, pp. 3333–3338.

- [19] S. V. Shah, I. Sharf, and A. Misra, “Reactionless path planning strategies for capture of tumbling objects in space using a dual-arm robotic system,” in *Proceedings of AIAA Guidance, Navigation, and Control Conference*, Reston, Virginia, 2013.
- [20] K. Yoshida, K. Hashizume, D. Nenchev, N. Inaba, and M. Oda, “Control of a space manipulator for autonomous target capture - ETS-VII flight experiments and analysis,” in *Proceedings of AIAA Guidance, Navigation, and Control Conference and Exhibit*, 2000, pp. 2000–4376.
- [21] A. Pisculli, L. Felicetti, P. Gasbarri, G. Palmerini, and M. Sabatini, “A reaction-null/Jacobian transpose control strategy with gravity gradient compensation for on-orbit space manipulators,” *Aerospace Science and Technology*, vol. 38, pp. 30–40, 2014.
- [22] D. N. Nenchev and K. Yoshida, “Singularity-consistent teleoperation techniques for redundant free-flying robots,” in *Proceedings of AIAA Guidance, Navigation, and Control Conference*, 1999, pp. 1895–1902.
- [23] H. Schaub and V. J. Lappas, “Redundant Reaction Wheel Torque Distribution Yielding Instantaneous L_2 Power-Optimal Spacecraft Attitude Control,” *Journal of Guidance, Control, and Dynamics*, vol. 32, no. 4, pp. 1269–1276, 2009.
- [24] M. D. Carpenter and M. A. Peck, “Dynamics of a High-Agility, Low-Power Imaging Payload,” *IEEE Transactions on Robotics*, vol. 24, no. 3, pp. 666–675, 2008.
- [25] M. Carpenter and M. Peck, “Reducing Base Reactions With Gyroscopic Actuation of Space-Robotic Systems,” *IEEE Transactions on Robotics*, vol. 25, no. 6, pp. 1262–1270, 2009.

- [26] Y. Nakamura and S. Ito, “Lowering energy consumption of Space robot systems through kinetic energy conservation,” in *Proceedings of IEEE International Conference on Robotics and Automation*, 1993, pp. 20–25.
- [27] R. Lampariello and G. Hirzinger, “Generating feasible trajectories for autonomous on-orbit grasping of spinning debris in a useful time,” in *Proceedings of IEEE/RSJ International Conference on Intelligent Robots and Systems*, 2013, pp. 5652–5659.
- [28] S. V. Shah and A. Gattupalli, “Energy Optimum Reactionless Path Planning for Capture of Tumbling Orbiting Objects using a Dual-Arm Robot,” in *Proceedings of the 1st International and 16th National Conference on Machines and Mechanisms*, 2013, pp. 16–21.
- [29] O. Khatib, “A unified approach for motion and force control of robot manipulators: The operational space formulation,” *IEEE Journal on Robotics and Automation*, vol. 3, no. 1, pp. 43–53, 1987.
- [30] J. Park, W. Chung, and Y. Youm, “On dynamical decoupling of kinematically redundant manipulators,” in *Proc. 1999 IEEE/RSJ International Conference on Intelligent Robots and Systems*, 1999, pp. 1495–1500.
- [31] C. Ott and A. Kugi, “Resolving the problem of non-integrability of nullspace velocities for compliance control of redundant manipulators by using semi-definite Lyapunov functions,” in *2008 IEEE International Conference on Robotics and Automation*, 2008, pp. 1999–2004.
- [32] J. Nakanishi, R. Cory, M. Mistry, J. Peters, and S. Schaal, “Operational Space Control: A Theoretical and Empirical Comparison,” *The International Journal of Robotics Research*, vol. 27, pp. 737–757, 2008.

- [33] J. Hollerbach and K. S. K. Suh, “Redundancy resolution of manipulators through torque optimization,” *Proceedings. 1985 IEEE International Conference on Robotics and Automation*, vol. 2, no. 4, 1985.
- [34] J. Hollerbach, “Local versus global torque optimization of redundant manipulators,” in *Proceedings of IEEE International Conference on Robotics and Automation*, 1987, pp. 619–624.
- [35] N. Hara, Y. Handa, and D. Nenchev, “End-link dynamics of redundant robotic limbs: The Reaction Null Space approach,” in *2012 IEEE International Conference on Robotics and Automation*, 2012, pp. 299–304.
- [36] H. Sone and D. N. Nenchev, “On some practical reactionless motion tasks with a free-floating space robot,” in *Proceedings of IEEE International Conference on Robotics and Automation*, 2015, pp. 2836–2841.
- [37] M. S. Konstantinov, M. D. Markov, and D. N. Nenchev, “Kinematic control of redundant manipulators,” in *Proceedings of 11th Int. Symp. Industr. Robots*, 1981, pp. 561–568.
- [38] H. Hanafusa, T. Yoshikawa, and Y. Nakamura, “Analysis and control of articulated robot arms with redundancy,” in *Preprints 8th Triennial IFAC World Congress 14:78-83*, 1981.
- [39] Y. Nakamura, H. Hanafusa, and T. Yoshikawa, “Task-priority based redundancy control of robot manipulators,” *The International Journal of Robotics Research*, vol. 6, no. 2, pp. 3–15, 1987.
- [40] D. Nenchev, Y. Umetani, and K. Yoshida, “Analysis of a redundant free-flying spacecraft/manipulator system,” *IEEE Transactions on Robotics and Automation*, vol. 8, no. 1, pp. 1–6, 1992.

- [41] K. Kreutz-Delgado, M. Long, and H. Seraji, “Kinematic analysis of 7-DOF manipulators,” *The International Journal of Robotics Research*, vol. 11, no. 5, pp. 469–481, Oct. 1992.
- [42] R. Boudreau and R. Podhorodeski, “Singularity analysis of a kinematically simple class of 7-jointed revolute manipulators,” *Transactions of the Canadian Society for Mechanical Engineering*, vol. 34, no. 1, pp. 105–117, 2010.
- [43] Y. Nakamura and H. Hanafusa, “Inverse Kinematic Solutions With Singularity Robustness for Robot Manipulator Control,” *Journal of Dynamic Systems, Measurement, and Control*, vol. 108, no. 3, p. 163, 1986.
- [44] C. Wampler, “Manipulator Inverse Kinematic Solutions Based on Vector Formulations and Damped Least-Squares Methods,” *IEEE Transactions on Systems, Man, and Cybernetics*, vol. 16, no. 1, pp. 93–101, 1986.
- [45] D. Nenchev, Y. Tsumaki, and M. Uchiyama, “Adjoint Jacobian closed-loop kinematic control of robots,” in *Proceedings of IEEE International Conference on Robotics and Automation*, 1996, pp. 1235–1240.
- [46] D. N. Nenchev, “Singularity-Consistent Parameterization of Robot Motion and Control,” *The International Journal of Robotics Research*, vol. 19, no. 2, pp. 159–182, feb 2000.
- [47] S. K. Agrawal and S. Shirumalla, “Planning motions of a dual-arm free-floating manipulator keeping the base inertially fixed,” *Mechanism and Machine Theory*, vol. 30, no. 1, pp. 59–70, jan 1995.
- [48] S. Taki and D. Nenchev, “Euler angle based feedback control of large eigenaxis rotations in the presence of singularities and model uncertainty,” in *Proceedings of the 13th International Conference on Control, Automation and Systems*, 2013, pp. 34–39.

- [49] E. Aboaf and R. Paul, “Living with the singularity of robot wrists,” in *Proceedings of IEEE International Conference on Robotics and Automation*, 1987, pp. 1713–1717.
- [50] S. Chiaverini, “Singularity-robust task-priority redundancy resolution for real-time kinematic control of robot manipulators,” *IEEE Transactions on Robotics and Automation*, vol. 13, no. 3, pp. 398–410, Jun. 1997.
- [51] S. Chiaverini, B. Siciliano, and O. Egeland, “Review of the damped least-squares inverse kinematics with experiments on an industrial robot manipulator,” *IEEE Transactions on Control Systems Technology*, vol. 2, no. 2, pp. 123–134, Jun. 1994.
- [52] Y. Tsumaki, D. Nenchev, S. Kotera, and M. Uchiyama, “Teleoperation based on the adjoint Jacobian approach,” *IEEE Control Systems Magazine*, vol. 17, no. 1, pp. 53–62, 1997.
- [53] Y. Tsumaki, S. Kotera, D. Nenchev, and M. Uchiyama, “Advanced experiments with a teleoperation system based on the SC approach,” in *Proceedings of IEEE/RSJ International Conference on Intelligent Robots and Systems*, 1998, pp. 1196–1201.
- [54] D. N. Nenchev, “Natural Motion and Singularity-Consistent Inversion of Robot Manipulators,” in *Advances in Robot Control*. Springer Berlin Heidelberg, 2007, pp. 9–33.
- [55] D. N. Nenchev, Y. Handa, and D. Sato, “Natural motion: Efficient path tracking with robotic limbs,” in *2010 IEEE/RSJ International Conference on Intelligent Robots and Systems*, 2010, pp. 3483–3488.
- [56] K. Yoshida, D. Nenchev, P. Vichitkulsawat, H. Kobayashi, and M. Uchiyama, “Experiments on the PTP operations of a flexible struc-

- ture mounted manipulator system,” *Proceedings of IEEE/RSJ International Conference on Intelligent Robots and Systems*, vol. 1, pp. 246–251, 1996.
- [57] M. Torres and S. Dubowsky, “Path-planning for elastically constrained space manipulator systems,” in *Proceedings of IEEE International Conference on Robotics and Automation*, 1993, pp. 812–817.
- [58] L. Villani and J. De Schutter, “Force Control,” in *Springer Handbook of Robotics*. Springer Verlag, 2008, ch. 7, pp. 161–186.
- [59] J. Luh, M. Walker, and R. Paul, “Resolved-acceleration control of mechanical manipulators,” *IEEE Transactions on Automatic Control*, vol. 25, no. 3, pp. 468–474, 1980.
- [60] K. O’Neil and Y.-C. Chen, “Instability of pseudoinverse acceleration control of redundant mechanisms,” in *Proceedings of IEEE International Conference on Robotics and Automation*, 2000, pp. 2575–2582.
- [61] K. A. O’Neil, “Divergence of linear acceleration-based redundancy resolution schemes,” *IEEE Transactions on Robotics and Automation*, vol. 18, no. 4, pp. 625–631, Aug. 2002.
- [62] A. Maciejewski, “Kinetic limitations on the use of redundancy in robotic manipulators,” *IEEE Transactions on Robotics and Automation*, vol. 7, no. 2, pp. 205–210, 1991.
- [63] S. Ma and D. N. Nenchev, “Local torque minimization for redundant manipulators: a correct formulation,” *Robotica*, vol. 14, no. 2, pp. 235–239, 1996.
- [64] Y. Watanabe, “Acceleration-level analysis on velocity-based motion control of kinematically redundant manipulators,” in *Proceedings of*

IEEE/RSJ International Conference on Intelligent Robots and Systems., 2001, pp. 1–6.

- [65] Shugen Ma, “Local torque minimization of redundant manipulators with considering end-motion joint velocities,” in *1996 IEEE International Conference on Systems, Man and Cybernetics.*, 1996, pp. 1477–1482.

Research Progresses

- [1] 曾根, 佐藤, 金宮, “平面浮遊ベース宇宙ロボットにおける Point-To-Point 無反動制御”, ロボティクス・メカトロニクス講演会, 1P2-K06, 2014.
- [2] 曾根, 佐藤, 金宮, “浮遊ベース宇宙ロボットにおける無反動制御を用いた実用例の提案”, 宇宙科学技術連合講演会, 1P2-K06, 2014.
- [3] H. Sone and D. N. Nenchev, “On some practical reactionless motion tasks with a free-floating space robot,” in *Proc. IEEE Int. Conf. Robot. Autom.*, 2015, pp. 2836–2841.
- [4] D. N. Nenchev, R. Okawa and H. Sone, “Task-space dynamics and motion/force control of fixed-base manipulators under reaction null-space-based redundancy resolution,” *Robotica*, pp. 1–18, 2015.
- [5] 曾根, 佐藤, 金宮, “宇宙ロボットにおける無反動マニピュレーションとリアクションホイール使用時のエネルギー効率の比較検証”, ロボティクス・メカトロニクス講演会, 1P2-U06, 2015.
- [6] 曾根, 佐藤, 金宮, “宇宙ロボットにおける無反動制御のエネルギー効率の解析”, 日本ロボット学会学術講演会, 3C2-06, 2015.
- [7] 曾根, 佐藤, 金宮, “宇宙ロボットにおける無反動制御のエネルギー効率の解析”, 第 98 回総研セミナー (TCU Robotics Workshop), 2015.
- [8] H. Sone and D. N. Nenchev, “Reactionless Camera Inspection With a Free-Flying/Floating Space Robot Under Reaction Null-Space Motion Control,” *Acta Astronautica*, submitted.

- [9] H. Sone and D. N. Nenchev, “Assessment of Reaction-Null Space Based Motion Control During Practical Camera Inspection Task,” in *Proc. The International Symposium on Artificial Intelligence, Robotics and Automation in Space*, submitted.

